

DISSERTATION

USING MODELLING TOOLS TO ADVANCE THE UNDERSTANDING OF
AMMONIA DRY-DEPOSITION AND BIDIRECTIONAL FLUX PROCESSES
NEXT TO LARGE ANIMAL FEEDING OPERATIONS

Submitted by

William Lassman

Department of Atmospheric Science

In partial fulfillment of the requirements

For the Degree of Doctor of Philosophy

Colorado State University

Fort Collins, Colorado

Spring 2020

Doctoral Committee:

Advisor: Jeffrey R. Pierce

Advisor: Jeffrey L. Collett Jr.

Emily V. Fischer

Jay M. Ham

Copyright by William Lassman 2020

All Rights Reserved

ABSTRACT

USING MODELLING TOOLS TO ADVANCE THE UNDERSTANDING OF AMMONIA DRY-DEPOSITION AND BIDIRECTIONAL FLUX PROCESSES NEXT TO LARGE ANIMAL FEEDING OPERATIONS

Ammonia in the atmosphere is a trace gas that can play a big role in the Earth's climate, as well as human and ecological health. Due to its stickiness and solubility, ammonia can enter the biosphere via wet and dry deposition, where excess ammonia input often results in soil acidification, disruption of natural ecological equilibria, and loss of biodiversity. Additionally, ammonia is the most abundant alkaline species in the atmosphere and can react with atmospheric acids to form aerosols, which can affect the earth's radiative balance as well as human health. Ammonia emissions tend to be associated with agricultural sources, such as fertilized fields or animal waste at Concentrated Animal Feeding Operations (CAFOs). Consequently, ammonia emissions tend to be dynamic and highly heterogeneous, and ammonia surface-fluxes are difficult to measure. However, in regions with many large CAFOs, ammonia can be an important regional pollutant, especially if there are sensitive ecosystems or other regional sources of atmospheric acids present.

In this dissertation, I study ammonia dry-deposition fluxes immediately downwind of CAFOs using a variety of modelling tools. First, I discuss original research where I use a coupled K-epsilon model with a Lagrangian-Stochastic ammonia bidirectional exchange surface model to simulate the dispersion and deposition of ammonia downwind of an idealized CAFO. Based on these simulations, the amount of ammonia that undergoes dry deposition depends greatly on the

land surface downwind of the CAFO; replacing bare soil or unmanaged grassland with leafier surfaces such as cropland or forests can increase the fraction of total ammonia emissions that deposits from 2 - 10% to 30 - 50%, though this is sensitive to the ammonia emission potential in the model plant canopy. Next, I describe a separate study where I use a 3-D Large-Eddy Simulation model to simulate the dispersion of ammonia and methane from a CAFO with a time-resolved modelling tool. I use this modelling system to produce synthetic observations, which are used to develop an inversion approach to quantify the ammonia dry deposition near a CAFO with co-located mobile measurements of ammonia and methane. While I demonstrate that such an inversion technique is feasible with surface-based measurements, considerable value is added, in terms of minimizing method bias and increasing method precision, by mounting measurements on a small Unmanned Aerial System (sUAS).

Finally, I present measurements of PM_{2.5} concentration and composition that were made in Palapye, Botswana. Botswana is a developing country with a hot and arid climate. Beef and livestock production are important economic activities in Botswana; however, the agricultural practices differ considerably from the CAFOs discussed in the rest of the dissertation. Furthermore, these livestock activities occur against a backdrop of emissions and air pollutants that differ considerably from the United States and Europe. The measurements show that PM_{2.5} concentrations were on average $9 \mu\text{g m}^{-3}$ during the 5-week measurement period. While below levels that are typically considered hazardous, there was considerable variability in the measured concentrations, and the measurement period is too short to conclusively determine that air pollution is not a public health concern in this region. The aerosol composition is dominated by carbonaceous species, probably from biomass burning, though inorganic sulfate also is abundant

in the aerosol phase. As Botswana continues to undergo economic development, the types of emissions and pollution present will continue to change.

ACKNOWLEDGEMENTS

During my PhD, I have benefitted from the guidance from too many people to name. There is no question in my mind that I would have never been able to make it this far without my support network. I will try to acknowledge as many people as I can, but if you do not find yourself listed here, a) please know that your help is still appreciated, but b) why are you reading this?

First, and foremost, I would like to acknowledge Jeff Pierce. Jeff gave me my first opportunity in atmospheric science by taking me on as a Masters student, and has continued to be my primary adviser throughout my PhD. In addition to the many scientific discussions, I have enjoyed sharing conversations with Jeff about many topics, including sports, fitness, music, and living well-rounded life. Second, I would like to acknowledge Jeff Collett, my co-adviser. Jeff C joined the team midway through my PhD because of his expertise on ammonia and gas-phase processes, in addition to his expertise in measurements. In addition to providing a calming, stabilizing presence to my graduate school experience, Jeff has taught me everything I know about measurements, and the complexities and challenges associated with taking your own data. Third, I would like to acknowledge Emily Fischer and Jay Ham, the members of my PhD committee. Thank you both for your guidance, encouragement, contributions to this research, as well as the instruction both inside and outside the classroom. It has been a privilege to learn from you both. Fourth, I would like to acknowledge Benjamin Loubet. Benjamin was my supervisor/mentor/collaborator/friend during my stay abroad at the Institut National de la Recherche Agronomique where the research in Chapter 2 of my dissertation was accomplished. Benjamin's guidance and insights, as well as his open mind for collaboration, helped to make that project a success. Furthermore, working with him helped me to regain some confidence as a

scientist. I look forward to many years of collaborations in the future. Fifth, and by no means least, I would like to acknowledge Bonne Ford. While we got to work together officially during my Masters degree, Bonne has continued to mentor me in an informal capacity throughout graduate school. Many aspects of being a scientist are not learned in the classroom, but are learned from outstanding individuals setting an example. I think if everybody could be a bit more like Bonne, the scientific community, and the world, would be a better place.

Outside of my mentorship network, there have been many others who have offered their professional assistance, as well as their friendship and camaraderie throughout graduate school. I would like to acknowledge the students in the Pierce group, Fischer group, as well as the other students in the ATS department who have been willing to talk about air pollution, wildfires, the MJO, and other non-scientific nonsense that comes up from time to time. There are too many of you to name but you know who you are. Also, if you're reading this, you are probably on the list (but seriously, get a life). I also want to acknowledge the students and coaches of the CSU triathlon team for giving me a place to set stupid goals, push my limits, and get really really tired. I want to acknowledge Victor, Sonia, and Pauline for welcoming me at INRA with friendship, despite with my somewhat eccentric personality, and my inability to speak French.

Finally, I would be remiss to not mention the people who got me to graduate school in the first place. Thank you to my MI friends (Adam, Alex, and Elliott) and my NU friends (Brad, Paul, Krishna, Daniel, Max, and Cameron) for keeping in touch, and making the time for me, visiting me (even in Europe), and dealing with my neuroticisms. Thank you to Kate for everything you do, from looking after me, to inspiring me to make it through this final push. Thank you to my siblings and parents for your understanding, patience, and support during these years of my life. Finally, thank you to Dean Summerwind for teaching me how to just sit out there parked.

TABLE OF CONTENTS

ABSTRACT.....	ii
ACKNOWLEDGEMENTS.....	v
CHAPTER 1. INTRODUCTION.....	1
1.1 The Nitrogen Cycle, Ammonia, the Colorado Front Range, and CAFOs.....	1
1.2 Boundary-Layer Turbulence Theory and Modelling.....	4
1.3 Dry Deposition and Bidirectional Flux.....	7
1.4 Dissertation Overview.....	9
REFERENCES.....	12
CHAPTER 2. LANDSCAPE ENGINEERING TO INCREASE LOCAL AMMONIA RECAPTURE DOWNWIND OF LARGE ANIMAL FEEDLOTS: A MODELLING ESTIMATE	19
2.1 Introduction.....	20
2.2 Methods.....	23
2.2.1 K-Epsilon Modelling with OpenFOAM	23
2.2.2 Lagrangian-Stochastic Ammonia Dispersion and Bidirectional Flux Modelling with MODDAS.....	24
2.2.3 Simulation Configurations and Parameters.....	26
2.3 Results.....	30
2.3.1 OpenFOAM Simulations.....	30
2.3.2 MODDAS Landuse Simulations.....	33
2.3.3 MODDAS Sensitivity Analysis.....	35
2.3.4 The Effect of Shelterbelts.....	38
2.4 Discussion.....	39

2.4.1 OpenFOAM Simulations.....	39
2.4.2 MODDAS Simulations; Important Parameters and Model Sensitivity.....	42
2.4.3 MODDAS Simulations; Use of Shelterbelts to Increase Ammonia Recapture.....	53
2.5 Conclusions.....	56
REFERENCES.....	58
CHAPTER 3. METHODS OF ESTIMATING DEPOSITION USING ATMOSPHERIC CONCENTRATION MEASUREMENTS: A CASE STUDY OF AMMONIA DOWNWIND OF A FEEDLOT.....	67
3.1 Introduction.....	68
3.2 Methods.....	74
3.2.1 LES SAM Simulations.....	74
3.2.2 Sampling Strategies.....	78
3.3 Results and Discussion.....	82
3.3.1 LES SAM Simulation Results.....	82
3.3.2 Estimation of the Fraction of Ammonia Removed Using All SAM Output.....	84
3.3.3 Using Vehicular and Aerial Platforms to Estimate the Fraction of Ammonia Removed.....	89
3.3.4 Approximations, Limitations, and Implications for Real Measurements.....	95
3.4 Conclusions.....	99
REFERENCES.....	103

CHAPTER 4. USING LOW-COST MEASUREMENT SYSTEMS TO INVESTIGATE	
AIR QUALITY: A CASE STUDY IN PALAPYE, BOTSWANA.....	113
4.1 Introduction.....	114
4.2 Methods.....	117
4.2.1 Site Description and Important Sources.....	117
4.2.2 Field Measurements.....	120
4.2.3 Ancillary and Remote Observations, and Back-Trajectory Modelling.....	122
4.3 Results and Discussion.....	123
4.3.1 PM _{2.5} Concentrations at BIUST.....	123
4.3.2 Filter PM _{2.5} Composition Characterization.....	125
4.3.3 Temporal Variability.....	130
4.4 Conclusions.....	138
REFERENCES.....	141
CHAPTER 5. CONCLUSION.....	154
5.1. Summary of Chapter 2.....	154
5.2. Summary of Chapter 3.....	155
5.3. Summary of Chapter 4.....	156
5.4. Synthesis and Future Work.....	157
REFERENCES.....	163
APPENDIX A.	165
APPENDIX B.	167
B.1.....	167
B.2.....	170

B.3.....	174
----------	-----

CHAPTER 1. INTRODUCTION

1.1 The Nitrogen Cycle, Ammonia, the Colorado Front Range, and CAFOs

With the exception of meteorites, spacecraft launches, and extremely small quantities of trace gases escaping from the top of the atmosphere, Earth does not exchange matter with its surroundings. On Earth, chemically active elements and their respective chemical compounds are continuously cycled between large reservoirs. A particularly well-known example of a biogeochemical cycle is the global carbon cycle, which describes the flux of carbon between the atmosphere, biosphere, and Earth's crust. The global carbon cycle is famous because of its importance for anthropogenic climate change; by removing carbon from a deep crust reservoir (i.e., fossil fuels) and burning the carbon to make CO₂, humans are increasing the atmospheric loading of CO₂, which perturbs the Earth's radiative balance. However, other biogeochemical cycles (e.g., water, phosphorous, sulfur) are also critically important for maintaining climatic, and also biochemical equilibrium on Earth (Fisher, 2017).

The nitrogen cycle is another important biogeochemical cycle on Earth, especially for its role in biochemistry. Most nitrogen on earth is diatomic N₂ gas in the atmosphere. N₂ is chemically very inert, and only undergoes chemical reactions in extreme environments (e.g., inside lightning bolts) to form nitrogen oxides (NO_x) or in special microbially-catalyzed reactions (inside soils, plant roots, and in the oceans) to form ammonia (NH₃); these processes are called “nitrogen fixation”. NH₃ and NO_x are chemically reactive nitrogen species (N_R) and are essential chemical constituents of amino acids, nucleic acids, a.k.a. “the building blocks of life”. Life as we know it could not exist without N_R compounds. However, the nitrogen fixation processes are naturally very slow and are balanced by denitrification reactions which convert N_R, back to N₂. The scarcity of,

and competition for, N_R has been a driver of natural selection for billions of years (Galloway et al., 2013; Galloway and Cowling, 2002). However, in the early 20th century, industrial scale adoption of the Haber-Bosch process has allowed synthetic nitrogen fixation for production of fertilizers (Galloway et al., 1995). Additionally, combustion of fossil fuels in vehicles and industrial combustion processes, such as power generation, can produce NO_x . Anthropogenic nitrogen fixation now exceeds natural nitrogen fixation, and these excess N_R compounds have resulted in large perturbations to the nitrogen cycle (Battye et al., 2017; Vitousek et al., 1997). N_R deposition or leakage into “sensitive ecosystems” (i.e., ecosystems that have evolved under nitrogen-limited conditions) can cause many negative impacts such as allowing invasive species to thrive (e.g., cheat grass in the Rocky Mountains, red tide), decreases in biodiversity, or catastrophic loss of life (e.g., eutrophication from algal blooms) (Vitousek et al., 2013). Additionally, reactive nitrogen species such as ammonium and nitrate can react to form aerosols in the atmosphere, which can directly affect human health (Dockery et al., 1993), and can affect climate by scattering or absorbing radiation or impacting cloud processes (Boucher et al., 2015). Globally, in response to the impact of NO_x on air pollution and human health, regulations on combustion and other NO_x emission processes has decreased the impact of oxidized nitrogen species, and reduced nitrogen species are becoming an increasingly important source of N_R to the atmosphere and environment (Li et al., 2016).

The most abundant reduced nitrogen species in the global nitrogen cycle is ammonia. NH_3 (g) is a gaseous compound that is soluble in water, and dissociates in aqueous solution to form ammonium (NH_4^+); because NH_3 is an alkaline species, it reacts with acids in the atmosphere (e.g., nitric acid, sulfuric acid, or organic acids) to form aerosols. Ammonia is a polar “sticky” molecule and can undergo dry deposition or complex bidirectional interactions with biomass. In these

bidirectional interactions, it is either emitted or absorbed by surface vegetation or soils, depending on the surface, climate, environmental conditions, and atmospheric ammonia concentration (Behera et al., 2013). Ammonia is also extremely difficult to measure with high temporal resolution because it sticks to instrument inlets (Pollack et al., 2019), and therefore the surface fluxes of ammonia are poorly constrained. While soil and vegetation fluxes contribute to ambient background ammonia concentrations, large point or area sources can produce elevated local or regional concentrations of ammonia. Examples of ammonia sources include the following: ammonia volatilization from fertilizers, biological and decomposition processes in wastewater treatment or landfills, and animal waste from livestock operations (Behera et al., 2013).

Metabolic products such as urea can rapidly decompose into ammonia in the environment. Because animals produce waste (Gomi, 2001), large livestock operations can be important local and regional sources of ammonia. In highly industrialized agricultural systems, a large fraction of livestock is produced in Concentrated Animal Feeding Operations (CAFOs), which can house many thousands of individual animals in concentrated facility (Hristov et al., 2011). For example, in Colorado, there are several CAFOs housing more than 40,000 head of cattle, and a few with a maximum capacity exceeding 100,000 head of cattle (“Colorado Cattlemen’s Association,”). CAFOs of this size have had ammonia concentration measurements as high as 20 ppm made nearby (Hacker et al., 2016; Shonkwiler and Ham, 2018; Sun et al., 2015, 2014), compared to an ambient background of 1 ppb. CAFOs in Colorado, and other places in the Western US are visible “ammonia hotspots” based on satellite observations (Van Damme et al., 2018). While the ammonia emissions from CAFOs are a complex function of environmental conditions, CAFO size, and management practices, many studies have measured the emissions flux of ammonia, and both empirical and process-based models of ammonia emissions are becoming available (Hristov et al.,

2011). However, there are large uncertainties in the impact that large CAFOs can have on regional air quality and N_R deposition, in part due to the complexity and heterogeneity of the complex surface interactions immediately downwind of the CAFO. While it is generally thought that a large fraction of CAFO ammonia emissions may undergo dry deposition near the feedlot boundary, the exact size of this fraction is poorly constrained (Hao et al., 2005). The determination of this fractional deposition is a function of two primary processes: dispersion of the CAFO emission plume in a turbulent boundary layer, and the interaction with the surface and dry deposition/bidirectional flux physics.

1.2 Boundary-layer turbulence theory and modelling

The Planetary Boundary Layer (PBL) is defined as the region of the atmosphere where the behavior is directly influenced by interaction with the surface; such interactions include: friction, latent and sensible heat flux, as well as environmental conditions such as atmospheric stability. The focus of this dissertation is the dispersion of ammonia downwind of feedlots, which is a process that occurs close to the surface; therefore, all modelling tools that are useful for this application require the capability to represent atmospheric turbulence and surface interactions in the PBL (Foken, 2008). The atmosphere is a fluid, and therefore the physics and dynamics of the atmosphere are represented by the Navier-Stokes Equations, coupled to the continuity equation for conservation of mass, and the thermodynamics of adiabatic compression and expansion of the fluid. Atmospheric motions span spatial scales of thousands of km (e.g., Rossby waves) to millimeters (viscous and frictional damping) (Holton and Hakim, 2012), and PBL motions include eddies that are the height of the entire PBL, several thousand meters under some conditions; direct numerical simulation (DNS) requires temporally and spatially resolving this broad range of spatial and

temporal scales, and is beyond the capability of modern computing systems. Therefore, numerical solutions of the atmospheric dynamics equations require careful selection of relevant processes to simulate, and parameterization of subgrid-scale or supergrid-scale processes.

One class of approaches that is applied in a variety of Computational Fluid Dynamics (CFD) applications where DNS is not feasible is Reynolds-Averaged Navier-Stokes equations (RANS) equations. The RANS equations are obtained by performing a Reynolds decomposition on the native Navier-Stokes equations to separate the mean flow characteristics from the temporally varying flow characteristics; the time-varying “fluctuation” terms are commonly referred to as the Reynolds Stress tensor. The representation of the Reynolds Stress tensor is referred to as the “turbulence closure”, and this term has no analytical solution, and chaotic numerical behavior; its representation is a major challenge for modern physics. Different RANS techniques use different approaches to parameterize the Reynolds Stress tensor in terms of known quantities (Tennekes and Lumley, 1972). One example of a commonly-applied RANS technique is the K-epsilon model, which expresses the Reynolds stress tensor as a function of the turbulent kinetic energy (TKE or K) and the TKE dissipation rate (epsilon), as defined below:

$$K = \frac{1}{2} u'^2; \quad \epsilon = \frac{\nu}{2} |\nabla u' + u'^T|^2 \quad (1.1)$$

The K-epsilon model also adds two additional equations to model the transport, production, and destruction of k and epsilon, which are coupled to the momentum transfer equation. These models are used to estimate the average flow characteristics for a given scenario, which includes the mean flow as well as the TKE, and TKE dissipation rate. K-epsilon models are used by representing interactions with the surface by using wall functions to parameterize frictional effects on surface mean winds (U), as well as TKE and TKE dissipation (Launder and Spalding, 1974). K-epsilon models are used to simulate flow through and above plant and urban canopies by representing

these flow obstacles as porous media, and representing the fluid interaction with the canopy with source functions in the K-epsilon equations. The K-epsilon model has been shown to perform well in situations where large pressure gradients are absent and the atmospheric boundary layer is neutral. However, a major shortcoming of this approach for use in atmospheric cases is the inability to represent buoyancy effects on the mean and turbulent flow fields; therefore, K-epsilon models do a poor job representing dispersion under stable or unstable conditions. Additionally, representing the Reynolds Stress as a function of U , k , and ϵ is equivalent to assuming isotropic turbulence, which is not often true in the atmosphere (Lovejoy et al., 2007). Nevertheless, the K-epsilon model has been widely adopted for a range of atmospheric modelling applications, such as wind-power generation (Hargreaves and Wright, 2007; Richards and Hoxey, 1993) and forest edge and in-canopy flow (Hanjalic, 2005; Högström et al., 1989; Svensson and Häggkvist, 1990).

Another alternative approach to DNS for modelling the PBL is to apply a low-pass filter to the Navier-Stokes equations to derive a temporally evolving version of the Navier-Stokes equations without resolving the smallest length and temporal scales; this approach is called Large Eddy Simulation (LES) (Smagorinsky, 1963). In LES models, a subgrid-scale model is required to represent processes that the model cannot resolve, such as viscous dissipation or scalar diffusion (Deardorff, 1970). At the model resolution, LES models do not require any assumptions about the Reynolds Stress, and consequently, there is no assumption of isotropic turbulence. Additionally, representing buoyancy effects and atmospheric stability is more straightforward. However, compared to K-epsilon models, LES models require more computing resources to perform simulations, and the representation of surface features such as topography or plant canopies is much more complex. Often, LES simulations that represent in-canopy processes require numerous

K-epsilon simulations of the same system in order to derive model parameters for the canopy inertial effects on the fluid flow (Zhiyin, 2015).

1.3 Dry deposition and bidirectional flux

Gases and aerosols can be deposited to the ground through two processes: wet deposition and dry deposition. Wet deposition occurs when the gas dissolves, or the particle is engulfed in, water and is deposited to the surface as rain, snow, graupel, or fog; while these processes can be responsible for large fluxes between the atmosphere and surface, they only occur during active precipitation, and are governed by a separate set of physical processes relative to dry deposition. Therefore, wet deposition is beyond the scope of this dissertation.

The dry deposition flux is usually modelled as a first order loss process according to Equation 2:

$$F = -v_d C \quad (1.2)$$

where F is the flux (mass per unit area per time), C is the atmospheric concentration (mass per volume), and v_d is the deposition velocity (distance per time). Dry deposition is actually a series of different physical processes that are governed by different physics: (1) a gas or particle is transported by atmospheric turbulence from a height above the surface (commonly referred to as the “reference height”) to the edge of the quasi-laminar boundary layer, (2) diffuses across the laminar boundary layer, and then (3) sticks to the surface. These three processes each often modelled analogously to electrical conduction (or inversely as resistances) are referred to as the atmospheric, quasi-laminar, and surface conductivity. Under this conceptual model, the deposition velocity for gases can be calculated as follows:

$$v_d^{-1} = R_a + R_b + R_s \quad (1.3)$$

where R_a is the atmospheric resistance, R_b is the quasi-laminar boundary layer resistance, and R_s is the surface resistance. The advantage of this approach is that the various processes in dry deposition can be modelled separately. For example, R_a is a function of turbulence and stability in the boundary layer, R_b is a function of the gas diffusivity and quasi-laminar boundary layer thickness, and R_s depends on the affinity of the gas to the surface in question (Seinfeld and Pandis, 2016). In general, R_a is often the rate-limiting step (Phillips et al., 2004) and atmospheric models have had general success representing R_a and R_b in larger-scale models (Wu et al., 2012), suggesting that the physical parameterizations of these processes are sufficiently accurate. However, the representation of R_s is more challenging, and in some cases, can dominate the resistance.

For the specific case of ammonia interacting with a soil or vegetated surface, there are additional layers of complexity. Plants and soils can be sources of ammonia under the right environmental conditions, but become sinks under other environmental conditions. This bidirectional behavior is modelled with a compensation point as follows:

$$F = -v_d(C - \chi_c) \quad (1.4)$$

where χ_c is the canopy compensation point. According to Equation 4, when $C_a > \chi_c$, the canopy is a sink for atmospheric ammonia, but when $\chi_c > C$, the canopy is a source; χ_c is the equivalent concentration of ammonia inside the plant canopy, while v_d behaves as a mass-transfer coefficient for the system (Farquhar et al., 1980). Within the plant canopy, determining χ_c can be complicated. χ_c is the “effective” canopy compensation point, and is determined by the sources and sink of ammonia inside the plant canopy. A simple conceptual model, the “big leaf” model, assumes that the ammonia exchange occurs only with the leaf surface. This model assumes that ammonia has two parallel paths within the plant canopy; it can deposit in a unidirectional process to the leaf

cuticle, with resistance depending on the leaf cuticle pH and RH, or it can undergo bidirectional exchange with the leaf apoplast inside the plant stomata. χ_s , the stomatal compensation point, is modeled by the effective Henry's law solubility of NH_3 gas and dissociation of NH_3 into NH_4^+ , which are functions of T, pH, and NH_4^+ concentration inside the plant (Sutton et al., 1998, 1995). In this model, the canopy compensation point (χ_c) is the algebraic solution of the complicated resistance diagram equations such that it is in equilibrium with atmospheric exchange, as well as the two in-canopy fates for ammonia (cuticular deposition or stomatal uptake). Other more complex bidirectional exchange models also consider ammonia bidirectional exchange with the soil (e.g., two-layer model) or with multiple layers inside the plant canopy (multi-layer model) (Nemitz et al., 2001, 2000); the details of these parameterizations require many hard-to-measure parameters that are literally in the weeds, and can vary over orders of magnitude and over small spatial scales. While ammonia bidirectional flux models of varying complexity are becoming more common in deposition parameterizations inside regional and global chemical transport models, more studies are needed to constrain model parameters, and to test the accuracy of these models under different conditions. For example, few studies have applied these models to conditions with extreme ammonia concentrations such as next to CAFOs, and to date, only one study has attempted to measure some of the parameters for a bidirectional flux model in this type of environment (Shen et al., 2018), despite evidence that these parameters are a strong function of the N_R inputs to ecosystem (Massad et al., 2010).

1.4 Dissertation Overview

Large CAFOs are major sources of ammonia to the surrounding environment, and have the potential to impact regional air quality and N_R deposition. However, the actual impact is quite uncertain due to the fact that a large, but poorly-constrained, fraction of the total ammonia

emissions undergo dry deposition within a few km of the CAFO boundary. There is potential to reduce the net impact CAFOs have on regional N_R deposition and air quality by leveraging this surface loss to sequester more ammonia in the land-surface ecosystem next to these feedlots. However, the fractional deposition is governed by two main physical processes: the turbulent dispersion from these sources, and the complex interaction with the surface. The combination of these processes makes this system challenging to study. Moreover, the challenge of measuring directly ammonia deposition has complicated study of this system and consequently, deposition is a major knowledge gap in our understanding of how important CAFOs are for air quality and N_R .

In this dissertation, I will apply models of atmospheric dispersion coupled with deposition models to investigate ammonia dispersion and deposition downwind of animal feedlots. In Chapter 1, I use OpenFOAM in RANS configuration, using the K-epsilon model to estimate the atmospheric wind field around an idealized CAFO. I then coupled OpenFOAM to MODDAS, a Lagrangian-Stochastic, multi-layer ammonia bidirectional exchange, plant canopy model. This coupled model framework is used to explore the impact of vegetated surfaces on ammonia bidirectional exchange in environments with massive ammonia sources. In Chapter 2, I use LES simulations to explore a novel technique for quantifying the ammonia deposition adjacent to CAFOs by quantifying the change in the concentration ratio of two tracers, one undergoing dry deposition, to represent ammonia and methane dispersion downwind of a CAFO. I also use synthetic observations of the LES model output to demonstrate a proof-of-concept measurement technique for quantifying ammonia deposition near a CAFO. Finally, in Chapter 3, I share results from an exploratory field study of atmospheric aerosols in Palapye, Botswana. Botswana is also a major beef-producing country, and has a similarly dry, grassland climate. However, it is sparsely

populated developing country, with many different types of aerosol sources, as well as different agricultural practices.

REFERENCES

- Battye, W., Aneja, V.P., Schlesinger, W.H., 2017. Is nitrogen the next carbon? *Earth's Future* 5, 894–904. <https://doi.org/10.1002/2017EF000592>
- Behera, S.N., Sharma, M., Aneja, V.P., Balasubramanian, R., 2013. Ammonia in the atmosphere: a review on emission sources, atmospheric chemistry and deposition on terrestrial bodies. *Environ Sci Pollut Res* 20, 8092–8131. <https://doi.org/10.1007/s11356-013-2051-9>
- Boucher, O., Randall, D.A., Artaxo, P., Bretherton, C., Feingold, G., Forster, P., Kerminen, V.-M., Kondo, Y., Liao, H., Lohmann, U., Rasch, P., Satheesh, S.K., Sherwood, S., Stevens, B., Zhang, X.-Y., n.d. Clouds and Aerosols, in: *Climate Change 2013: The Physical Science Basis. Contribution of Working Group I to the Fifth Assessment Report of the Intergovernmental Panel on Climate Change*. Cambridge University Press, Cambridge, United Kingdom and New York, NY USA.
- Colorado Cattlemen's Association [WWW Document], n.d. URL <https://www.coloradocattle.org/> (accessed 11.5.19).
- Deardorff, J.W., 1970. A numerical study of three-dimensional turbulent channel flow at large Reynolds numbers. *Journal of Fluid Mechanics* 41, 453–480. <https://doi.org/10.1017/S0022112070000691>
- Dockery, D.W., Pope, C.A., Xu, X., Spengler, J.D., Ware, J.H., Fay, M.E., Ferris, B.G.Jr., Speizer, F.E., 1993. An Association between Air Pollution and Mortality in Six U.S. Cities. *New England Journal of Medicine* 329, 1753–1759. <https://doi.org/10.1056/NEJM199312093292401>

- Farquhar, G.D., Firth, P.M., Wetselaar, R., Weir, B., 1980. On the Gaseous Exchange of Ammonia between Leaves and the Environment: Determination of the Ammonia Compensation Point. *Plant Physiology* 66, 710–714. <https://doi.org/10.1104/pp.66.4.710>
- Fisher, M.R., 2017. 3.2 Biogeochemical Cycles, in: *Environmental Biology*.
- Foken, T., 2008. *Micrometeorology*. Springer-Verlag, Berlin Heidelberg. <https://doi.org/10.1007/978-3-540-74666-9>
- Galloway, J.N., Cowling, E.B., 2002. Reactive Nitrogen and The World: 200 Years of Change. *AMBIO: A Journal of the Human Environment* 31, 64–71. <https://doi.org/10.1579/0044-7447-31.2.64>
- Galloway, J.N., Leach, A.M., Bleeker, A., Erisman, J.W., 2013. A chronology of human understanding of the nitrogen cycle. *Philosophical Transactions of the Royal Society B: Biological Sciences* 368, 20130120. <https://doi.org/10.1098/rstb.2013.0120>
- Galloway, J.N., Schlesinger, W.H., Levy, H., Michaels, A., Schnoor, J.L., 1995. Nitrogen fixation: Anthropogenic enhancement–environmental response. *Global Biogeochem. Cycles* 9, 235–252. <https://doi.org/10.1029/95GB00158>
- Gomi, T., 2001. *Everyone Poops, Bound for Schools & Libraries* ed. edition. ed. Turtleback, La Jolla, CA.
- Hacker, J.M., Chen, D., Bai, M., Ewenz, C., Junkermann, W., Lieff, W., McManus, B., Neining, B., Sun, J., Coates, T., Denmead, T., Flesch, T., McGinn, S., Hill, J., 2016. Using airborne technology to quantify and apportion emissions of CH₄ and NH₃ from feedlots. *Anim. Prod. Sci.* 56, 190–203. <https://doi.org/10.1071/AN15513>
- Hanjalic, K., 2005. Will RANS Survive LES? A View of Perspectives. *J. Fluids Eng* 127, 831–839. <https://doi.org/10.1115/1.2037084>

- Hao, X., Chang, C., Janzen, H.H., Hill, B.R., Ormann, T., 2005. Potential nitrogen enrichment of soil and surface water by atmospheric ammonia sorption in intensive livestock production areas. *Agriculture, Ecosystems & Environment* 110, 185–194. <https://doi.org/10.1016/j.agee.2005.04.002>
- Hargreaves, D.M., Wright, N.G., 2007. On the use of the k - ϵ model in commercial CFD software to model the neutral atmospheric boundary layer. *Journal of Wind Engineering and Industrial Aerodynamics* 95, 355–369. <https://doi.org/10.1016/j.jweia.2006.08.002>
- Högström, U., Bergström, H., Smedman, A.-S., Halldin, S., Lindroth, A., 1989. Turbulent exchange above a pine forest, I: Fluxes and gradients. *Boundary-Layer Meteorol* 49, 197–217. <https://doi.org/10.1007/BF00116411>
- Holton, J.R., Hakim, G.J., 2012. *An Introduction to Dynamic Meteorology*, Volume 88, 5 edition. ed. Academic Press, Amsterdam.
- Hristov, A.N., Hanigan, M., Cole, A., Todd, R., McAllister, T.A., Ndegwa, P.M., Rotz, A., 2011. Review: Ammonia emissions from dairy farms and beef feedlots. *Canadian Journal of Animal Science* 91, 1–35. <https://doi.org/10.1139/CJAS10034>
- Launder, B.E., Spalding, D.B., 1974. The numerical computation of turbulent flows. *Computer Methods in Applied Mechanics and Engineering* 3, 269–289. [https://doi.org/10.1016/0045-7825\(74\)90029-2](https://doi.org/10.1016/0045-7825(74)90029-2)
- Li, Y., Schichtel, B.A., Walker, J.T., Schwede, D.B., Chen, X., Lehmann, C.M.B., Puchalski, M.A., Gay, D.A., Collett, J.L., 2016. Increasing importance of deposition of reduced nitrogen in the United States. *PNAS* 113, 5874–5879. <https://doi.org/10.1073/pnas.1525736113>
- Lovejoy, S., Tuck, A.F., Hovde, S.J., Schertzer, D., 2007. Is isotropic turbulence relevant in the atmosphere? *Geophysical Research Letters* 34. <https://doi.org/10.1029/2007GL029359>

- Massad, R.-S., Nemitz, E., Sutton, M.A., 2010. Review and parameterisation of bi-directional ammonia exchange between vegetation and the atmosphere. *Atmos. Chem. Phys.* 10, 10359–10386. <https://doi.org/10.5194/acp-10-10359-2010>
- Nemitz, E., Milford, C., Sutton, M.A., 2001. A two - layer canopy compensation point model for describing bi - directional biosphere - atmosphere exchange of ammonia. *Quarterly Journal of the Royal Meteorological Society* 127, 815 - 833. <https://doi.org/10.1002/qj.49712757306>
- Nemitz, E., Sutton, M.A., Schjoerring, J.K., Husted, S., Paul Wyers, G., 2000. Resistance modelling of ammonia exchange over oilseed rape. *Agricultural and Forest Meteorology* 105, 405–425. [https://doi.org/10.1016/S0168-1923\(00\)00206-9](https://doi.org/10.1016/S0168-1923(00)00206-9)
- Phillips, S.B., Arya, S.P., Aneja, V.P., 2004. Ammonia flux and dry deposition velocity from near-surface concentration gradient measurements over a grass surface in North Carolina. *Atmospheric Environment* 38, 3469–3480. <https://doi.org/10.1016/j.atmosenv.2004.02.054>
- Pollack, I.B., Lindaas, J., Roscioli, J.R., Agnese, M., Permar, W., Hu, L., Fischer, E.V., 2019. Evaluation of ambient ammonia measurements from a research aircraft using a closed-path QC-TILDAS operated with active continuous passivation. *Atmospheric Measurement Techniques* 12, 3717–3742. <https://doi.org/10.5194/amt-12-3717-2019>
- Richards, P.J., Hoxey, R.P., 1993. Appropriate boundary conditions for computational wind engineering models using the k- ϵ turbulence model, in: Murakami, S. (Ed.), *Computational Wind Engineering* 1. Elsevier, Oxford, pp. 145–153. <https://doi.org/10.1016/B978-0-444-81688-7.50018-8>

- Seinfeld, J.H., Pandis, S.N., 2016. *Atmospheric Chemistry and Physics, From Air Pollution to Climate Change*, 3rd ed. Hoboken, NJ.
- Shen, J., Chen, D., Bai, M., Sun, J., Lam, S.K., Mosier, A., Liu, X., Li, Y., 2018. Spatial variations in soil and plant nitrogen levels caused by ammonia deposition near a cattle feedlot. *Atmospheric Environment* 176, 120–127. <https://doi.org/10.1016/j.atmosenv.2017.12.022>
- Shonkwiler, K.B., Ham, J.M., 2018. Ammonia emissions from a beef feedlot: Comparison of inverse modeling techniques using long-path and point measurements of fence-line NH₃. *Agricultural and Forest Meteorology, Greenhouse gas and ammonia emissions from livestock production* 258, 29–42. <https://doi.org/10.1016/j.agrformet.2017.10.031>
- Smagorinsky, J., 1963. General circulation experiments with the primitive equations. *Mon. Wea. Rev.* 91, 99–164. [https://doi.org/10.1175/1520-0493\(1963\)091<0099:GCEWTP>2.3.CO;2](https://doi.org/10.1175/1520-0493(1963)091<0099:GCEWTP>2.3.CO;2)
- Sun, K., Tao, L., Miller, D.J., Khan, M.A., Zondlo, M.A., 2014. On-Road Ammonia Emissions Characterized by Mobile, Open-Path Measurements. *Environ. Sci. Technol.* 48, 3943–3950. <https://doi.org/10.1021/es4047704>
- Sun, K., Tao, L., Miller, D.J., Zondlo, M.A., Shonkwiler, K.B., Nash, C., Ham, J.M., 2015. Open-path eddy covariance measurements of ammonia fluxes from a beef cattle feedlot. *Agricultural and Forest Meteorology* 213, 193–202. <https://doi.org/10.1016/j.agrformet.2015.06.007>
- Sutton, M.A., Burkhardt, J.K., Guerin, D., Fowler, D., 1995. Measurement and modelling of ammonia exchange over arable croplands, in: Heij, G.J., Erisman, J.W. (Eds.), *Studies in Environmental Science, Acid Rain Research: Do We Have Enough Answers?* Elsevier, pp. 71–80. [https://doi.org/10.1016/S0166-1116\(06\)80274-8](https://doi.org/10.1016/S0166-1116(06)80274-8)

- Sutton, M.A., Milford, C., Dragosits, U., Place, C.J., Singles, R.J., Smith, R.I., Pitcairn, C.E.R., Fowler, D., Hill, J., ApSimon, H.M., Ross, C., Hill, R., Jarvis, S.C., Pain, B.F., Phillips, V.C., Harrison, R., Moss, D., Webb, J., Espenhahn, S.E., Lee, D.S., Hornung, M., Ullyett, J., Bull, K.R., Emmett, B.A., Lowe, J., Wyers, G.P., 1998. Dispersion, deposition and impacts of atmospheric ammonia: quantifying local budgets and spatial variability. *Environmental Pollution, Nitrogen, the Confer-N-s First International Nitrogen Conference 1998* 102, 349–361. [https://doi.org/10.1016/S0269-7491\(98\)80054-7](https://doi.org/10.1016/S0269-7491(98)80054-7)
- Svensson, U., Häggkvist, K., 1990. A two-equation turbulence model for canopy flows. *Journal of Wind Engineering and Industrial Aerodynamics* 35, 201–211. [https://doi.org/10.1016/0167-6105\(90\)90216-Y](https://doi.org/10.1016/0167-6105(90)90216-Y)
- Tennekes, H., Lumley, J.L., 1972. *A First Course in Turbulence* [WWW Document]. The MIT Press. URL <https://mitpress.mit.edu/books/first-course-turbulence> (accessed 11.15.19).
- Van Damme, M., Clarisse, L., Whitburn, S., Hadji-Lazaro, J., Hurtmans, D., Clerbaux, C., Coheur, P.-F., 2018. Industrial and agricultural ammonia point sources exposed. *Nature* 564, 99. <https://doi.org/10.1038/s41586-018-0747-1>
- Vitousek, P.M., Aber, J.D., Howarth, R.W., Likens, G.E., Matson, P.A., Schindler, D.W., Schlesinger, W.H., Tilman, D.G., 1997. Human Alteration of the Global Nitrogen Cycle: Sources and Consequences. *Ecological Applications* 7, 737–750. [https://doi.org/10.1890/1051-0761\(1997\)007\[0737:HAOTGN\]2.0.CO;2](https://doi.org/10.1890/1051-0761(1997)007[0737:HAOTGN]2.0.CO;2)
- Vitousek, P.M., Menge, D.N.L., Reed, S.C., Cleveland, C.C., 2013. Biological nitrogen fixation: rates, patterns and ecological controls in terrestrial ecosystems. *Philosophical Transactions of the Royal Society B: Biological Sciences* 368, 20130119. <https://doi.org/10.1098/rstb.2013.0119>

- Wu, Z., Wang, X., Turnipseed, A.A., Chen, F., Zhang, L., Guenther, A.B., Karl, T., Huey, L.G., Niyogi, D., Xia, B., Alapaty, K., 2012. Evaluation and improvements of two community models in simulating dry deposition velocities for peroxyacetyl nitrate (PAN) over a coniferous forest. *Journal of Geophysical Research: Atmospheres* 117. <https://doi.org/10.1029/2011JD016751>
- Zhiyin, Y., 2015. Large-eddy simulation: Past, present and the future. *Chinese Journal of Aeronautics* 28, 11–24. <https://doi.org/10.1016/j.cja.2014.12.007>

CHAPTER 2. LANDSCAPE ENGINEERING TO INCREASE LOCAL AMMONIA RECAPTURE DOWNWIND OF LARGE ANIMAL FEEDLOTS: A MODELLING ESTIMATE

Ammonia emissions from large animal feedlots can have large effects on regional air quality and N_R deposition into sensitive ecosystems. However, it is difficult to quantify the effect of these large sources, due to the complicated processes represented by ammonia atmosphere-biosphere exchanges; other studies have shown that a large fraction of ammonia emitted by these sources may undergo dry deposition within a few km of the feedlot boundary. In this study, we use a modelling system that couples ammonia dispersion with its bidirectional flux with the surface to simulate deposition downwind of a large animal feedlot. We show that changes to the vegetation and other land surface properties next to feedlots have large potential to increase local dry deposition and decrease the net effect of ammonia on the surrounding atmosphere. For example, we find that a having surface of maize crop or forest within the first 1.5 km of the feedlot may remove 30% or 50% of the emitted ammonia, respectively, under our base conditions; in contrast, a surface of exposed soil with no vegetation only removes 2% under the same conditions. However, due to uncertainty in the canopy compensation point, changes in ambient thermodynamic environment, and potential canopy saturation, measurements of canopy and soil nitrogen content are crucial for more-accurately representing this system in models. Finally, while some plant canopies can effectively remove ammonia over a relatively small length of trees (length of 200 m), we demonstrate that narrow tree shelterbelts (length of 10 m) are an ineffective way to increase ammonia deposition, due to their unfavorable effect on turbulent dispersion near CAFOs.

2.1 Introduction

Anthropogenic changes to the global nitrogen cycle can lead to atmospheric and environmental contamination by N_R , commonly in the forms of ammonia, ammonium, nitrate, nitric acid, and NO_x . (Vitousek et al., 2013). N_R , specifically ammonia and nitric acid, can react in the atmosphere to form aerosols, which are known to negatively impact human health (Dockery et al., 1993) and can impact regional and global climate change through a variety of mechanisms (Boucher et al., 2015). Furthermore, N_R availability is a critical parameter in many ecosystems, and as synthetic N_R from anthropogenic nitrogen-fixation processes (i.e. Haber-Bosch process) escape into the environment, increases in N_R can have detrimental effects on soil pH, biodiversity, and broader ecosystem health (Asman et al., 1998; Clark et al., 2018). Additionally, N_R species that deposit in soils can undergo biochemical processes and be re-emitted to the atmosphere as N_2O (Laville et al., 2011; Mosier et al., 1998; Werner et al., 2007), which is a powerful greenhouse gas with a long atmospheric lifetime (Intergovernmental Panel on Climate Change, 2014). While N_R can come from several different types of sources, controls on NO_x emissions from combustion have decreased the importance of oxidized nitrogen species in many regions; however, reduced nitrogen species such as ammonia, which primarily originate from agricultural processes (NEI 2014 <https://www.epa.gov/air-emissions-inventories>), are not subject to the same degree of regulation in the United States (Stephen and Aneja, 2008), and are difficult to monitor and control in regions where regulations do exist, such as Europe; consequently, reduced nitrogen emissions are becoming the dominant source of N_R in many regions, especially regions with agricultural sources (Li et al., 2017, 2016).

The 20th and 21st centuries has seen the emergence of new agricultural practices involving massive commercial animal feedlot operations. The western US contains some of the largest

animal feeding operations on earth, with some beef feedlots having in excess of 100,000 head of cattle. More specifically, the total beef and dairy cattle population on the Colorado Front Range (CFR) exceeds 2 million head of cattle, and are valued at approximately \$2.8 billion (“Colorado Cattlemen’s Association,” 2019). Despite regional and national decreases in oxidized N_R deposition, vulnerable alpine ecosystems in the nearby Rocky Mountains have experienced steady increases in total N_R deposition, suggesting that these ammonia hotspots are important sources. Beyond this specific example, other large AFOs with 20,000+ head of cattle are located in the Western US (Baum et al., 2008; Miller et al., 2015), as well as Australia (Shen et al., 2018, 2016) and Canada (Hacker et al., 2016; McGinn et al., 2016, 2007; Staebler et al., 2009); large point sources of ammonia are now visible from space (Damme et al., 2018).

Despite their size, the importance of these major ammonia sources for regional N_R deposition and air quality is poorly constrained. The impact of CAFOs on regional N_R deposition and air quality is a function of four processes: emissions, dispersion and transport through the atmospheric boundary layer, atmospheric chemical processing, and surface interaction. Emissions from feedlots are dynamic and vary according to environmental conditions such as temperature (T), relative humidity (RH), atmospheric stability, and windspeed, and also depend on management practices such as cattle diet and facility maintenance practices; however, emissions have been well-studied from observational approaches as well as the development of process-based and empirical models (Hristov et al., 2011; Shonkwiler and Ham, 2018; Sun et al., 2015, 2014). Likewise, the gas-phase chemical processing of gas-phase ammonia (oxidation or aerosol partitioning) is well-understood (Seinfeld and Pandis, 2016). However, ammonia surface fluxes are not as well constrained (Walker et al., 2019). Ammonia atmosphere-surface fluxes are a bidirectional process governed by a series of physical and biological processes (Flechard et al.,

2015). The surface compensation point is a function of ammonia thermodynamics in plant tissue and soil, and is regulated by biological activity, while the mass-transfer efficiency, or mass conductance, is a function of turbulent transport, quasi-laminar boundary layer thickness and diffusion rate within the plant canopy (Massad et al., 2010). While some of these processes are well-represented by dry-deposition parameterizations (Wu et al., 2018), many of the biological processes, such as ammonia uptake by plant stomata and soil or dry deposition in leaf cuticle, can dominate the uncertainty in the surface-atmosphere exchange of ammonia (Wu et al., 2012). These processes vary tremendously in magnitude and depends on fine-scale variability in surface land cover, which often produces large amounts of uncertainty, as well as variability in dry-deposition estimates in systems where the underlying bidirectional flux models are not well-constrained (Dennis et al., 2013). Because direct measurements of ammonia deposition downwind of large sources are difficult to perform, (Ellis et al., 2010; Pollack et al., 2019; Whitehead et al., 2008; Flesch et al., 2007), other approaches towards estimating the ammonia deposition requiring and bidirectional flux models are typically used (i.e. Shen et al., 2017; Shen et al., 2018; McGinn et al., 2011). Therefore, there is a need to better understand the breadth of ammonia deposition ranges close to these major sources, and an opportunity to leverage the variability to engineer agricultural systems that can favorably increase local ammonia recapture to protect more vulnerable ecosystems and airsheds downwind.

The purpose of this study is to use a modelling system that couples ammonia dispersion with bidirectional surface fluxes to quantify the ammonia deposition downwind of a CAFO-like source under different surface conditions. In this study, we identify critical parameters within ammonia bidirectional flux models that can have the greatest effect on model-based estimates of ammonia deposition adjacent to CAFOs, and quantify the effect that these parameters have on

deposition. First, we use an open-source computational fluid dynamics (CFD) model to produce estimates of turbulent flow downwind of a feedlot for different land-use types. We use the output from the CFD model to generate trajectories for a lagrangian stochastic bidirectional exchange model to quantify the interaction of the ammonia plume with vegetation downwind of the feedlot. For our base case scenarios, we find that the modeled deposition on grass well-reproduces the observed deposition in what few measurements are available in the literature. However, we find that growing large crops such as maize downwind of feedlots has the potential to dramatically increase the deposition by an order of magnitude, though this is highly sensitive to the assumptions about parameters that govern the thermodynamics and in-canopy mass-transfer processes that determine the compensation point. Finally, we explore the use of windbreaks and shelterbelts as techniques for increasing local ammonia recapture but minimizing the land-use change required to implement them. In Section 2.3, we describe the modelling results; however, the discussion of the results is in Section 2.4.

2.2 Methods

2.2.1 K-Epsilon Modelling with OpenFOAM

In this study, we use OpenFOAM to produce trajectories for the Lagrangian-Stochastic model. OpenFOAM is an open-source modelling system for computational fluid dynamics (CFD) applications. In this study, we use OpenFOAM in Reynolds-Averaged Navier-Stokes (RANS) configuration to numerically solve the k-epsilon equations; we use this model configuration to simulate atmospheric turbulence upwind of, above, and through a plant canopy. The canopy is represented as a porous medium, where porosity is inversely proportional to the leaf area density (LAD). The canopy behaves as a source for turbulent kinetic energy (K) and turbulent kinetic

energy dissipation (epsilon), and is parameterized using Dalpe-Masson source functions (Dalpe and Masson, 2007). The Dalpe-Masson functions are designed for flow effects at plant canopy boundaries. Additionally, the OpenFOAM implementation uses wall functions tuned for application to the atmospheric boundary layer to represent the effect of the surface on the flow (Hargreaves and Wright, 2007). The implementation of the k-epsilon model with the aforementioned source and wall functions has been evaluated against field measurements from a forest edge (Irvine et al., 1997), and show typical agreement for K-epsilon simulations through plant canopies (Segersson, D., 2017). More generally, various implementations of k-epsilon models have been used to simulate the atmospheric boundary layer (Hargreaves and Wright, 2007; Richards and Hoxey, 1993), especially in the context of simulating dispersion above and through plant canopies (Hanjalic, 2005; Segalini et al., 2016; Svensson and Häggkvist, 1990). K-epsilon simulations are only able to simulate neutral atmospheric stability conditions, so most of the modelling results only pertain to the neutral atmospheric boundary layer; we explore the sensitivity of our results to this assumption using Monin-Obukhov theory.

2.2.2 Lagrangian-Stochastic Ammonia Dispersion and Bidirectional Flux Modelling with MODDAS

We coupled OpenFOAM to MODDAS, a Lagrangian-Stochastic/atmosphere-biosphere exchange model to calculate the ammonia dispersion and deposition. MODDAS uses the mean winds U and W to determine the particle advection scheme, as well as information about the turbulence to calculate the dispersion TKE (k), as calculated from OpenFOAM, to estimate σ_u and σ_w according to Equation 2.1:

$$\sigma_u = C_u \sqrt{2k} ; \sigma_w = C_w \sqrt{2k} \quad (2.1)$$

where C_u and C_w are empirical constants with values of 0.726 and 0.368 respectively. We then calculate the Lagrangian timescale according to Equation 2.2:

$$\tau_{Lu} = 2 \frac{\sigma_u^2}{3.12\epsilon}; \quad \tau_{Lw} = 2 \frac{\sigma_w^2}{3.12\epsilon} \quad (2.2)$$

where epsilon is also read from OpenFOAM. MODDAS then uses U , W , τ_{Lu} , and τ_{Lw} to generate trajectories that originate in every model grid cell, are advected by U and W streamlines, and deviate from the mean wind streamline according to the size of τ_{Lu} , and τ_{Lw} in a grid cell multiplied by a stochastic operator. This process is repeated for enough particles to populate a dispersion matrix D which represents the dispersion function connecting two grid cells inside the model domain. The concentration at a given point is given by Equation 2.3:

$$C = \int_{x_s, y_s, z_s} S(x_s, y_s, z_s) D(x, y, z | x_s, y_s, z_s) dx_s dy_s dz_s \quad (2.3)$$

where S represents all types of sources: background ammonia concentration from the upwind model boundary, area source representing the CAFO, plant canopy emissions, and plant canopy deposition. Because of the superposition principle, we are able to split this equation by source types in order to separately model the different behavior. In this system, the upwind model boundary, which represents the ambient background concentrations, is constant with height, while the CAFO source is emitted from the model surface at constant uniform emission flux. The plant canopy source undergoes bidirectional flux processes, which are modelled by resistor networks analogous to electrical conductivity, and compensation point behavior. The model that is used is well-summarized in Loubet et al., (2006), with detailed information about model parameters in Massad et al., (2010). In the context of MODDAS, the bidirectional flux process can be split into two separate processes. Therefore, we can reorganize Equation 2.3 as shown in Equation 2.4:

$$C = C_{bkg} + \int_{x_{CAFO}} S_{CAFO} D dx_{CAFO} + \int_{x_{CAN}} S_{CAN,emit}(x_{CAN}) D dx_{CAN} + \int_{x_{CAN}} S_{CAN,dep}(x_{CAN}, C) D dx_{CAN} \quad (2.4)$$

Where C_{bkg} represents the ambient background, the integral over X_{CAFO} represents the feedlot area source with S_{CAFO} being a constant emission flux, and the remaining two terms represent the canopy emission and canopy deposition, respectively. While the first three terms can be solved prognostically, the canopy deposition term is a function of the atmospheric concentration, and therefore the dispersion matrix must be inverted to solve for deposition in this modelling framework.

MODDAS has been used to simulate dispersion and deposition of ammonia from agricultural sources such as fertilized crops (Loubet et al., 2003; Marceau et al., 2012), ammonia hotspots (Loubet et al., 2009), and pollen dispersion (Jarosz et al., 2004, 2003). Furthermore, MODDAS has been used to test agroforestry ammonia sequestration strategies (Bealey et al., 2014). However, we are applying these modelling tools to much larger CAFOs, with concentrations of ammonia, and consequently surface fluxes, that are much more extreme than the scenarios simulated in Bealey et al., (2014), as well as on a model domain that is an order of magnitude larger in spatial extent. Furthermore, this study is the first instance we know of that has coupled MODDAS with an open-source CFD package and performed the simulations in a high-performance computing environment. For more detail on the physics, flux parameterizations, and numerical implementation, refer to Loubet et al., (2006); many parameter values and guidelines for parameter estimation can be found in Massad et al., (2010).

2.2.3 Simulation Configuration and Parameters

In this study, all simulations were performed in a two-dimensional domain, where x is aligned with the mean wind direction and z is perpendicular to the surface. We perform simulations on three different domain configurations. Configuration 1 was our base domain setup, while Configuration 2 was used to conduct the atmospheric stability sensitivity test (discussed below),

and Configuration 3 was used to investigate the effect of shelterbelts. The canopy types and positions for the three different model configurations are illustrated in Figure 2.1. In Configuration 1, the OpenFOAM simulation domain spans $x = -320$ m to 2540 m with 1500 grid cells, and $z = 0$

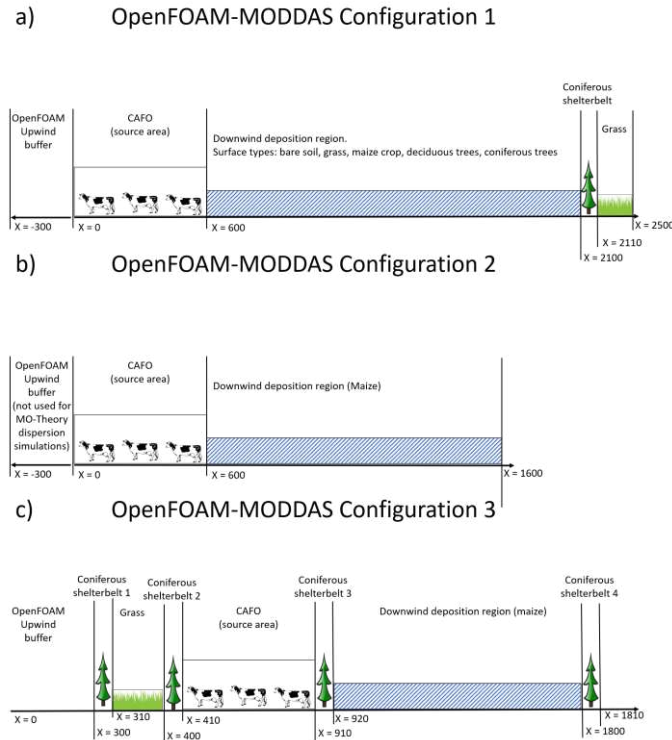


Figure 2.1: Simulation domain configurations for (a) the base-case simulations, (b) the stability test simulations, and (c) the shelterbelt positioning simulations.

to 500 m with 300 grid cells. The grid cells in the x direction are identical, while the z grid cells use simple grading with grid cells at the model top a factor of 20 larger than grid cells at the model surface; therefore, vertical grid cells at the model surface are 0.14 m thick, and 8 m thick at the model top. For the MODDAS simulations, the model resolution is coarsened to 800 horizontal grid cells spanning 2500 m; the same z grid aspect ratio and number of cells is used; however, 25 grid cells are guaranteed to be inside the bottom 20 m of the model domain to represent the plant canopy, which produces slightly different spacing between the vertical model layers. MODDAS uses linear interpolation to regrid the OpenFOAM output to the appropriate MODDAS grid. Model Configuration 2 uses 450 x 250 grid cell spacing to span $x = -320$ m to 1640 m, $z = 0$ to 500 m for

the OpenFOAM control case; however, for the other stability cases, MODDAS used vertical profiles estimated from Monin-Obukhov theory which assume U and K profiles as a function of Monin-Obukhov length, wind speed at a reference height, and the model roughness length. For these cases, the vertical extent of the domain was limited to 300 m, and the grid cell dimensions were 300 x 75. Simulation Configuration 3 uses the same vertical configuration as Configuration 1, but the horizontal domain spans $x = -320$ to 1540 m with 800 grid cells, with no reduction in grid cell number in the MODDAS simulations. For all simulations, the upwind boundary conditions are modelled as follows: horizontal windspeed (U) is initialized with a logarithmic wind profile of 6.17 m s^{-1} at 15 m above the surface, while vertical wind (W) was set to 0, and k and epsilon are initialized using inlet profiles specified in Hargreaves and Wright, (2007). We allow 300 m of empty model domain with surface roughness parameter $z_0 = 0.06 \text{ m}$ upwind of the first plant canopy feature.

The plant canopies are represented as a porous media, where the porosity is inversely proportional to the Leaf Area Density (LAD). LAD profiles for grass and maize, as well as plant height (H) and Leaf Area Index (LAI) were previously used with MODDAS, and are adapted from Loubet et al., (2009); the LAD profiles, LAI, and H for the coniferous and deciduous canopies are taken from (Teske and Thistle, 2004). The parameter values used are reported in Table 2.1, and the normalized LAD profiles are included in Appendix A. In addition to the LAD, LAI, and H, the plant canopies also use parameters for the ammonia bidirectional flux model. These parameters are included in Table 2.1. The base-case environmental conditions, including T, RH, photosynthetically active radiation (PAR), time of day, simulation latitude, atmospheric stability, as well as the source length and emission flux, are summarized in Table 2.2. In OpenFOAM, the CAFO is represented as a porous media using the same set of parameters as a plant canopy; the

equivalent LAD profile apportions most of the near the surface below 1 meter, with minor obstructions further from the surface, the total height of the CAFO is modelled as 2 m, and the equivalent LAI (analogous to the total porosity of the CAFO) is 1.0. The analogous LAD profile for the CAFO is also included in Appendix A.

Table 2.1: Parameters that are used to calculate canopy compensation point and resistance terms in the bidirectional flux model, sorted by surface type.

Parameter	Units	Bare Soil	Grass	Maize	Deciduous	Coniferous
H (canopy height)	m	--	0.5	2.5	25.75	19.3
LAI (leaf area index)	--	--	2.0	4.5	3.29	6.12
Γ_s (stomatal emission potential)	--	N/A	800	1186	600	1300
Γ_g (ground emission potential)	--	360	360	13000	20	20
$R_{w,min}$ (minimum cuticular resistance)	$s\ m^{-1}$		30			
$R_{w,\beta}$ (cuticular resistance exponent parameter)	--		2.7			
$R_{s,min}$ (minimum stomata resistance)	$s\ m^{-1}$		60			
$R_{s,\beta}$ (cuticular resistance exponent parameter)	--		7			

To test the sensitivity of the modelled results to atmospheric stability, we conducted simulations with model Configuration 2 (Figure 2.1b). For these simulations, we conducted a controlled case using the OpenFOAM k-epsilon, but also used wind and TKE profiles determined by Monin-Obukhov theory for stability classes A-F (Irwin, 1979). We test the sensitivity of the model results to the canopy compensation point using model Configuration 1 (Figure 2.1a), maize case, where we varied the emission potential Γ_s from the base value 1186 up to 33208, as well as the atmospheric T from 8 to 26 °C, and RH from 75% to 30%.

Table 2.2: Global environmental parameters for base-case simulations.

Environmental Variable	Model Configuration 1	Model Configuration 2	Model Configuration 3
T [degrees C]	8 - 26	8	8
RH [%]	70 - 30	30	30
U at 15 m [m s ⁻¹]	6.8	6.8	6.8
Atmospheric Stability	Neutral	A-F	Neutral
Time of day [Local Standard time]	1300	1300	1300
Degrees Latitude	45	45	45
Photosynthetically Active Radiation [w m ⁻²]	600	600	600
Source Length [m]	600	600	500
Source Emission Flux [μg m ⁻² s ⁻¹]	100	100	100

2.3 Results

2.3.1 OpenFOAM Simulations

In Figure 2.2, we show the simulated interaction between the wind and various roughness features on the surface for model Configuration 1, with a maize collection region downwind of the CAFO. At an x coordinate 0, the plume encounters the CAFO, which is dense below 1 meter and porous from 1-2 meters. Frictional losses at the surface cause the wind speed to decrease and the turbulent kinetic energy to increase inside and directly above the CAFO, and this wake effect propagate upwards away from the surface, with noticeable slowing of the winds 18 m away from the surface. At x = 600, the flow encounters the maize field adjacent to the CAFO, which produces

more intense wake effects, as the maize is a rougher, less porous surface than the CAFO, and is also 0.5 meters taller. Wind speed and TKE decrease rapidly inside the maize canopy, and a stronger wake effect propagates upward. Finally, at $x = 2100$, the flow encounters a 10-m thick coniferous band of trees (i.e., a “shelterbelt”). The shelterbelt produces the most intense wake effects, with decreases in U and TKE located within and directly downwind of the trees ($x = 2120$) with decreases in U and increases in K propagating far away from the surface.

In Figure 2.3, we show vertical profiles of each turbulent variable at important positions in the model Configuration 1 domain. From top to bottom, the rows show U , W , TKE, and $C0\varepsilon$ (normalized ε). From left to right, the columns show the vertical profiles at $x = 200$ (over the CAFO), $x = 585$ (over the CAFO, but close to the interface with the downwind deposition region), $x = 615$ (over the downwind deposition region), $x = 2080$ (before the shelterbelt feature), $x = 2120$

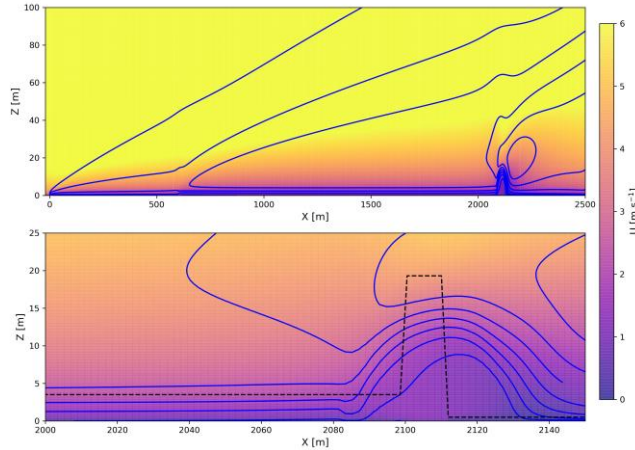


Figure 2.2: Wind and turbulent kinetic energy (colors and contours, respectively) from OpenFOAM simulation, configuration 1, maize canopy case. The top shows the entire model domain, the bottom panel is zoomed in on the downwind coniferous treebelt feature.

(downwind of the shelterbelt feature), and $x = 2500$ (at the model outlet). In each of the Configuration 1 simulations, there is no difference in any of the vertical profiles at $x = 200$ (Figure 2.3, first column). However, slightly upwind of the deposition region, significant differences

emerge between the simulations with trees downwind (e.g. “deciduous” and “coniferous”) vs the other simulations (“baresoil”, “grass”, and “maize”). In both of the tree cases, U decreases, while W and TKE increase upwind of the interface with the trees as the mean flow is directed over the

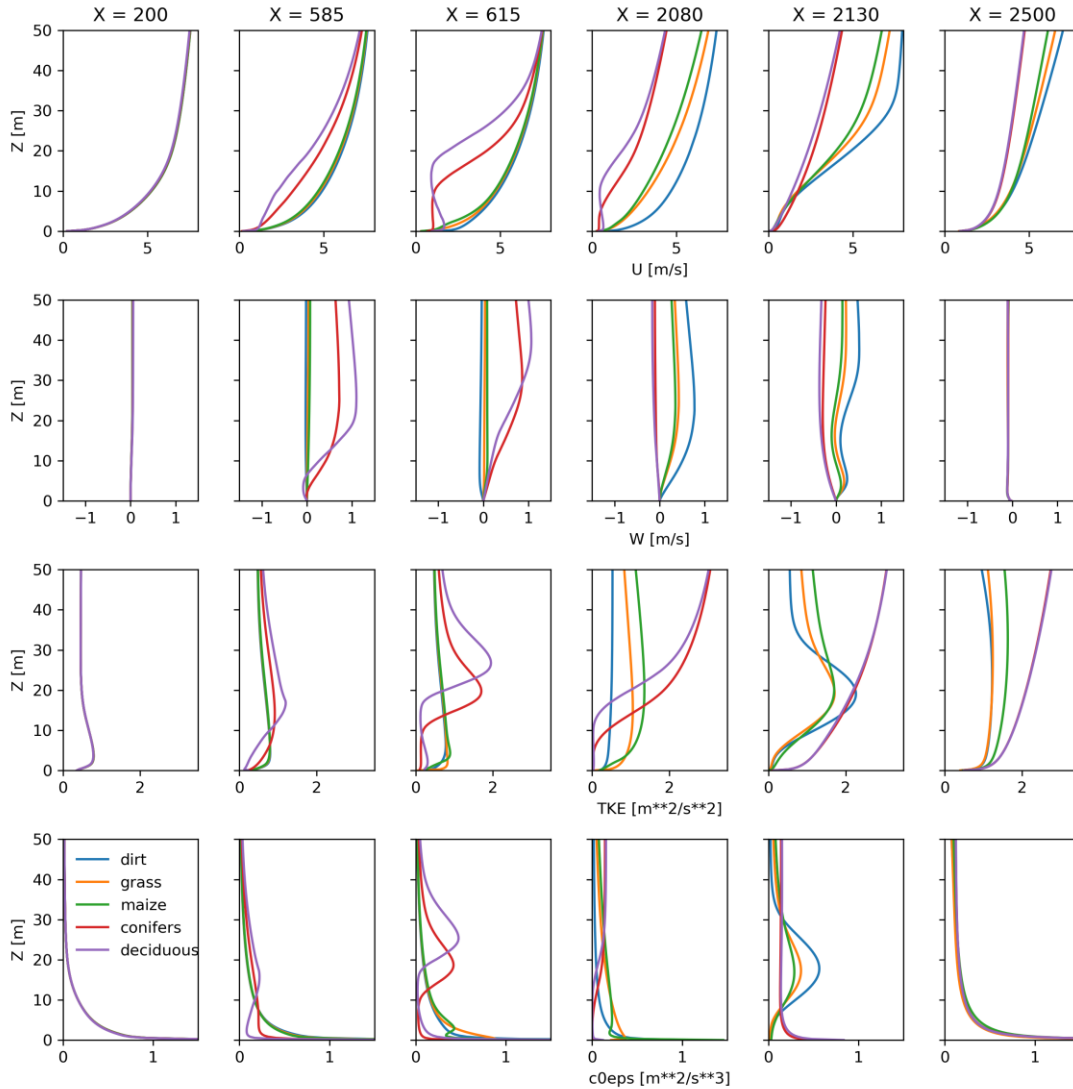


Figure 2.3: Vertical profiles of U , W , k , and $C0\epsilon$ for the simulation Configuration 1 at upwind and downwind positions of major model domain features: , plotted at $x = 200m$ (over the CAFO), $x = 585$ and $615m$ (before and after the CAFO boundary), $x = 2080$ and $2130m$ (before and after the 10m-thick coniferous tree band at $x = 2100-2110m$) and at the simulation outlet ($x = 2500m$).

densest part of the respective plant canopies. Over the downwind deposition region ($x = 600$ — 2100), the wind and turbulent kinetic energy are quickly dampened where the plant canopy is

thickest; this is most obvious in the tree simulations which have the tallest plant canopies, but also occurs inside the 2.5 m high maize and 0.5 m high grass canopies as well. The TKE profiles show that turbulence is produced above and below the densest regions of the canopy, which are different for the coniferous LAD profile and the deciduous LAD profile. Finally, $C0\varepsilon$ is highest where TKE is highest inside the plant canopy. Further downwind ($x = 2080$), most of the in-canopy wind and TKE has been dampened, though there is TKE production on the top of both tree canopies. There are also more noticeable differences in the U, and TKE profiles between the maize simulations as compared to the grass and baresoil simulations. There is also an increase in W for the three simulations without trees as the mean flow is redirected over the shelterbelt feature ($x = 2100 - 21,010$). Downwind of the shelterbelt, there are familiar wake effects: decreases in U, negative W forming a downdraft on the downwind side of the trees, TKE production above and below the densest LAD in the shelterbelt canopy, and decreases in TKE close to the surface due to dissipation. The tree simulations have the noticeably slower winds more than 50 m from the surface as compared to the treeless simulations, but also have noticeably higher TKE. Finally, at the model outlet, the simulations seem to have converged, or are close to converging, as they spin down over an identical grass surface, though the tree simulations still have lower surface winds and higher TKE values relative to the simulations with trees.

2.3.2 MODDAS Landuse Simulations

Next, we present the output from MODDAS simulations that use the OpenFOAM turbulence output to produce the dispersion matrix in Equation 2.5. In Figure 2.4, we show the surface concentrations for two example cases (maize vs baresoil), the 2-D atmospheric concentration of ammonia downwind from the CAFO for the maize case, and the 2-D difference between the maize and baresoil simulations (panels a, b, and c respectively). Both the maize and

baresoil simulations show atmospheric concentrations of $1500 \mu\text{g m}^{-3}$ at the surface at the downwind boundary of the CAFO. Both simulations exhibit similar behavior in that the ammonia concentration decreases with increasing distance downwind of the CAFO. This is due to two physical processes: dilution as the ammonia plume undergoes vertical dispersion and deposition. At the domain outlet, the baresoil and maize simulations have relatively similar decreases in the concentration of ammonia (203 and $104 \mu\text{g m}^{-3}$, a 13 and 7 percent of the CAFO boundary

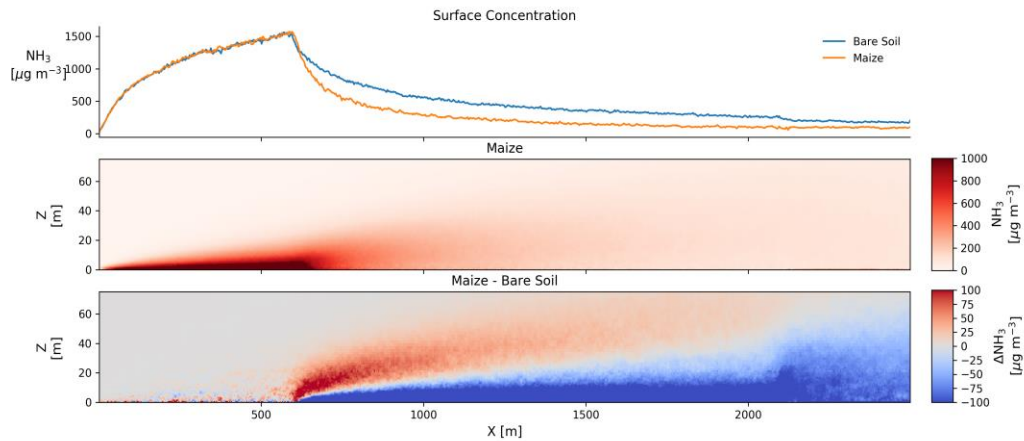


Figure 2.4: (a) surface NH_3 concentration for bare soil and maize, (b) NH_3 concentrations as a pcolor plot within 70 m of the surface for the maize simulation case; and (c) the concentration difference between maize and bare soil simulation cases.

concentration), and are different from each other by a factor of 2. In Figure 2.4c, we show the difference in concentration between these two cases. In the maize case, the surface concentrations are much lower than the baresoil simulation, due to increased deposition and increased vertical mixing. The higher concentrations far from the surface in the maize case are due to the comparatively rougher surface producing higher amounts of TKE and a stronger updraft on the upwind edge of the maize canopy, as compared to the baresoil case.

In Figure 2.5, we show the deposition flux each x coordinate for the simulated surfaces in model Configuration 1 (panel a), as well as the integrated deposited ammonia normalized by the CAFO emissions (panel b). In Figure 2.5a, the deposition flux is as high as $160 \mu\text{g m}^{-2} \text{s}^{-1}$ for the

coniferous forest, and $60 \mu\text{g m}^{-2} \text{s}^{-1}$ for maize; the deposition flux for grass is comparatively much smaller ($10 \mu\text{g m}^{-2} \text{s}^{-1}$ at the CAFO fenceline). However, the depositional fluxes decrease rapidly

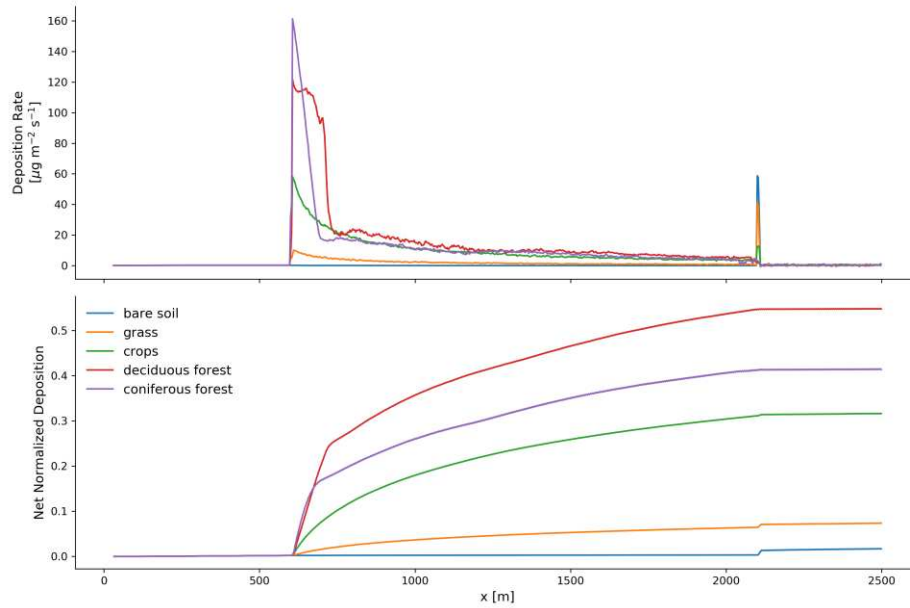


Figure 2.5: (a) the deposition flux and (b) the net fractional ammonia recapture (normalized by CAFO emissions) plotted as a function of x , where the CAFO boundary occurs at $x = 600$ m.

within 500 meters of the CAFO boundary, and at the upwind boundary of the shelterbelt at $x = 2100$ m, all of the simulations exhibit a depositional flux that is similar in magnitude. Passing through the shelterbelt, each simulation has a local increase in dry deposition that is entirely driven by the surface concentrations that pass through the shelterbelt. In Figure 2.5b, we show that around 50% of the total CAFO emissions can be recaptured by a deciduous forest in these simulated conditions. Similarly, the coniferous simulation results in 40% ammonia recapture, despite a higher initial deposition flux. The maize simulation results in 33% ammonia recapture, the grass simulation results in 10%, while the bare soil simulation results in 2%.

2.3.3 Model Sensitivity Analysis

Next, we present results from our analysis of the model sensitivity to the canopy compensation point, which is governed by three parameters: Γ , T , and RH. We conducted

simulations for 4 values of T and RH, across 8 values of Γ_s ; the complete results are summarized in Appendix A. In Figure 2.6, we show the ammonia deposition flux and recapture percentage (a and b, respectively) for 4 different values of Γ from two sets of conditions: cool and moist base-

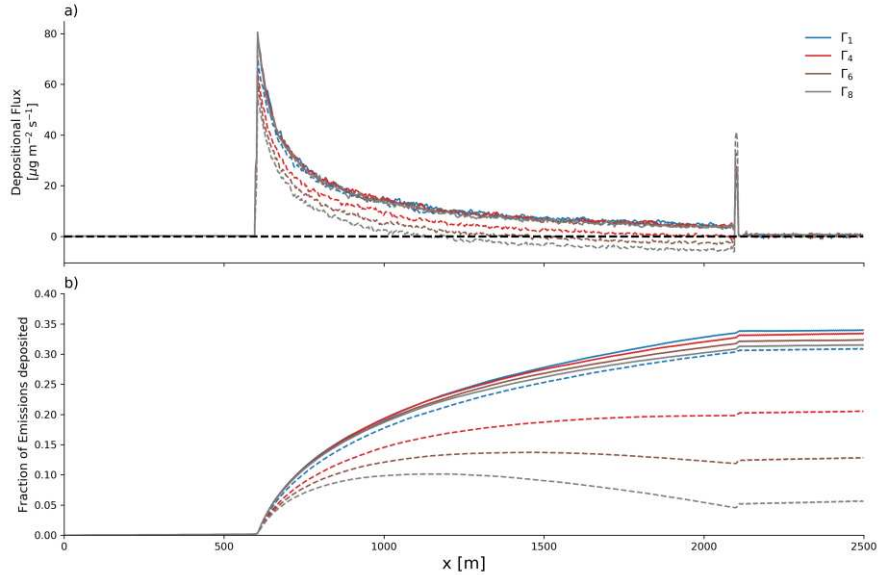


Figure 2.6: Ammonia deposition flux (a) and recapture fraction (b) for four different values of gamma. The base-case thermodynamic environment ($T = 8$ C, $RH = 75\%$) is plotted in solid lines, while the hot-dry case ($T = 26$ C, $RH = 30$ C) is plotted in the dashed lines.

case conditions, and under hot and dry conditions. For the base case environmental T and RH, the ammonia recapture fraction for Γ_1 is 33% for this model configuration the same as we report above, while the value for Γ_8 is 31%. Under hot and dry conditions, the net ammonia recapture for Γ_1 is 30.5%. However, for Γ_8 , the net recapture percentage is 4.5%. Furthermore, the deposition flux becomes negative at $x = 1200$ m, implying that within 600 m of the source boundary, the plant canopy has become a source of ammonia to the atmosphere.

Figure 2.7a shows the ammonia recapture (represented by the colorbar) for the base-case value of Γ (i.e., Γ_1) as a function of T and RH along the x and y axes. Figure 2.7b shows analogous plots for Γ_8 , the largest emission potential used in this study. In Figure 2.7c, the difference between these two cases is shown. For low T and high RH, the value of Γ does not impact the ammonia recapture fraction in this model configuration (difference $<0.02\%$). However, for high T, the

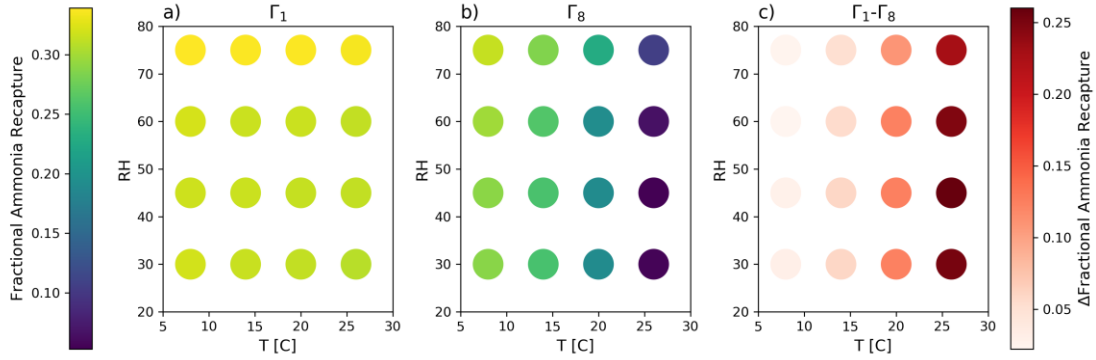


Figure 2.7: Ammonia deposition flux (a) and recapture fraction (b) for four different values of gamma. The base-case thermodynamic environment ($T = 8 \text{ }^\circ\text{C}$, $\text{RH} = 75\%$) is plotted in solid lines, while the hot-dry case ($T = 26 \text{ }^\circ\text{C}$, $\text{RH} = 30\%$) is plotted in the dashed lines.

ammonia recapture is as much as 25% less, corresponding to a net recapture of less than 5% for the Γ_8 simulations. The ammonia recapture fraction has low sensitivity to RH across all values of Γ and T .

In addition to the compensation point sensitivity analysis, we present results from assessing the sensitivity to assumptions about the atmospheric stability. The stability sensitivity simulations were conducted using model Configuration 2, and therefore cannot be easily compared to the results from previous simulation configurations. The total-domain fractional ammonia recapture for simulations under each of the Pasquill Stability classes, along with a neutral (class D) K-epsilon simulation to serve as a control, are shown in Table 2.3.

Table 2.3: Impact of stability on ammonia recapture fraction.

Stability Class	(Obukhov Length)	Fractional Ammonia Recapture (relative to K-epsilon simulation)
A: Strongly unstable	($L = -2.5 \text{ m}$)	0.35% (5%)
B: Unstable	($L = -4.5 \text{ m}$)	0.36% (5%)
C: Moderately unstable	($L = -13.5 \text{ m}$)	0.78% (12%)
D: Neutral	($L = -10000 \text{ m}$)	3.48% (-53%)
E: Moderately stable	($L = 50 \text{ m}$)	6.15% (94%)
F: Stable	($L = 20 \text{ m}$)	7.64% (116%)
K-epsilon Simulation (D)		6.52% (--)

2.3.4 Effect of Shelterbelts

In Figure 2.8, we present results from the shelterbelt simulations. These simulations use model Configuration 3 (Figure 2.1c); In Figure 2.8a, we show that the simulations with trees upwind of the source have higher concentrations further from the surface and lower concentrations of ammonia close to the surface relative to the control case with no trees. Figure 2.8b shows the

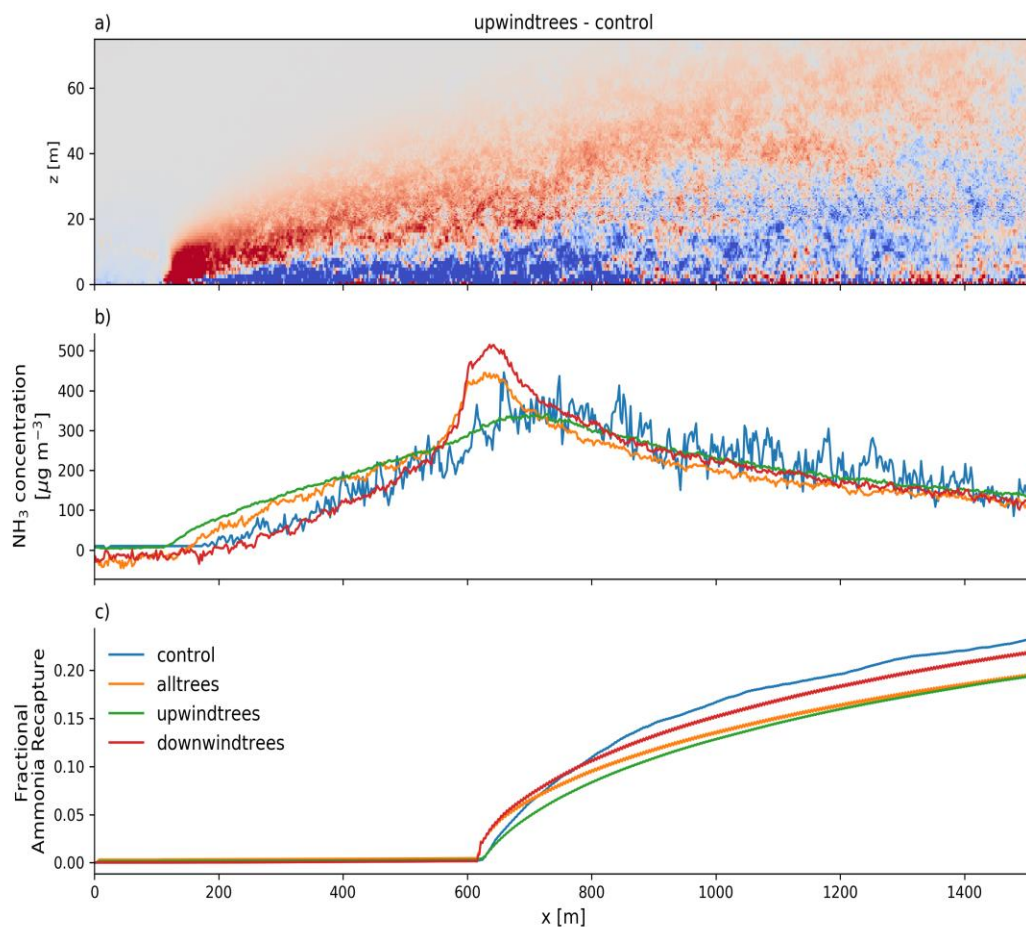


Figure 2.8: (a) Concentration difference between the control simulation with no trees, and the simulation with trees upwind of the source; (b) the surface concentrations from all four of the shelterbelt experiments; and (c) the fractional ammonia recapture by each of the model simulations.

surface concentrations for all four simulations. The concentration over the source is highest in the simulation cases with trees upwind of the source (“upwindtrees” and “alltrees”); however, the simulations with trees on the downwind barrier (“alltrees” and “downwindtrees”) have higher surface concentrations of ammonia than the other two simulations. Over the maize surface, however, the control simulation has the highest concentration of ammonia at the surface. In Figure 2.8c, we see that the control case has the highest recapture fraction of all of the simulations, although the “downwind” case becomes almost equivalent at the shelterbelt located at the domain outlet. The control case achieves 23% recapture over the 1 km maize deposition zone, while the other three simulations all are between 23% and 19% total recapture.

2.4 Discussion

2.4.1 OpenFOAM Simulations

In Section 2.3.1, we demonstrate the effect that plant canopies have on the U and W wind components, as well as the turbulent kinetic energy. The interaction is driven by three main processes: conservation of momentum and interaction of the mean wind with the plant canopy, the production of turbulence by frictional effects and interaction with the plant canopy, and the dissipation of turbulence. While the entire model, including parameter values, is explained in detail in Dalpe and Masson (2007), we reproduce the three source functions for momentum, K, and epsilon respectively:

$$S_{u,i} = -\rho C_d \alpha |u| u_i \quad (2.5)$$

$$S_k = \rho C_d \alpha [\beta_p |u|^3 - \beta_d k |u|] \quad (2.6)$$

$$S_\epsilon = \rho C_d \alpha \frac{\epsilon}{k} [C_{\epsilon 4} \beta_p |u|^3 - C_{\epsilon 5} \beta_d k |u|] \quad (2.7)$$

where ρ is the fluid density, α is the LAD, and β_i and C_i are empirical constants. As the unperturbed flow encounters the plant canopy (where $\alpha > 0$), the flow slows. This results in higher pressure on the upwind edge of the plant canopy, which produces an updraft, guiding flow over the canopy edge, while producing shear, which in turn produces turbulent kinetic energy on the upwind boundary of the plant canopy. The source term for epsilon is proportional to k , meaning that regions with when the plant canopy encounters highly turbulent flow, the turbulence is less efficiently dampened (i.e., epsilon production is lower) than when the TKE dissipation rate is already high. Consequently, epsilon increase occurs further downwind after the flow encounters the plant canopy, as the k/ϵ ratio increases.

These effects can be seen in Figure 2.2, where the horizontal wind speed slows and TKE increases and propagates upward through the domain; in addition to the source functions, TKE and epsilon are advected by the mean flow, and are produced in the flow field by viscous processes, as shown by the k -epsilon model equations (Launder and Spalding, 1983); the viscous production and dissipation of TKE are slower than the production by interaction with the plant canopy. In Figure 2.3, we show vertical profiles of all variables at each of the important interfaces within the model domain; the decrease in U can be seen as the the flow encounters new obstacles. Specifically, we see the near-surface decrease in U as a result of surface roughness, the increases and decreases in W on the upwind and downwind edges of the shelterbelt ($x = 2080$ and 2130), the production of TKE when high U flow first encounters the canopy features, and the ultimate dampening of in-canopy TKE by the continual production of ϵ .

There are three main implications for the effect of the plant canopy on the turbulent flow processes for the downwind ammonia bidirectional fluxes in this context: (1) upwind and downwind canopy features such as shelterbelts can slow the horizontal wind speed near the surface,

increasing the residence time of the ammonia emissions over the surface, but (2) the canopy features also increase the turbulence near the surface and can increase the rate of dilution as the plume mixes further away from the surface, and (3) plant canopies produce an updraft on the upwind boundary which can redirect the ammonia plume over the plant canopy. This is consistent with the findings of many studies of turbulence on forest edges (Dalpe and Masson, 2007). A key finding from this study is that designing too dense of a plant canopy adjacent to the ammonia prevents the ammonia plume from penetrating deep into the vegetated volume. In our simulations, the in-canopy U and TKE for the densest plant canopies simulated (maize, deciduous, and coniferous trees) are efficiently dampened by the dense vegetation. While the vegetation inside the plant canopy is thermodynamically favorable for absorbing ammonia from the atmosphere, the low U and TKE may inhibit the mass transfer of the ammonia plume deep inside a dense canopy. Bealey et al., (2014), who have used similar methodology to analyze the ammonia recapture potential found that plant canopies that are too dense redirect most of the ammonia plume over the plant canopy. The optimal scenario from their study was a porous, low-LAI plant canopy adjacent to the feedlot, with a denser “backstop” to prevent the plume from passing through the plant canopy. However, the downwind plant canopies that we simulate are considerably longer (1500 m) than the Bealey et al., (2014) case (100 m), negating the need for a backstop. Taking only the mass transfer into account, the optimal canopy layout is one that reduces the surface wind speed downwind of the CAFO, minimizes the turbulence, and minimizes the updraft strength on the upwind boundary of the CAFO to allow the ammonia plume to penetrate the plant canopy. We will expand upon the ammonia depositional processes within the MODDAS model next.

2.4.2 MODDAS Simulations; Important Parameters and Model Sensitivity

Next, we discuss the results from the MODDAS simulations. As we showed in Section 2.3.2 (from Figure 2.3), we see that for all cases, the ammonia concentration at the surface decreases (Figure 2.4); this is due to dilution of the ammonia plume, as well as deposition, which we show in Figure 2.5. Many studies have made measurements of ammonia concentrations at various distances from feedlots ((Miller et al., 2015; Shonkwiler and Ham, 2018; Sun et al., 2015, 2014); given the size of our CAFO, an atmospheric concentration of $1500 \mu\text{g m}^{-3}$ is typical for the concentrations at the fence line, and a concentration between 20 (deciduous forest) and 200 (bare soil) $\mu\text{g m}^{-3}$ are within the range of expected values for 1.5 km from a major feedlot boundary. However, comparatively few studies have characterized ammonia deposition at multiple distances downwind of a CAFO, due to the observational challenges associated with measuring ammonia deposition. One of the few studies was conducted in Alberta, Canada (McGinn et al., 2016). In this study, they used the flux gradient method to directly measure ammonia deposition at one location downwind of a feedlot with 8600 head of cattle, with additional indirect measurements that quantified the uptake in soil patches at varying distances downwind. The study found ambient concentrations of 220-250 $\mu\text{g m}^{-3}$, and corresponding deposition fluxes between 6 and 12 $\mu\text{g m}^{-2} \text{s}^{-1}$ at the flux gradient tower approximately 100 m from the CAFO boundary, depending on wind direction and other environmental conditions. However, the flux gradient technique only performs well under relatively constant conditions, and the McGinn et al., (2016) study was only able to quantify deposition under a subset of wind directions. They compare the flux gradient approach with soil uptakes, and estimates of based on deposition velocity calculations that do not account for any processes besides the atmospheric resistance, and find a rapid decrease in the deposition fluxes from 17 $\mu\text{g m}^{-2} \text{s}^{-1}$ (where the ammonia concentration was typically 500 - 1000 $\mu\text{g m}^{-3}$) to

less than $1 \mu\text{g m}^{-2} \text{s}^{-1}$ over 500 m. The surface adjacent to the CAFO in this study consisted of oilseed rape crop as well as winter wheat, which are both larger crops with more leaf area than grass, but smaller than mature maize. Despite the lower concentrations of ammonia, it is not surprising to find that the deposition at the fenceline is higher our estimates for grass. They also find the same qualitative result that we show, that the deposition flux changes dramatically (e.g., by an order of magnitude) over a relatively small (i.e., 500 m) downwind distance from the CAFO boundary.

Another study (Shen et al., 2016) measured atmospheric ammonia concentrations at various distances downwind from a large CAFO (~18,000 head of cattle) in Victoria, Australia, over an unmanaged grassland surface; in the first study, they used a bidirectional flux model (Massad et al., 2010) to estimate deposition. They found deposition rates of $2.4 \mu\text{g N m}^{-2} \text{s}^{-1}$, which is equivalent to $3 \mu\text{g NH}_3 \text{m}^{-2} \text{s}^{-1}$ at the CAFO fenceline, and decreases by over a factor of 10 in a 1000 m measurement area. Compared to the Canadian CAFO in McGinn et al. (2016), this Australian feedlot was larger, and ambient ammonia concentrations were measured to be $508 \mu\text{g m}^{-3}$ 50 m from the CAFO boundary, which decreased to $53 \mu\text{g m}^{-3}$ over the same spatial interval, with deposition rates decreasing with increasing distance. As we show in Figure 2.5b, the type of land surface can dramatically impact the deposition flux next to the CAFO, even with the same emission rate and environmental conditions. Compare to the Shen et al., (2016) reported deposition fluxes, our modelled results report similar fluxes over grass ($10 \mu\text{g m}^{-2} \text{s}^{-1}$ at the CAFO fenceline, $7 \mu\text{g m}^{-2} \text{s}^{-1}$ at 50 m), suggesting that for grass, the model is given results similar to the Australian experimental studies. The difference in deposition rate between our model estimate ($10 \mu\text{g m}^{-2} \text{s}^{-1}$) and the measurement from Shen et al., (2016) ($3 \mu\text{g m}^{-2} \text{s}^{-1}$) at the fenceline can be explained by the higher concentration (1500 vs. $500 \mu\text{g m}^{-3}$), as well as differences in the environmental

conditions (8 degrees C, 70% RH for our simulations vs. diurnally variable conditions averaged over a few months in Victoria, Australia) or wind profile and atmospheric stability.

Expanding our analysis to the other surface types, maize, as well as deciduous and coniferous trees absorb 5-6 times as much ammonia as compared to grass. Relative to grasses, maize typically has a higher ammonia emission potential, and therefore we expect the canopy compensation point to be higher for a given set of environmental conditions. Despite the higher emission potential, the maize canopy has much higher fence-line ammonia deposition fluxes (60 vs $10 \mu\text{g m}^{-2} \text{s}^{-1}$) as compared to grass, and the maize canopy recaptures substantially more ammonia than the grass (33% vs 10%). Therefore, within this modelling framework, the difference between maize and grass is due to the more favorable mass-transfer of a maize canopy as compared to grass, rather than a thermodynamic difference in ammonia solubility within the plant's apoplast. The taller maize canopy produces more TKE near the surface, decreasing near-surface stratification and allowing more air with more concentrated ammonia to mix into the plant canopy; simultaneously, the larger total area of leaves intercept a larger fraction of the Lagrangian particle trajectories, leading to increased depletion of ammonia. For the forest simulations, the thermodynamics are increasingly favorable for ammonia deposition relative to the maize canopy, as the selected values for Γ_s and Γ_g are smaller for the tree species as compared to maize (Table 2); it is important to note that these parameters are highly uncertain for forests. While the total LAI of a forest canopy is similar to that of a maize canopy, the total height and LAD are also different. The combined effect of these differences is that idealized forest canopies can recapture 30-60% more ammonia relative to maize canopy. The idealized coniferous and deciduous LAD profiles are different, with coniferous canopies having more LAD near the surface while the deciduous canopy has an LAD profile that peaks further from the ground, based on parameterizations outlined in Teske and

Thistle, (2004). The ammonia plume originates at the surface, and so within the first 100 m, the plume intercepts more leaves in the coniferous canopy where leaves are near the surface; the coniferous deposition flux was $160 \mu\text{g m}^{-2} \text{s}^{-1}$ at the CAFO fenceline, which is 3 times higher than the maize deposition rate at this distance. However, the dense LAD near the surface and the increased surface roughness cause a stronger updraft and more near-surface turbulence (Figure 2.2), and the ammonia concentration near the surface rapidly decreases, and hence the deposition rate rapidly decreases; by 200 m from the CAFO boundary, the deposition flux for the coniferous simulation is smaller than the flux in the maize canopy. However, because the initial deposition flux is so large, the coniferous simulation still recaptures more total ammonia than the maize simulation. The deciduous LAD profile is shaped differently, with a larger fraction of the LAD near the top of the plant canopy. The ammonia plume from the surface does not immediately intercept the leaves, so the initial deposition rate is slower, relative to the coniferous case. However, the updraft on the upwind boundary of the forest is weaker near the surface, and the TKE production primarily occurs further from the surface relative to the coniferous case, so more of the ammonia penetrates into the plant canopy, and the deciduous simulation maintains a fast deposition rate for more distance. This is analogous to the more porous plant canopy outlined in the Bealey et al., (2014) study; however, the longer plant canopy in our study is much longer and the deposition rate plateaus after a few hundred meters, which negates the need for a backstop. By the downwind boundary of the deciduous forest, the ammonia deposition flux has decreased to approximately $3 \mu\text{g m}^{-2} \text{s}^{-1}$, the same value as the maize and coniferous canopies. Consequently, the net ammonia recapture by the deciduous forest is higher than the coniferous or maize simulations. In all vegetation cases, the deposition rate is initially high, and rapidly decreases.

From the results and discussion above, it follows that while replacing bare soil or grassland next to CAFOs with production of maize or reforestation, as much as 50% of the total ammonia emissions can be recaptured. However, because the gradient in the deposition flux is so large, a substantial fraction of the ammonia recapture can be accomplished with a fraction of the 1500 m length that we use in these simulations. For example, 80% of the total deposition for each land surface occurs in the first 500 m (Figure 2.5), with more occurring for the coniferous canopy, and 50% occurs in the first 100 m. This is useful, as practical concerns may prevent the growth of a 1500 m thick forest, particularly in drier climates where precipitation may not be adequate to support a forest. However, if using irrigation to maintain a much smaller patch of forest is possible, then this could be a viable tactic for locally recapturing more ammonia. In the western US, land next to CAFOs is often used to grow maize, sorghum, or other crops that can be used to provide feed for the CAFO, so many of these landscapes may already be optimized for local ammonia recapture; however, this may also be important for fertilization practices. However, there are other complications. In the subsequent study from Shen et al., (2017), they analyzed the soil and plant nitrogen content and measured a gradient in available soil-N content, soil ammonium content, soil nitrate content, soil pH, and soil inorganic nitrogen; in addition to impacting the soil emission potential, these changes can impact the soil's ability to support plant life, or grow crops. Shen et al., (2017) also observed decreases in total plant cover, as well as increases in the relative coverage of herbaceous plants to grasses, closer to the CAFO fence line, suggesting that the massive ammonia input (on the order of $220 \text{ kg N ha}^{-1} \text{ yr}^{-1}$) is impacting the soil chemistry and ecosystem health near the feedlot. Massad et al., (2010) derive several parameterizations for soil ammonia emission potential depending on the management practices and land-surface characteristics. If we

treat the land next to a CAFO as a managed surface of grass or crops, then the emission potential can be modeled as follows:

$$\Gamma_s = 66.4 + 0.853N_{in}^{1.59} \quad (2.8)$$

where Γ_s is the stomatal emission potential and N_{in} is the total nitrogen input in $\text{kg ha}^{-1} \text{ yr}^{-1}$. For an unmanaged environment, such as grassland or forest, the parameterization is as follows:

$$\Gamma_s = 246 + 0.0041N_{in}^{3.56} \quad (2.9)$$

Shen et al., (2016) and McGinn et al., (2016) observed deposition rates as high as of $3 \mu\text{g m}^{-2} \text{ s}^{-1}$ and $12 \mu\text{g m}^{-2} \text{ s}^{-1}$, respectively, which are equivalent to 950 and $3780 \text{ kg ha}^{-1} \text{ yr}^{-1}$, respectively. Shen et al., (2017) subsequently estimate that the average deposition is on the order of $220 \text{ kg ha}^{-1} \text{ yr}^{-1}$, which is more consistent with ammonia deposition estimates from other large-scale animal feedlots (Fowler et al., 1998; Loubet et al., 2009; Walker et al., 2019). Based on these three estimates of the total N input, we calculate stomatal emission potentials of 46360 , 416130 , and 4590 for the fluxes estimate in McGinn et al., (2016), Shen et al., (2016) and (2017) respectively, when modeling the landscape as a managed area. When modeling the land as an unmanaged ecosystem, we estimate emission potentials of 1.6×10^8 , 2.2×10^{10} , and 8.6×10^5 respectively. According to our simulations, the ammonia recapture potential, and therefore the deposition rate, are correspondingly higher for maize and forested surfaces. Based on the maximum deposition flux of $60 \mu\text{g m}^{-2} \text{ s}^{-1}$ for maize, we estimate that Γ_s is 5.3×10^6 or 6.8×10^{12} for managed or unmanaged ecosystems, respectively.

These Γ_s values have been calculated by extrapolating the deposition rate to an entire year. In reality, variation in winds, as well as changes in seasonal LAI will impact these deposition flux estimates. However, even if we divide these fluxes by 100, these estimates of Γ_s are much higher than any measured emission potentials for maize (Massad et al., 2010). The Massad et al., (2010)

parameterizations are based on measurements in less extreme conditions, and are not calibrated with this magnitude of ammonia deposition in mind. As Γ_s increases in response to ecosystem N-inputs, this will decrease the depositional flux, which is a negative feedback on the capacity of a plant canopy to absorb ammonia emerges. Therefore, these are certainly overestimates of the actual ecosystem values for Γ_s ; furthermore, it is also likely that estimates of ammonia deposition near CAFOs that rely on these bidirectional flux models, with commonly used parameters for Γ_s , strongly overestimate the deposition rate; therefore, there is a need to measure Γ_s next to large point sources to understand how plant and soil nitrogen respond to these massive deposition fluxes.

The compensation point, χ_c , is a function of T, RH, and the emission potential Γ_s . While T and RH measurements are commonly available, Γ_s , which is defined as the ratio of ammonium ion to hydrogen ion inside the leaf apoplast, requires offline laboratory characterization; due to the time-consuming and expensive nature of these measurements, large datasets of Γ_s are not commonly available in the literature. We tested the sensitivity of the modeling results to changes in Γ_s in order to constrain the effect that surface saturation may have on ammonia deposition. We chose to conduct the sensitivity analysis over maize for several reasons: (1) maize is an important agro-industrial crop and there are datasets available for Γ_s for maize to constrain the parameter, and (2) the maize canopy offers viable ammonia recapture potential in the base-case scenarios, and (3) maize and sorghum crops are quite commonly grown next to CAFOs already.

In Figure 2.6, we show the ammonia deposition fluxes and net fractional recapture for 4 different values of Γ_s for maize under two sets of T and RH conditions: the “base-case” conditions used throughout the manuscript (T = 8 degrees C, RH = 75%), and “hot-dry” conditions (T = 26 degrees C, RH = 30%). Under base-case scenarios, the two extreme values for Γ_s do not produce a clear difference in the deposition flux; this implies that it would be difficult to decouple changes

in Γ_s based on measurements of ammonia deposition alone. When integrated over 1500 m, there is a 3% difference in the total ammonia recapture, suggesting that the net ammonia recapture is not strongly sensitive to this parameter. However, simulations under the “hot-dry” environmental conditions show very different results. The total ammonia recapture changes by less than 5% for the simulation using Γ_1 (control) under hot and dry atmospheric conditions; however, using Γ_8 (highest) substantially decreases the deposition flux a short distance from the feedlot boundary relative to the Γ_1 simulation, and within 600 m of the CAFO boundary, the canopy compensation point exceeds the atmospheric concentration. This implies that the maize becomes a source of ammonia to the environment, rather than a sink. Integrated over the entire 1500 m maize canopy, the net ammonia recapture is less than 5%, which is $\frac{1}{6}$ the recapture from assuming Γ_1 . While Γ_8 is substantially larger than Γ_1 (33200 and 1300, respectively), it is substantially smaller than the results predicted by the parameterizations in Massad et al., (2010). Therefore, the actual effectiveness of maize, or any other plant canopy, for absorbing ammonia is likely lower than the estimates we provide based on these modelling results. The maximum deposition rate occurring at the domain boundary is not significantly smaller for the Γ_8 , suggesting that rapid deposition can occur with a high value for Γ , but only when the atmospheric loading is extremely high. McGinn et al., (2016) observed analogous behavior as well; at times when the flux gradient tower was upwind of the CAFO, the land became a source of ammonia to the atmosphere, suggesting that the land surface was indeed approaching saturation, and re-emitting ammonia back to the atmosphere when the surface compensation point exceeds the atmospheric concentration. Likely, during a typical diurnal cycle, the surface may change from being a sink of ammonia overnight, to a source during the day. However, we do not model other diurnal behavior inside the canopy.

Next, we generalize this result to a broader range of environmental conditions. We demonstrate in Figure 2.7 that generally under cold conditions, the effect of Γ on the canopy fractional ammonia recapture is small, and the effect of RH is negligible. Under hot conditions, Γ can dramatically impact the net ammonia recapture, as discussed above, but we predict that RH variability only has a small effect. RH affects the leaf area wetting, which enhances the cuticular leaf loss, which is not treated as a bidirectional flux in this model. However, the physical parameterization for this loss mechanism is poorly constrained, due to challenges isolating its effect from stomatal losses. Likewise, the physical parameters used are generic and advances to this specific loss mechanism are required to characterize the uncertainty or increase the precision of this modelling approach. Given the best-guess parameter values (Massad et al., 2010), this loss appears to be minor relative to the stomatal losses, due to the small effect that RH has on the net deposition.

Based on the discussion above, deposition into plant canopies is more sensitive to the emission potential in hot and dry climates, as both impact the canopy compensation point. It follows that land surfaces adjacent to CAFOs, where Γ is likely elevated due to long-term input of reactive nitrogen, are more likely to saturate due to increases in Γ in hotter and drier climates. However, warmer climates may also experience more rapid plant growth and faster microbial activity in the soil, which could result in more-rapid nitrification, utilization of N_R in biomass, or emission of N_2O and NO_x . For a given region, plant canopies will absorb more ammonia during the cooler periods when χ_C is suppressed, and will likely experience supersaturation during hotter and dryer periods. These processes may occur on a seasonal or diurnal timescale. However, there are other important limitations to the model that may impact the applicability of this result to the real world. In MODDAS, the leaf temperature is fixed as 0.1 degree C cooler than the atmospheric

temperature. However, in a dense plant canopy that is not under drought stress, the temperature may be substantially cooler and the RH may be substantially higher than the environment due to latent cooling from evapotranspiration. Therefore, if the atmospheric conditions are 26 °C and 30% RH, a well-irrigated field of maize will be cooler and more humid, and this will impact the compensation point behavior. Additionally, for the scenario of plants under drought stress, the stomatal resistance increases as plants close their stomata to limit evaporative loss to the environment. For scenarios where Γ is high, this will decrease the canopy compensation point and decouple it from temperature; conversely, for scenarios where Γ is low, the canopy compensation point increases under drought stress, as the stomata are no longer available to absorb ammonia from the atmosphere. The soil fluxes are also bidirectional and modeled using emission potential/compensation point behavior, but the underlying physics governing the resistances and solubility of ammonia in the soil pores is more complex. While we use a soil emission potential in this model, we do not vary it with changes in the stomatal emission potential in our sensitivity analysis. In reality, these two parameters are not likely to be completely independent.

Until this point, we have analyzed output from simulations that assume a neutral atmospheric profile with a typical atmospheric U and TKE profile at the model inlet. However, the atmospheric state can have dramatic effects on dispersion throughout the atmospheric boundary layer. K-epsilon models are cannot simulate non-neutral conditions in the atmosphere, so it is difficult to apply this modelling framework to a stable or unstable atmospheric state. We instead use Monin-Obukhov Theory (MOT)-derived profiles to produce wind and turbulence estimates for above the canopy, which are affected by the roughness length of the land surface; inside the plant canopies, as well as at the interface between atmospheric sections at canopy boundaries, there is a momentum balance to produce physically reasonable behavior; while this

representation of the atmosphere in the model can be used to model dispersion under different stability conditions, it does not accurately simulate dispersion inside the plant canopy, or across the interface between model regions with different surface properties. Therefore, we only use it to provide order-of-magnitude estimates of the sensitivity to dispersion. Consequently, we used a simpler and smaller model domain (Configuration 2), so these results cannot be compared to the Configuration 1 simulation results discussed above.

The sensitivity to stability is summarized in Table 3.3, which shows that under highly unstable conditions, 0.4% of the total ammonia is deposited to the maize surface and other base assumptions, which is 10% relative to the neutral Monin-Obukhov dispersion simulation, and 5% relative to the K-epsilon simulation (also neutral). Likewise, highly stable conditions increase deposition by 100% relative to the corresponding neutral case. The MOT simulations span roughly a factor of 20 between the most stable and most unstable case in terms of ammonia deposition, which the K-epsilon control simulation produced estimates that are more similar to stability class E (moderately stable) conditions, rather than the type D. This could be due to the K-epsilon theory having a more-realistic representation of dispersion in and immediately above the plant canopy, as well as more realistic behavior at the CAFO-maize model boundary, than the MOT cases. However, there may be other explanations for this difference. Regardless, the MOT simulations show that our predicted results are likely strongly a function of atmospheric stability, and that the approximate range in ammonia recapture fraction is a factor of 20.

Atmospheric stability is an instantaneous property of the atmosphere that varies with the accompanying weather and time of day; however, it often follows longer-term climate and seasonal patterns which depend on the region in question. In the western US, summers are dominated by low fractions of cloud cover and a strong solar flux during the day, which often

produces an unstable atmospheric profile, as well as efficient radiative cooling overnight which can produce a stable boundary layer. Conversely, the UK has more-frequent cloud cover and hence is dominated by neutral or near-neutral atmospheric profiles, with little diurnal difference. Equally important are differences in the land surface with season; an agricultural land may have bare soil or grass during half of the year, with crops growing from small to large before being harvested. Likewise, unmanaged grassland follows the life cycle of grasses throughout the year, and deciduous forests lose their leaves during the winter. The land surface therefore varies seasonally in terms of its capacity to mitigate ammonia emissions from a neighboring CAFO. Quantifying how the differences by region and season could impact ammonia deposition are an important next step for this field of study, but it is beyond the scope of the work presented here.

2.4.3 MODDAS Simulations; Use of Shelterbelts to Increase Ammonia Recapture

We have established that reforestation or growing crops such as maize adjacent to CAFOs can increase local ammonia recapture. However, converting 1500 m of grassland to managed forest is not always feasible if the land is currently used for other purposes. In fact, land next to CAFOs is often already used to grow feed for the residents of the feedlot, so changing land-use to a forest may not be economical for the feedlot operators. Therefore, we also investigated techniques to recapture more ammonia using minimal changes to the surrounding land surface by use of shelterbelts, or 10 m thick bands of trees, in different spatial arrangements. In Figure 2.8, we show the difference in atmospheric ammonia concentrations between the “upwindtrees” simulation and no trees in the model domain (Figure 2.8a), the surface concentrations for all of the shelterbelt scenarios considered (Figure 2.8b), as well as the fractional ammonia recapture (Figure 2.8c). The effect of trees placed upwind of the CAFO on the turbulence is to slow the surface windspeed, but increase turbulent kinetic energy. While slower winds can increase the residence time of the plume

in the downwind plant canopy, which may increase deposition, increased turbulence will enhance vertical mixing. Therefore, upwind trees cause a larger fraction of the plume to flow over the top of the crop field avoiding deposition. This is seen in Figure 2.8a, where the presence of trees upwind of the source create a difference in ammonia dispersion. The ammonia surface concentration is lower in the case with upwind trees as compared to the control simulation with no trees (Figure 2.8b), and the fractional ammonia recapture is approximately 25% lower than the control case (Figure 2.8c).

The downwind tree case has a similar effect on the turbulence over the maize, but the winds and turbulence over the CAFO are affected differently; there is a buildup of ammonia concentrations on the downwind half of the CAFO, upwind of the first shelterbelt. The surface concentration decreases rapidly, due to increases in boundary layer turbulence, but also rapid deposition inside the coniferous shelterbelt. The “downwindtrees” case has the fastest initial ammonia deposition (Figure 2.8c). However, the rate of deposition slows as the surface concentration rapidly decreases, and by the end of the maize field, the increase in surface turbulence offsets the initial fast deposition, and this simulation offers no improvement over the control case. Finally, the “alltrees” case combines both properties, increased turbulence and decreased windspeeds over the CAFO as well as fast initial deposition as the plume passes through the first downwind coniferous band. The “alltrees” case is only able to recapture 80% of the total ammonia, relative to the case with no trees.

In all of the shelterbelt cases, the 10 m thick coniferous bands of trees are not large enough to absorb an appreciable fraction of the ammonia emissions; the tree bands are porous and most of the ammonia passes through them. However, these narrow bands of trees can have a relatively large impact on the turbulence near the surface, and this effect appears to dominate for tree bands

of this size. The increase in surface turbulent kinetic energy promotes faster mixing of the ammonia away from the surface, which ultimately decreases the net ammonia recapture. When positioned upwind, the shelterbelts are not able to absorb any ammonia from the atmosphere, so there is no mechanism to increase the ammonia recapture. When positioned downwind, the shelterbelts do rapidly absorb ammonia from the atmosphere, but 10 m is not enough to absorb an appreciable fraction of the total emissions from a large CAFO. While Bealey et al., (2014) found that relatively smaller plant canopies (length 30-50 m) can still absorb as much as 20% of the total ammonia emitted from some animal feedlot systems, the authors found that the optimal configuration was to use a tree with a deciduous-type LAD profile for the majority of the plant canopy to allow the ammonia plume to penetrate the plant canopy, but then to use a dense coniferous “backstop” section at the end of the plant canopy to prevent ammonia from pass through the plant canopy. However, the systems that were investigated in this study involved much smaller sources, so the absolute size of the deposition flux was much smaller. As they were primarily interested in emissions from poultry operations, the most-effective canopy configurations that they explored allowed the animals were allowed to range inside of a plant canopy. Due to the correspondingly larger size of the CAFOs in our study, and difficulty of maintaining a cattle pasture under a dense tree canopy, we did not test these specific strategies. For a larger CAFO, a greater fraction of the emissions will mix above the downwind plant canopy, and the importance of this vertical mixing. However, based on the fast initial deposition flux in various tree types for the from the first land-use experiment (Figure 2.5), there is likely a shelterbelt design that is closer to 100 m in length that removes an appreciable fraction of the total ammonia emissions. However, we have not developed an optimized design of this shelterbelt in this work.

As mentioned in the previous settings, there are many different variables that we do not explicitly account for in this work. For example, in the context of an extremely narrow (i.e., 10 m thick) shelterbelt, the issue of sink-saturation becomes more important, as there is a correspondingly smaller amount of plant mass available to absorb ammonia. Additionally, the capacity of the shelterbelt to absorb ammonia from the atmosphere would vary depending on the leaves present on the shelterbelt vegetation, and the sink would be less effective if the trees shed their leaves during the winter, or under drought stress. Furthermore, for this application, there are other concerns about the wind direction. For narrow shelterbelts, small changes in wind direction will result in very different turbulent behavior upwind and downwind of the source; our results show that the ammonia recapture fraction is very sensitive to the impact the shelterbelts have on turbulent dispersion near the surface. In this study, we showed that shelterbelt systems perform better with trees downwind of the source. However, changing wind direction would make it impossible to design a shelterbelt that is always downwind of the source. Likewise, for conditions where the mean flow produces a yaw angle, the turbulent response could be more complicated, and is not accounted for in this study. Truly optimizing shelterbelts for ammonia recapture likely requires three-dimensional simulations, and a robust seasonal analysis, both of which are beyond the current capabilities of the modelling system we use in this study.

5. Conclusions

In this work, we used OpenFOAM-MODDAS to perform coupled dispersion and bidirectional flux modelling for ammonia emitted from large CAFOs. First, we tested the ammonia deposition over 5 broad land-use types: bare soil, grass, maize crop, coniferous forest, and deciduous forest. Over bare soil, the deposition rate is slow, due to the unfavorable compensation

point as well as the lack of near-surface turbulence to allow mixing. Over grass, we find a maximum depositional flux of $10 \mu\text{g m}^{-2} \text{ s}^{-1}$, which agrees with reported measurements for ammonia deposition at CAFO fence lines over grass, though there are few measurement studies to compare with. For this configuration, the grass simulations re-absorb approximately 8% of the total CAFO emissions. However, rougher surfaces with higher LAI such as maize, coniferous trees, and deciduous trees produce more favorable near-surface turbulence and have more capacity to absorb ammonia from the atmosphere. Our simulations of a maize crop suggest that 30% of the total CAFO emissions could be recaptured in this scenario, while simulations of coniferous and deciduous forest led to 40% and 50% of total ammonia recapture respectively, though we know of no measurement studies to test these modelling results. Because the canopy compensation point is a function of environmental variables (T and RH) and the ammonia emission potential, which is often poorly constrained, there is considerable uncertainty in these estimates, though the uncertainty depends on the environment. Under cold and humid conditions, the total ammonia recapture is not sensitive to the emission potential, but under hot and dry conditions, the total ammonia recapture is highly sensitive to the emission potential in the plant canopy. The emission potential is in turn, a function of the total nitrogen input to the ecosystem, suggesting that measurements of this parameter near CAFOs are essential in order to better-constrain the bidirectional flux processes in this extreme environment. Finally, we investigate the use of smaller-scale shelterbelts to engineer favorable conditions for ammonia recapture with minimal land-use changes. However, the results of our analysis suggest that the turbulent environment produced by shelterbelts are often unfavorable for increasing ammonia recapture, due to the increases in near-surface turbulent kinetic energy.

REFERENCES

- Asman, W. a. H., Sutton, M.A., Schjørring, J.K., 1998. Ammonia: emission, atmospheric transport and deposition. *New Phytologist* 139, 27–48. <https://doi.org/10.1046/j.1469-8137.1998.00180.x>
- Baum, K.A., Ham, J.M., Brunzell, N.A., Coyne, P.I., 2008. Surface boundary layer of cattle feedlots: Implications for air emissions measurement. *Agricultural and Forest Meteorology* 148, 1882–1893. <https://doi.org/10.1016/j.agrformet.2008.06.017>
- Bealey, W.J., Loubet, B., Braban, C.F., Famulari, D., Theobald, M.R., Reis, S., Reay, D.S., Sutton, M.A., 2014. Modelling agro-forestry scenarios for ammonia abatement in the landscape. *Environ. Res. Lett.* 9, 125001. <https://doi.org/10.1088/1748-9326/9/12/125001>
- Boucher, O., Randall, D.A., Artaxo, P., Bretherton, C., Feingold, G., Forster, P., Kerminen, V.-M., Kondo, Y., Liao, H., Lohmann, U., Rasch, P., Satheesh, S.K., Sherwood, S., Stevens, B., Zhang, X.-Y., n.d. Clouds and Aerosols, in: *Climate Change 2013: The Physical Science Basis. Contribution of Working Group I to the Fifth Assessment Report of the Intergovernmental Panel on Climate Change*. Cambridge University Press, Cambridge, United Kingdom and New York, NY USA.
- Clark, C.M., Phelan, J., Doraiswamy, P., Buckley, J., Cajka, J.C., Dennis, R.L., Lynch, J., Nolte, C.G., Spero, T.L., 2018. Atmospheric deposition and exceedances of critical loads from 1800–2025 for the conterminous United States. *Ecological Applications* 28, 978–1002. <https://doi.org/10.1002/eap.1703>
- Colorado Cattlemen’s Association [WWW Document], n.d. URL <https://www.coloradocattle.org/> (accessed 11.5.19).

- Dennis, R.L., Schwede, D.B., Bash, J.O., Pleim, J.E., Walker, J.T., Foley, K.M., 2013. Sensitivity of continental United States atmospheric budgets of oxidized and reduced nitrogen to dry deposition parametrizations. *Philosophical Transactions of the Royal Society B: Biological Sciences* 368, 20130124. <https://doi.org/10.1098/rstb.2013.0124>
- Dockery, D.W., Pope, C.A., Xu, X., Spengler, J.D., Ware, J.H., Fay, M.E., Ferris, B.G.Jr., Speizer, F.E., 1993. An Association between Air Pollution and Mortality in Six U.S. Cities. *New England Journal of Medicine* 329, 1753–1759. <https://doi.org/10.1056/NEJM199312093292401>
- Ellis, R.A., Murphy, J.G., Pattey, E., Haarlem, R. van, O'Brien, J.M., Herndon, S.C., 2010. Characterizing a Quantum Cascade Tunable Infrared Laser Differential Absorption Spectrometer (QC-TILDAS) for measurements of atmospheric ammonia. *Atmospheric Measurement Techniques* 3, 397–406. <https://doi.org/10.5194/amt-3-397-2010>
- Flechard, C.R., Massad, R.-S., Loubet, B., Personne, E., Simpson, D., Bash, J.O., Cooter, E.J., Nemitz, E., Sutton, M.A., 2015. Advances in Understanding, Models and Parameterizations of Biosphere-Atmosphere Ammonia Exchange, in: Massad, Raia-Silva, Loubet, Benjamin (Eds.), *Review and Integration of Biosphere-Atmosphere Modelling of Reactive Trace Gases and Volatile Aerosols*. Springer Netherlands, Dordrecht, pp. 11–84. https://doi.org/10.1007/978-94-017-7285-3_2
- Flesch, T.K., Wilson, J.D., Harper, L.A., Todd, R.W., Cole, N.A., 2007. Determining ammonia emissions from a cattle feedlot with an inverse dispersion technique. *Agricultural and Forest Meteorology* 144, 139–155. <https://doi.org/10.1016/j.agrformet.2007.02.006>
- Fowler, D., Pitcairn, C.E.R., Sutton, M.A., Flechard, C., Loubet, B., Coyle, M., Munro, R.C., 1998. The mass budget of atmospheric ammonia in woodland within 1 km of livestock

- buildings. *Environmental Pollution, Nitrogen, the Confer-N-s First International Nitrogen Conference 1998* 102, 343–348. [https://doi.org/10.1016/S0269-7491\(98\)80053-5](https://doi.org/10.1016/S0269-7491(98)80053-5)
- Hacker, J.M., Chen, D., Bai, M., Ewenz, C., Junkermann, W., Lieff, W., McManus, B., Neininger, B., Sun, J., Coates, T., Denmead, T., Flesch, T., McGinn, S., Hill, J., 2016. Using airborne technology to quantify and apportion emissions of CH₄ and NH₃ from feedlots. *Anim. Prod. Sci.* 56, 190–203. <https://doi.org/10.1071/AN15513>
- Hanjalic, K., 2005. Will RANS Survive LES? A View of Perspectives. *J. Fluids Eng* 127, 831–839. <https://doi.org/10.1115/1.2037084>
- Hargreaves, D.M., Wright, N.G., 2007. On the use of the k- ϵ model in commercial CFD software to model the neutral atmospheric boundary layer. *Journal of Wind Engineering and Industrial Aerodynamics* 95, 355–369. <https://doi.org/10.1016/j.jweia.2006.08.002>
- Hristov, A.N., Hanigan, M., Cole, A., Todd, R., McAllister, T.A., Ndegwa, P.M., Rotz, A., 2011. Review: Ammonia emissions from dairy farms and beef feedlots. *Canadian Journal of Animal Science* 91, 1–35. <https://doi.org/10.1139/CJAS10034>
- Intergovernmental Panel on Climate Change (Ed.), 2014. Anthropogenic and Natural Radiative Forcing, in: *Climate Change 2013 - The Physical Science Basis*. Cambridge University Press, Cambridge, pp. 659–740. <https://doi.org/10.1017/CBO9781107415324.018>
- Irwin, J.S., 1979. A theoretical variation of the wind profile power-law exponent as a function of surface roughness and stability. *Atmospheric Environment* (1967) 13, 191–194. [https://doi.org/10.1016/0004-6981\(79\)90260-9](https://doi.org/10.1016/0004-6981(79)90260-9)
- Jarosz, N., Loubet, B., Durand, B., McCartney, A., Foueillassar, X., Huber, L., 2003. Field measurements of airborne concentration and deposition rate of maize pollen. *Agricultural and Forest Meteorology* 119, 37–51. [https://doi.org/10.1016/S0168-1923\(03\)00118-7](https://doi.org/10.1016/S0168-1923(03)00118-7)

- Jarosz, N., Loubet, B., Huber, L., 2004. Modelling airborne concentration and deposition rate of maize pollen. *Atmospheric Environment* 38, 5555–5566.
<https://doi.org/10.1016/j.atmosenv.2004.06.027>
- Launder, B.E., Spalding, D.B., 1983. PAPER 8 - THE NUMERICAL COMPUTATION OF TURBULENT FLOWS, in: Patankar, S.V., Pollard, A., Singhal, A.K., Vanka, S.P. (Eds.), *Numerical Prediction of Flow, Heat Transfer, Turbulence and Combustion*. Pergamon, pp. 96–116. <https://doi.org/10.1016/B978-0-08-030937-8.50016-7>
- Laville, P., Lehuger, S., Loubet, B., Chaumartin, F., Cellier, P., 2011. Effect of management, climate and soil conditions on N₂O and NO emissions from an arable crop rotation using high temporal resolution measurements. *Agricultural and Forest Meteorology* 151, 228–240. <https://doi.org/10.1016/j.agrformet.2010.10.008>
- Li, Y., Schichtel, B.A., Walker, J.T., Schwede, D.B., Chen, X., Lehmann, C.M.B., Puchalski, M.A., Gay, D.A., Collett, J.L., 2016. Increasing importance of deposition of reduced nitrogen in the United States. *PNAS* 113, 5874–5879.
<https://doi.org/10.1073/pnas.1525736113>
- Li, Y., Thompson, T.M., Van Damme, M., Chen, X., Benedict, K.B., Shao, Y., Day, D., Boris, A., Sullivan, A.P., Ham, J., Whitburn, S., Clarisse, L., Coheur, P.-F., Collett Jr., J.L., 2017. Temporal and spatial variability of ammonia in urban and agricultural regions of northern Colorado, United States. *Atmos. Chem. Phys.* 17, 6197–6213.
<https://doi.org/10.5194/acp-17-6197-2017>
- Loubet, B., Asman, W.A.H., Theobald, M.R., Hertel, O., Tang, Y.S., Robin, P., Hassouna, M., Dämmgen, U., Genermont, S., Cellier, P., Sutton, M.A., 2009. Ammonia Deposition Near Hot Spots: Processes, Models and Monitoring Methods, in: Sutton, M.A., Reis, S.,

- Baker, S.M.H. (Eds.), Atmospheric Ammonia: Detecting Emission Changes and Environmental Impacts. Springer Netherlands, Dordrecht, pp. 205–267.
https://doi.org/10.1007/978-1-4020-9121-6_15
- Loubet, B., Cellier, P., Générumont, S., Laville, P., Flura, D., 2003. Measurement of short-range dispersion and deposition of ammonia over a maize canopy. *Agricultural and Forest Meteorology* 114, 175–196. [https://doi.org/10.1016/S0168-1923\(02\)00176-4](https://doi.org/10.1016/S0168-1923(02)00176-4)
- Loubet, B., Cellier, P., Milford, C., Sutton, M.A., 2006. A coupled dispersion and exchange model for short-range dry deposition of atmospheric ammonia. *Q.J.R. Meteorol. Soc.* 132, 1733–1763. <https://doi.org/10.1256/qj.05.73>
- Marceau, A., Saint-Jean, S., Loubet, B., Foueillassar, X., Huber, L., 2012. Biophysical characteristics of maize pollen: Variability during emission and consequences on cross-pollination risks. *Field Crops Research* 127, 51–63.
<https://doi.org/10.1016/j.fcr.2011.11.006>
- Massad, R.-S., Nemitz, E., Sutton, M.A., 2010. Review and parameterisation of bi-directional ammonia exchange between vegetation and the atmosphere. *Atmos. Chem. Phys.* 10, 10359–10386. <https://doi.org/10.5194/acp-10-10359-2010>
- McGinn, S.M., Flesch, T.K., Crenna, B.P., Beauchemin, K.A., Coates, T., 2007. Quantifying Ammonia Emissions from a Cattle Feedlot using a Dispersion Model. *Journal of Environmental Quality* 36, 1585–1590. <https://doi.org/10.2134/jeq2007.0167>
- McGinn, S.M., Janzen, H.H., Coates, T.W., Beauchemin, K.A., Flesch, T.K., 2016. Ammonia Emission from a Beef Cattle Feedlot and Its Local Dry Deposition and Re-Emission. *Journal of Environmental Quality* 45, 1178–1185.
<https://doi.org/10.2134/jeq2016.01.0009>

- Miller, D.J., Sun, K., Tao, L., Pan, D., Zondlo, M.A., Nowak, J.B., Liu, Z., Diskin, G., Sachse, G., Beyersdorf, A., Ferrare, R., Scarino, A.J., 2015. Ammonia and methane dairy emission plumes in the San Joaquin Valley of California from individual feedlot to regional scales. *Journal of Geophysical Research: Atmospheres* 120, 9718–9738.
<https://doi.org/10.1002/2015JD023241>
- Mosier, A.R., Duxbury, J.M., Freney, J.R., Heinemeyer, O., Minami, K., 1998. Assessing and Mitigating N₂O Emissions from Agricultural Soils. *Climatic Change* 40, 7–38.
<https://doi.org/10.1023/A:1005386614431>
- Pollack, I.B., Lindaas, J., Roscioli, J.R., Agnese, M., Permar, W., Hu, L., Fischer, E.V., 2019. Evaluation of ambient ammonia measurements from a research aircraft using a closed-path QC-TILDAS operated with active continuous passivation. *Atmospheric Measurement Techniques* 12, 3717–3742. <https://doi.org/10.5194/amt-12-3717-2019>
- Richards, P.J., Hoxey, R.P., 1993. Appropriate boundary conditions for computational wind engineering models using the k- ϵ turbulence model, in: Murakami, S. (Ed.), *Computational Wind Engineering* 1. Elsevier, Oxford, pp. 145–153.
<https://doi.org/10.1016/B978-0-444-81688-7.50018-8>
- Segalini, A., Nakamura, T., Fukagata, K., 2016. A Linearized $k-\epsilon$ Model of Forest Canopies and Clearings. *Boundary-Layer Meteorol* 161, 439–460.
<https://doi.org/10.1007/s10546-016-0190-5>
- Seinfeld, J.H., Pandis, S.N., 2016. *Atmospheric Chemistry and Physics, From Air Pollution to Climate Change*, 3rd ed. Hoboken, NJ.

- Shen, J., Chen, D., Bai, M., Sun, J., Coates, T., Lam, S.K., Li, Y., 2016. Ammonia deposition in the neighbourhood of an intensive cattle feedlot in Victoria, Australia. *Scientific Reports* 6, srep32793. <https://doi.org/10.1038/srep32793>
- Shen, J., Chen, D., Bai, M., Sun, J., Lam, S.K., Mosier, A., Liu, X., Li, Y., 2018. Spatial variations in soil and plant nitrogen levels caused by ammonia deposition near a cattle feedlot. *Atmospheric Environment* 176, 120–127. <https://doi.org/10.1016/j.atmosenv.2017.12.022>
- Shonkwiler, K.B., Ham, J.M., 2018. Ammonia emissions from a beef feedlot: Comparison of inverse modeling techniques using long-path and point measurements of fence-line NH₃. *Agricultural and Forest Meteorology, Greenhouse gas and ammonia emissions from livestock production* 258, 29–42. <https://doi.org/10.1016/j.agrformet.2017.10.031>
- Staebler, R.M., McGinn, S.M., Crenna, B.P., Flesch, T.K., Hayden, K.L., Li, S.-M., 2009. Three-dimensional characterization of the ammonia plume from a beef cattle feedlot. *Atmospheric Environment* 43, 6091–6099. <https://doi.org/10.1016/j.atmosenv.2009.08.045>
- Stephen, K., Aneja, V.P., 2008. Trends in agricultural ammonia emissions and ammonium concentrations in precipitation over the Southeast and Midwest United States. *Atmospheric Environment, Agricultural Air Quality: State of the Science (AAQ-2006)* 42, 3238–3252. <https://doi.org/10.1016/j.atmosenv.2007.05.062>
- Sun, K., Tao, L., Miller, D.J., Khan, M.A., Zondlo, M.A., 2014. On-Road Ammonia Emissions Characterized by Mobile, Open-Path Measurements. *Environ. Sci. Technol.* 48, 3943–3950. <https://doi.org/10.1021/es4047704>

- Sun, K., Tao, L., Miller, D.J., Zondlo, M.A., Shonkwiler, K.B., Nash, C., Ham, J.M., 2015. Open-path eddy covariance measurements of ammonia fluxes from a beef cattle feedlot. *Agricultural and Forest Meteorology* 213, 193–202.
<https://doi.org/10.1016/j.agrformet.2015.06.007>
- Svensson, U., Häggkvist, K., 1990. A two-equation turbulence model for canopy flows. *Journal of Wind Engineering and Industrial Aerodynamics* 35, 201–211.
[https://doi.org/10.1016/0167-6105\(90\)90216-Y](https://doi.org/10.1016/0167-6105(90)90216-Y)
- Teske, M.E., Thistle, H.W., 2004. A library of forest canopy structure for use in interception modeling. *Forest Ecology and Management* 198, 341–350.
<https://doi.org/10.1016/j.foreco.2004.05.031>
- Van Damme, M., Clarisse, L., Whitburn, S., Hadji-Lazaro, J., Hurtmans, D., Clerbaux, C., Coheur, P.-F., 2018. Industrial and agricultural ammonia point sources exposed. *Nature* 564, 99. <https://doi.org/10.1038/s41586-018-0747-1>
- Vitousek, P.M., Menge, D.N.L., Reed, S.C., Cleveland, C.C., 2013. Biological nitrogen fixation: rates, patterns and ecological controls in terrestrial ecosystems. *Philosophical Transactions of the Royal Society B: Biological Sciences* 368, 20130119.
<https://doi.org/10.1098/rstb.2013.0119>
- Walker, J.T., Bell, M.D., Schwede, D., Cole, A., Beachley, G., Lear, G., Wu, Z., 2019. Aspects of uncertainty in total reactive nitrogen deposition estimates for North American critical load applications. *Science of The Total Environment* 690, 1005–1018.
<https://doi.org/10.1016/j.scitotenv.2019.06.337>

- Werner, C., Butterbach-Bahl, K., Haas, E., Hickler, T., Kiese, R., 2007. A global inventory of N₂O emissions from tropical rainforest soils using a detailed biogeochemical model. *Global Biogeochemical Cycles* 21. <https://doi.org/10.1029/2006GB002909>
- Whitehead, J.D., Twigg, M., Famulari, D., Nemitz, E., Sutton, M.A., Gallagher, M.W., Fowler, D., 2008. Evaluation of Laser Absorption Spectroscopic Techniques for Eddy Covariance Flux Measurements of Ammonia. *Environ. Sci. Technol.* 42, 2041–2046. <https://doi.org/10.1021/es071596u>
- Wu, Z., Schwede, D.B., Vet, R., Walker, J.T., Shaw, M., Staebler, R., Zhang, L., 2018. Evaluation and Intercomparison of Five North American Dry Deposition Algorithms at a Mixed Forest Site. *Journal of Advances in Modeling Earth Systems* 10, 1571–1586. <https://doi.org/10.1029/2017MS001231>
- Wu, Z., Wang, X., Turnipseed, A.A., Chen, F., Zhang, L., Guenther, A.B., Karl, T., Huey, L.G., Niyogi, D., Xia, B., Alapaty, K., 2012. Evaluation and improvements of two community models in simulating dry deposition velocities for peroxyacetyl nitrate (PAN) over a coniferous forest. *Journal of Geophysical Research: Atmospheres* 117. <https://doi.org/10.1029/2011JD016751>

CHAPTER 3. METHODS OF ESTIMATING DEPOSITION USING ATMOSPHERIC CONCENTRATION MEASUREMENTS: A CASE STUDY OF AMMONIA DOWNWIND OF A FEEDLOT

Atmospheric ammonia is an important compound in the atmosphere because of its role in aerosol formation and its importance to the global nitrogen cycle. However, because ammonia is challenging to measure with sufficient time resolution for eddy-covariance-type deposition flux approaches, other strategies are needed to measure its dry deposition in a cost-effective way. Livestock feeding operations are a major source of ammonia emissions to the atmosphere, and ammonia concentrations near these large feedlots can be many orders of magnitude higher than background. The impact that these feedlots can have on regional ecology and air quality can be difficult to quantify, in large part due to the challenges of measuring and modelling ammonia dry deposition adjacent to these major sources. Feedlots housing ruminant livestock such as cattle are also sources of methane. Because methane does not undergo appreciable dry deposition and is chemically inert on relevant spatial scales, we can use it as a tracer to constrain the downwind dilution of feedlot ammonia emissions.

The ratio of atmospheric ammonia to methane has been shown to decrease with increasing distance downwind of a feedlot due to deposition and aerosol partitioning of gas-phase ammonia. In atmospheric conditions where inorganic aerosol formation is slow, methane can serve as a conservative tracer, allowing the estimation of the fraction of ammonia that undergoes deposition downwind of the feedlot. Using atmospheric modelling of turbulent dispersion in the atmospheric boundary layer, we produce synthetic measurements to demonstrate a novel approach for estimating the deposition. We use Large Eddy Simulation (LES) to simulate the dispersion of tracer species from an area source to represent ammonia and methane emissions from a feedlot.

We then use the background-corrected ammonia:methane concentration ratio to construct a mass balance, and calculate the dry deposition flux. We then sample the LES output to produce synthetic observations in order to test this approach for use in the field with two candidate measurement platforms: sensors deployed on a small unmanned aerial vehicle and on a surface-based mobile observation platform such as an automobile. We find that for the automobile (ground based) deployment, our method produces overestimates of ammonia deposition on the order of a factor of 1.5 due to sampling near the surface where ammonia concentrations are depleted. However, use of the aerial platform allows more accurate estimation of the deposition fraction (relative error < 0.09).

This work is currently under review in *Agriculture and Forest Meteorology*.

3.1 Introduction

Nitrogen is an essential chemical element in life on earth. However, because N_2 gas is mostly inert, it must be fixed into Biologically Available Nitrogen (BAN) species, either oxidized or reduced nitrogen species (e.g., nitrate and ammonia, respectively), for it to be incorporated into biomass. Human activity has surpassed soil and ocean bacteria as the dominant source of nitrogen fixation on Earth, in large part due to the synthesis of ammonia via the Haber-Bosch process; hundreds of Tg of BAN are produced every year for use in plant fertilizers (Vitousek et al., 2013). Excess application of fertilizer to crops can enter rivers and streams through surface runoff, leach into groundwater, or volatilize to impact the surrounding ecosystems and atmosphere. Additionally, the inclusion of crude protein in animal feed can increase the concentration of ammonia in animal waste as a byproduct of metabolism, and ammonia can similarly impact the air and groundwater from animal livestock (Asem-Hiablíe et al., 2019; Hristov et al., 2011; Rotz et al., 2019). Once in

the atmosphere, ammonia is the most common alkali species and often combines with atmospheric acids to form aerosols, which can impact the earth's radiative balance (Boucher et al., 2013), is hazardous to human health (Dockery et al., 1993), and contributes to visibility degradation (Gu et al., 2014). Fugitive BAN in the atmosphere can also undergo wet and dry deposition into sensitive ecosystems, where it can cause soil acidification (via soil microbe nitrification), eutrophication, and changes to biodiversity and soil microbiomes (McLaughlin and Mineau, 1995).

Under non-precipitating conditions, atmospheric ammonia can stick to surfaces and is taken up by plants and soils for incorporation into biomolecules as part of the terrestrial nitrogen cycle. Therefore, the ammonia in the atmosphere is often treated as a dry depositing species in atmospheric chemical transport models (Farquhar et al., 1980). However, plants and soils can also emit ammonia to the atmosphere as a byproduct of biochemical processes that depend on the temperature, soil/leaf moisture, relative humidity, plant species, and nitrogen status. Taken together, these variables determine the surface "compensation point", which is analogous to the concentration of ammonia represented by the surface. When the compensation point is larger than the atmospheric concentration, the surface is a source of ammonia, whereas when the compensation point is smaller than the ambient concentration, then the surface is a sink. When the surface compensation point and atmospheric concentration are similar, the direction of the net flux can change on short timescales due to changes in environmental conditions impacting the surface compensation point. Furthermore, the mass-transfer between the surface and atmosphere is a function of wind speed, atmospheric stability, and surface roughness, which can vary on micrometeorological scales. In most cases, the compensation point and atmospheric concentrations are of similar magnitude, so the ammonia-surface interactions are best represented as a "bidirectional flux process" (Sutton et al., 1995). However, close to major sources of ammonia,

the atmospheric concentrations in the plume are much larger than the surface compensation point (Shen et al., 2016), and the net flux can be approximated as a unidirectional dry deposition process (McGinn et al., 2007); we refer to this as “nearfield dry deposition”. The approximate size of this “nearfield” area (where the flux is universally from the atmosphere to the surface) and the magnitude of the deposition fluxes in this zone is highly uncertain. This process is further complicated by ammonia solubility in rain and snow, where it can undergo wet deposition; however, dry deposition is typically the dominant ammonia sink in the nearfield, so we focus only on the fair-weather dry-deposition processes in this study.

Concentrated Animal Feeding Operations (CAFOs), which can house tens of thousands of livestock, are major sources of ammonia and other air pollutants (e.g., methane) to the surrounding environment (Eilerman et al., 2016; Shonkwiler and Ham, 2018; Yang et al., 2016). For example, CAFOs in the Colorado Front Range impact nearby vulnerable alpine ecosystems farther to the west such as Rocky Mountain National Park (RMNP). In RMNP, increases in ammonia and ammonium deposition are observed (Beem et al., 2010; Benedict et al., 2013) during periods of transport from Northeast Colorado, a region with extensive CAFO development that is visible from space (Damme et al., 2018). However, direct numerical simulation and source-apportionment type analyses are challenging due to difficulties representing the complicated transport in this region in chemical transport models (Thompson et al., 2015). More broadly, while increased regulation of U.S. NO_x emissions has helped to significantly reduce nitrate deposition nationally, much of the U.S. has seen increases in ammonium deposition (Li et al., 2016), and the reactive nitrogen deposition budget now appears to be dominated by wet and dry inputs of ammonia/ammonium in most regions. Nationally, 60% of all US ammonia emissions are estimated to come from animal feeding operations (US EPA, 2016). CAFOs also are a major source of ammonia in regions in

Australia (Hacker et al., 2016; Shen et al., 2018, 2016) and Canada (McGinn et al., 2016, 2007; Staebler et al., 2009). In order to determine the precise role CAFO emissions play in ecosystem changes from nitrogen deposition and in air quality, we need to be able to accurately represent the nearfield ammonia deposition in order to avoid systematic biases and reduce uncertainties in our emissions estimates in chemical transport models.

One reason deposition of ammonia is uncertain is the difficulty of directly measuring ammonia fluxes. Ammonia is a “sticky” gas that can bind to instrument inlets and surfaces, which can compromise measurement time response and in some cases introduce memory and hysteresis effects. It is difficult to measure ammonia accurately enough at a high temporal resolution for conventional flux measurement techniques, such as eddy covariance (Roscioli et al., 2016; Sun et al., 2015). Other methods, such as the aerodynamic gradient method (Flechard and Fowler, 1998; Loubet et al., 2012), cannot be performed in the vicinity of major sources, as the assumption of stationarity and constant flux over a measurement time-period is often not valid with rapidly changing wind directions (Loubet et al., 2009). Finally, the rapid changes to wind direction under turbulent conditions and the large concentration gradients present near a major source with variable emission fluxes (Sun et al., 2015) such as a CAFO can cause rapid changes to the atmospheric concentration, and therefore the deposition rate, on short timescales, which further complicates this measurement. Therefore, ammonia surface fluxes must generally be quantified using less direct approaches. Because CAFO emissions of ammonia are large and dry deposition can occur rapidly, large in-plume spatial gradients in ammonia concentrations often arise. Many studies have used these gradients alongside other measurements to estimate the deposition rate. One study (McGinn et al., 2016) used soil traps alongside passive gas-phase ammonia samplers configured to employ the Flux Gradient method downwind of a CAFO in Alberta, Canada to measure the

deposition of ammonia. Another study (Shen et al., 2016) used downwind passive measurements of atmospheric ammonia with a bidirectional flux model to calculate the deposition rate, and in a follow-up study (Shen et al., 2018), they use soil and leaf nitrogen analysis to corroborate their estimates of deposition. Both studies show that on average, ammonia deposition occurs rapidly near a CAFO, with 90% of all measured ammonia dry deposition (within the study domain) occurring within 3 km of the CAFO, but these studies required challenging laboratory characterization of soil ammonia and many passive atmospheric ammonia measurements, which limits this approach to assessment of time-averaged nearfield dry deposition. This time averaging is a limitation as ammonia dry deposition varies under specific meteorological conditions and specific times of day, so there is a need to be able to quantify deposition under shorter time (sub-daily) periods.

Time-resolved ammonia-concentration measurements by multiple stationary monitors at different distances from the CAFO have the potential to fill this need for sub-daily deposition estimates. However, deployment of many sensors in a single study may be impractical. Furthermore, it can be beneficial to use a single analyser to prevent systematic measurement biases between separate analyzers from introducing artifacts in this approach. Consequently, we know of no studies that have tried to use this approach to quantify deposition. Alternatively, a single mobile measurement platform could be used to make measurements at multiple locations in a relative short time period (minutes to hours). Surface vehicle (e.g., car or truck-based) mobile measurements (Miller et al., 2015; Shadman, 2018; Sun et al., 2014; Tao et al., 2015), and aircraft-based measurements (Hacker et al., 2016; Staebler et al., 2009) have been used to measure emissions of ammonia and other species (e.g., methane) from CAFOs, but few studies have attempted to quantify the ammonia deposition. Another study (Hacker et al., 2016) that also used

aircraft-based measurements of ammonia demonstrated the use of methane co-emission from a CAFO to trace the dispersion of these two species downwind, and to estimate the emission flux for both species. They measured elevated ammonia concentrations above background 7 km downwind of the CAFO and elevated methane 25 km downwind; however, they did not use this difference to estimate the deposition rate of ammonia. One notable study (Staebler et al., 2009) used a small, manned aircraft to measure ammonia emissions from the same CAFO as McGinn et al (2016). They used a dispersion model and simultaneous measurements of aerosol composition to show that the chemical transformation of gas-phase ammonia to particulate NH_4^+ is negligible on these temporal and spatial scales; they showed less dry deposition than McGinn, finding that only 10% of the total ammonia underwent deposition near the CAFO. While manned aircraft can be very effective at studying emissions and fluxes from area sources, this approach may be prohibitively expensive. Therefore, it is difficult to conduct measurements under diverse enough meteorological conditions and with enough replicates to confidently characterize the deposition. We are not aware of any studies that have used a mobile laboratory or surface vehicle to specifically study ammonia deposition adjacent to feedlot-type sources, or any studies using a small Unmanned Aerial System (sUAS) a.k.a. drone to make any ammonia measurements near a CAFO.

Miller et al., (2015) demonstrated that the ratio of ammonia to methane in the atmosphere decreases rapidly downwind of beef feedlots, and attribute this decrease to a combination of deposition and aerosol partitioning. Their study location, the San Joaquin Valley, has a number of sources of nitrate, and ammonium nitrate formation is an important sink for ammonia in this region. Furthermore, their study period (winter) corresponds to lower temperatures and higher relative humidity, further favouring rapid aerosol partitioning. Other studies (e.g., Staebler et al., 2009)

have demonstrated that in warm conditions with low atmospheric sulfate and nitrate, ammonia partitioning into the aerosol phase is negligible within a few km of a CAFO. Here, we propose a new approach for using the change in ammonia:methane ratio to quantify the fraction of ammonia that undergoes dry deposition near a CAFO.. In Section 3.3.2, we explain the methods used to implement this approach using dispersion modelling. In Section 3.3.1, we briefly discuss the dispersion modelling results. In Section 3.3.2, we show that we are able to estimate the deposited ammonia within a given distance from the CAFO by controlling for the dispersion and dilution downwind of the source by conservation of methane mass. This approach requires very reasonable assumptions that ammonia loss due to uptake into particles or oxidation are small in this high ammonia concentration environment. In Section 3.3.3, we investigate the feasibility of implementing this approach in a real measurement situation by sampling the LES simulated turbulent methane and ammonia concentration fields as they would be measured from mobile platforms (i.e., automobile or sUAS), and applying our analysis technique to the pseudo-data to estimate the deposited fraction of ammonia. Finally, we subject the analysis to a sensitivity test to provide guidance for optimizing the sampling procedure in a more realistic measurement scenario.

3.2 Methods

3.2.1 LES SAM Simulations

We use a Large Eddy Simulation (LES) to simulate dispersion and deposition in a turbulent boundary layer. LES is a solution to low-pass filtered Navier-Stokes Equations, and it explicitly resolves turbulence down to the level of the model resolution while relying on parameterizations for sub-grid-scale turbulence. The LES model used in this study is the System for Atmospheric Modelling (SAM) v6.10.10 (Khairoutdinov and Randall, 2002). SAM is a community convection-

resolving LES model that uses a K-theory (1st order closure) scheme for sub-grid-scale turbulent advection. SAM has been used for a range of applications including studies of convective processes (Khairoutdinov and Randall, 2003), coupling between surface and the atmospheric boundary layer (Gentine et al., 2016, 2014), and atmospheric dispersion (Berner et al., 2015; Stevens et al., 2012). Specifically, studies have used SAM to model aerosol microphysics and dilution from power plant smokestacks (Gong et al., 2013; Stevens et al., 2012), as well as the biomass burning plumes (Lonsdale et al., 2019; Sakamoto et al., 2016), where the dispersion and in-plume processing have been evaluated against measurements. SAM includes support for tracers with user-defined physics; the simulations in this study were performed with two tracers: one was entirely passive and meant to represent methane, while the other tracer representing ammonia underwent a 1st-order removal at the model surface, approximating unidirectional dry deposition close to a CAFO. We assume no other loss mechanisms (e.g., particle formation) for ammonia in the plume. The deposition flux, F ($\text{kg m}^{-2} \text{s}^{-1}$), is given by:

$$F = -v_d C(x, y, z = 0) \quad (3.1)$$

where v_d (m s^{-1}) is the surface deposition velocity (providing a rate constant for removal by deposition in grid cells located adjacent to the model surface boundary), and C is atmospheric concentration of the depositing species (e.g., kg m^{-3}). We employ a Cartesian spatial grid where z is elevation ($z=0$ at ground level), x is aligned with the wind direction, and y is the transverse direction. We conducted SAM simulations on a $128 \times 96 \times 106$ (x , y , and z , respectively) grid with 100×100 m horizontal (x, y) resolution with variable vertical (z) resolution ranging from 5 m near the surface and increasing gradually to 60 m outside at $z=1000$ m. The SAM simulation domain therefore spans 12.8 km in the downwind dimension, 9.6 km in the cross-wind dimension, and 5.26 km above the surface. The model boundary conditions (wind speed, relative humidity, and

surface sensible and latent heat flux) were prescribed using NCEP North American Regional Reanalysis (NARR) interpolated to our simulation location in Fort Collins, Colorado (*NCEP Reanalysis data provided by the NOAA/OAR/ESRL PSD, Boulder, Colorado, USA, from their Web site at <https://www.esrl.noaa.gov/psd/>*). We chose June 25th-27th of 2014 to represent typical summer conditions for this region. The daytime temperature and relative humidity were between 290 and 300K (17 and 27 degrees C) and 15-40%, respectively. Surface winds were between 4 and 8 m s⁻¹. At night, the atmosphere is more stable and large eddies tend to be absent, and all tracer transport is sub-grid-scale. For this reason, we only consider transport during the daytime in this study. Typical wind-speed values are in the range of 4-8 m/s near the surface during this period. We include results of a sensitivity study where we repeat this analysis for a different atmospheric state Appendix B2.

To represent the CAFO in SAM, we use a single area source of 600 x 600 meters located over the interval $X = 500-1100$ m and $y=4500-5100$ meters (and $z=0$). This is approximately equivalent to a small-to-medium-sized CAFO that has a capacity of 18,000 head of cattle. By considering only a single source, we are assuming that the feedlot is far from any other sources of either methane or ammonia. In real world CAFOs, the methane and ammonia emissions are a result from different biologic processes on the CAFO site (enteric fermentation vs volatilization from urea decomposition in animal manure and urine); therefore the actual emission sources are not exactly co-located, vary differently with time, and have different degrees of homo/heterogeneity on the CAFO facility. While we recognize that these processes have been studied at great detail (provide references), we do not attempt to capture this complexity in this study. The synthetic measurements we produce (described in Section 3.2.2) use concentration measurements over a range of 0 to 3500 m downwind of the source. In our model simulations, the sources for methane and ammonia are

co-located and homogeneously distributed throughout the area source, and emission fluxes were assumed to be 45 and 90 $\mu\text{g m}^{-2}$ of methane and ammonia, respectively (uniform over the source), based on measurements made at a small CAFO in northern Colorado (Shonkwiler and Ham, 2018; Sun et al., 2015). For all simulations discussed here, the ammonia deposition velocity model parameter was set to 1.0 cm s^{-1} (0.01 m s^{-1}) which is an order-of-magnitude approximation of this parameter, based on literature estimates of the ammonia dry depositional fluxes from field studies (Schrader and Brümmer, 2014). In the SAM simulations, the background value for both tracers is zero; hence, all concentrations presented in this paper are implicitly background corrected, and should be considered excess concentrations above a real-world background concentration. While the real atmosphere does contain substantial background concentrations of methane, we are assuming that said background can be accurately and precisely determined to differentiate from in-plume measurements, and background-correct the observations. Consequently, we can not consider the impact of variable background concentrations or contaminating sources in this study. Throughout the rest of the manuscript, we refer to all concentration as excess (i.e., “excess ammonia concentration”).

To determine the simulated “reference” ammonia deposition in our model (i.e. the “true” ammonia dry deposition calculated from the 3-D model output), we use the model output surface tracer concentration fields and the deposition velocity parameter to calculate the surface flux using Equation 1. Knowing the local deposition flux at any x-y location on the ground (averaged over the entire time period) allows determination of the overall deposition rate for any x-y region by integrating over that region – we are particularly interested in examining regions extending to different downwind distances X beyond the edge of the feedlot. By normalizing the deposition rate

for the region by the overall source emission rate of ammonia, we determine the simulated fraction of emitted ammonia that is deposited in the region.

In a real-life field experiment, e.g., with the automobile or sUAS, it will never be possible to have full x-y-z data over the entire domain. Therefore, the primary objective of this study is to develop a technique to determine the fraction of ammonia emissions from a CAFO that undergoes dry deposition nearby, by inverting synthetic measurements of ammonia and methane atmospheric concentrations, but without relying on direct flux measurement techniques. To do this, we compare the ratio of ammonia to methane in the atmosphere at the CAFO boundary (i.e., $X = 1000$) to a different distances (i.e., 1-3.5km, or $X = 2000$ to 3500) downwind from the source. The concentrations of both species decrease further from the source due to dilution. Additionally, if we integrate the total mass in each Y-Z plane through our model domain, we expect the total planar mass loading to decrease for both species; as the plume mixes vertically, it is more rapidly diluted by stronger winds at higher altitudes. However, we expect the total mass conductance through each downwind Y-Z plane to be conserved if emissions and winds are constant. We next introduce the domain-integrated mass conductance, J , given by:

$$J = \iint U(x, y, z)C(x, y, z)dydz \quad (3.2)$$

where U is the x component of the wind and C is the concentration. In the absence of net convergence or divergence, the domain-integrated mass-conductance is a conserved quantity for non-depositing species. Therefore, because ammonia undergoes dry deposition, the ratio of J_{NH_3}/J_{CH_4} decreases with distance from the source. Therefore, the relative change in this ratio will tell us the fraction of ammonia that has been removed from the domain.

3.2.2 Sampling Strategies

We next investigate the accuracy of using field measurements of atmospheric methane and ammonia concentrations to estimate ammonia deposition by sampling our 4-dimensional SAM output to produce synthetic data. We consider two different sampling strategies: a single mobile surface measurement (i.e., sensors mounted on an automobile or truck), and a single mobile

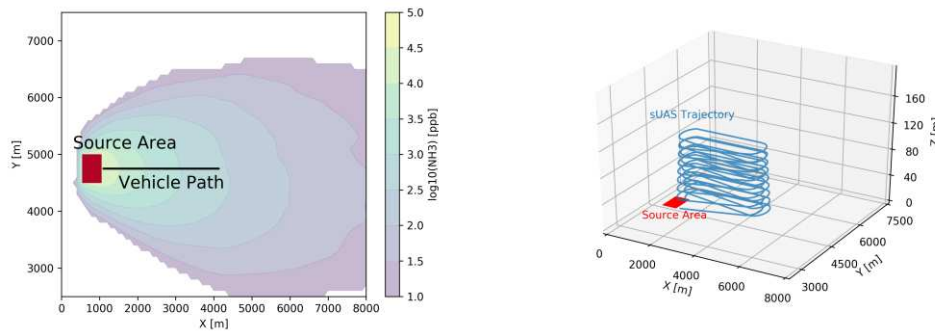


Figure 3.1: (a) Surface vehicle measurement platform base trajectory outlined over an example plume and (b) sUAS base trajectory, subject to FAA constraints, flight payload considerations, and fuel conservation strategies. Both trajectories were perturbed to examine the sensitivity of the results to deviations from these “best-case scenario” trajectories as described in the text.

airborne platform (i.e., sensors mounted on a sUAS). The vehicle and sUAS base-case trajectories are plotted in Figure 3.1a and 3.1b, respectively. For our base-case surface-vehicle scenario, we sampled the SAM output on the downwind side of the source area, down the plume centerline ($Y=4800$ m) from the CAFO boundary ($X=1100$ m) driving away from the CAFO at 12 m s^{-1} , continuing to a maximum distance of 3 km from the CAFO (i.e., $X=4100$ m), then turning around and retracing this trajectory back to the CAFO. The base-case measurement scenario sampled 2 hours of SAM output, so 12 total transects are completed. Concentrations are measured 5 m off the ground (simulating the instrument inlets on a mast). We built the base-case sUAS trajectory based on a number of real-world considerations. In this study we assume a fixed-wing sUAS because they can often carry higher mass payloads than rotor type sUASs (as needed for ppb sensitivity methane and ammonia sensors) and avoid some of the flowfield complexity associated

with the strong down wash of rotor sUAS. We also assume the sUAS cannot safely fly under 10 m from the surface and cannot exceed 400ft (~120m) given current regulations of the United States Federal Aviation Administration (FAA). The flight trajectory is selected to minimize ascents, descents, and strong turns and has a 45 minute flight time. Furthermore, to mimic our surface-based sampling approaches, we designed our flight trajectory to travel upwind and downwind from the CAFO in a series of 12 ovals extending 3500 m downwind of the CAFO. For both measurement platforms, these base-case scenarios closely mimic the domain-integrated calculation and produce the most accurate estimates of deposition within the framework of this study. However, we acknowledge that other better-performing trajectories may exist.

For the methane and ammonia sensing we assume a temporal response of 5 s as can be achieved with laser based instruments. All pseudo-measurements with (background-corrected) concentrations less than 15 ppb are masked (remove from the simulated data) to simulate a lower limit of detection due to both instrumental (sensor) limitations as well as due to the variations in the ambient backgrounds over the relatively large spatial and temporal scales of the simulated measurement experiments (i.e., if either tracer species was observed to have a lower concentration than 15 ppb, we threw out both observations). This assumption is equivalent to assuming that the background concentrations can be determined as a function of time to sufficient precision such that the in-plume concentrations can be differentiated from out-of-plume background concentrations at a precision of 15 ppb such that we are able to background-correct the observed concentrations. Background ammonia concentrations are typically smaller than 15 ppb whereas concentrations adjacent to CAFOS greatly exceed this value, so this masked value is a reasonable value for ammonia (Benedict et al., 2018). Methane background concentrations are several orders of magnitude higher than this, and in regions with nearby sources of methane the background

variability can be in this range ((Arefev et al., 2016). However, the background variability on daily and hourly timescales is generally less than 15 ppb and can be accurately characterized with upwind measurements. Furthermore, for large sources such as CAFOs, the difference between in-plume and out-of-plume methane concentrations is usually larger than 15 ppb. Finally, the results presented here are not very sensitive to this assumed lower limit of detection (15 ppb) (e.g., if we change the mask to 5 or 50 ppb, our deposition estimate decreases by 1% and increases 10%, respectively) However, we do not explicitly account for background variability in this study, and we acknowledge that this may be a source of error for implementing this method in regions with other large sources of methane and ammonia nearby. We therefore acknowledge the complexities of this assumption, but believe that it is adequately justified.

To perform the deposition analysis, we bin the simulated observations from each platform by downwind distance from the source; we then calculate each bin's average concentration for both ammonia and methane, and calculate the ratio between the two bin-average concentrations. We then normalize the concentration ratios by the furthest upwind ratio that was observed (i.e., the ratio in the observation bin closest to the CAFO), and assert that these normalized ratios at given X positions represent the fraction of ammonia that has been deposited over the given spatial interval (i.e., unity minus the fraction then corresponds to the amount still to be transported yet further downwind). The results presented below will show the posited linkage between these spatially varying ammonia:methane ratios and the ammonia deposition fraction. Following that, to characterize the robustness of the sampling approaches, we examine other sampling trajectories by perturbing the mobile sampling strategies (surface vehicle and sUAS) from the base-case by changing the following: sampling duration, sampling time-of-day within our simulated atmosphere, angle offset from the plume centerline, translation in x, y, and (where applicable) z direction. We

use the results of these trajectory perturbations to test the robustness of the results against realistic deviations from a single sampling trajectory that may arise from practical limitations in a real measurement scenario, such as the placement of roads or private property. We acknowledge that we are not estimating uncertainties across the full range of atmospheric and emission conditions (which would require more LES simulations), and our uncertainties represent those for the specific conditions during the times and location of our LES simulation.

3.3 Results and Discussion

3.3.1 LES SAM Simulation Results

First, we show results from our SAM LES simulations. Figure 3.2 shows, from left to right, instantaneous (background-corrected) methane concentration fields for an arbitrary point in time, 2-hour averaged methane concentrations, and the ammonia-to-methane ratio for the 2-hour average concentrations. The two-hour time period was from 10 to 12 local standard time. The top row shows the x-z plane at the y centerline, and the bottom row shows x-y plane at the model surface layer. The individual timesteps shown in Figures 3.2a and 3.2d are representative of the turbulent structure of the dispersion system represented by this model. Averaging enough model output together produces smooth plume structures (Figures 3.2b and 3.2c). Also, the ratio plots (Figures 3.2c and 3.2f) show that the ammonia is depleted from the model domain near the surface with less depletion occurring far from the surface.

In the instantaneous output (Figures 3.2a and d), we see that the concentrations of methane vary spatially in a chaotic manner. This is a property of turbulent flow. We show this figure to emphasize that any measurements of tracer concentrations in a plume will vary considerably as a function of time. However, with suitable temporal averaging, a smoother and better-defined plume

structure emerges, as shown in Figures 3.2b,e. This smoother concentration profile is what ultimately governs the depositional fluxes over the sampling period of interest. A measurement study that attempts to quantify deposition will measure the atmosphere as it appears in Figures

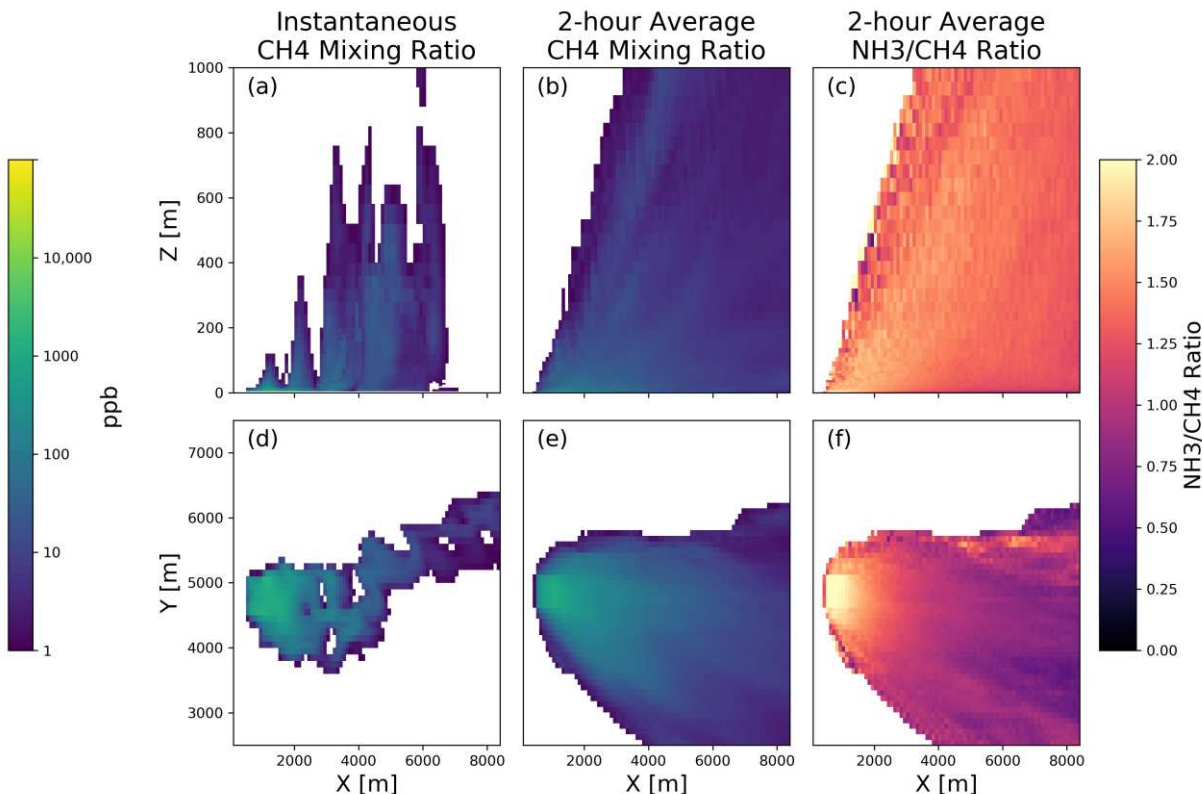


Figure 3.2: The instantaneous and steady-state plume behavior from SAM simulation output. The top row shows domain centerline concentrations (x vs z) with (a) showing excess methane concentration model output from a single timestep, (b) showing a 2-hour average from 10-12, and (c) shows the ammonia/ methane excess concentration ratios. The bottom row (d, e, and f, respectively) shows the same model output, but in the surface layer of the model domain ($z = 2.5$ m in the center of the box). Excess concentrations smaller than 1 ppb are masked.

3.2a,d, but to infer the behaviour demonstrated in Figures 3.2d,e. Finally, we show that the ratio of ammonia to methane changes very little outside of the layer immediately above the surface (Figure 3.2c). Near the surface, there is a substantial decrease in this ratio downwind. In order to quantify the fraction of CAFO emissions that deposit nearby, it is important to quantify the change in ratio throughout a representative fraction of the emissions plume extent in the vertical direction.

In order to determine whether these SAM dispersion results are consistent with representative atmospheric conditions, we compare the SAM simulation output to measurements. We compare the wind characteristics to measurements from a CoAgMet site in northern Colorado near the simulation location, and we compare the ammonia concentrations at the simulated CAFO boundary to some in situ measurements of ammonia at a CAFO fence line in eastern CO. We have included the model-measurement comparison and discussion in Appendix B1.

3.3.2 Estimation of the Fraction of Ammonia Removed Using All SAM Output

Figure 3.3a shows the total Y-Z-integrated ammonia and methane loadings (i.e., the total mass of methane and ammonia in a Y-Z slice through the domain) as a function of X. Figure 3.3b shows the Y-Z-integrated flux (i.e., the mass conductances) as a function of x for ammonia and methane as well as the total-domain-width x-integrated deposited ammonia (calculated via the reference method) and the deposition-corrected ammonia conductance (what our calculations expect the ammonia conductance to be in the absence of deposition). Figure 3.3c shows the estimated fraction of ammonia remaining in the column as a function of downwind distance using two methods: the change in methane and ammonia conductances, and the reference deposition. All results shown in Figure 3.3 are averaged from 10-12 Local Standard Time. We also looked at results from 12-14, 14-16, and 16-18, well as an average over the entire 8-hour period, and while the atmospheric state changed during each of these time periods, the overall qualitative results were not sensitive to the time of day.

In Figure 3.3a, the y-z-integrated atmospheric mass-loading of methane and ammonia are not constant; as the tracer species mix vertically, they are advected by systematically faster winds, causing a net increase in the rate that mass is exported from the domain and decreasing mass loadings further downwind from the source. However, in the absence of transport out of the top or

lateral domain boundaries, or any mass sources or sinks inside the model domain (i.e., deposition), we expect the mass conductance to be a conserved quantity, equal to the emission rate. In Figure

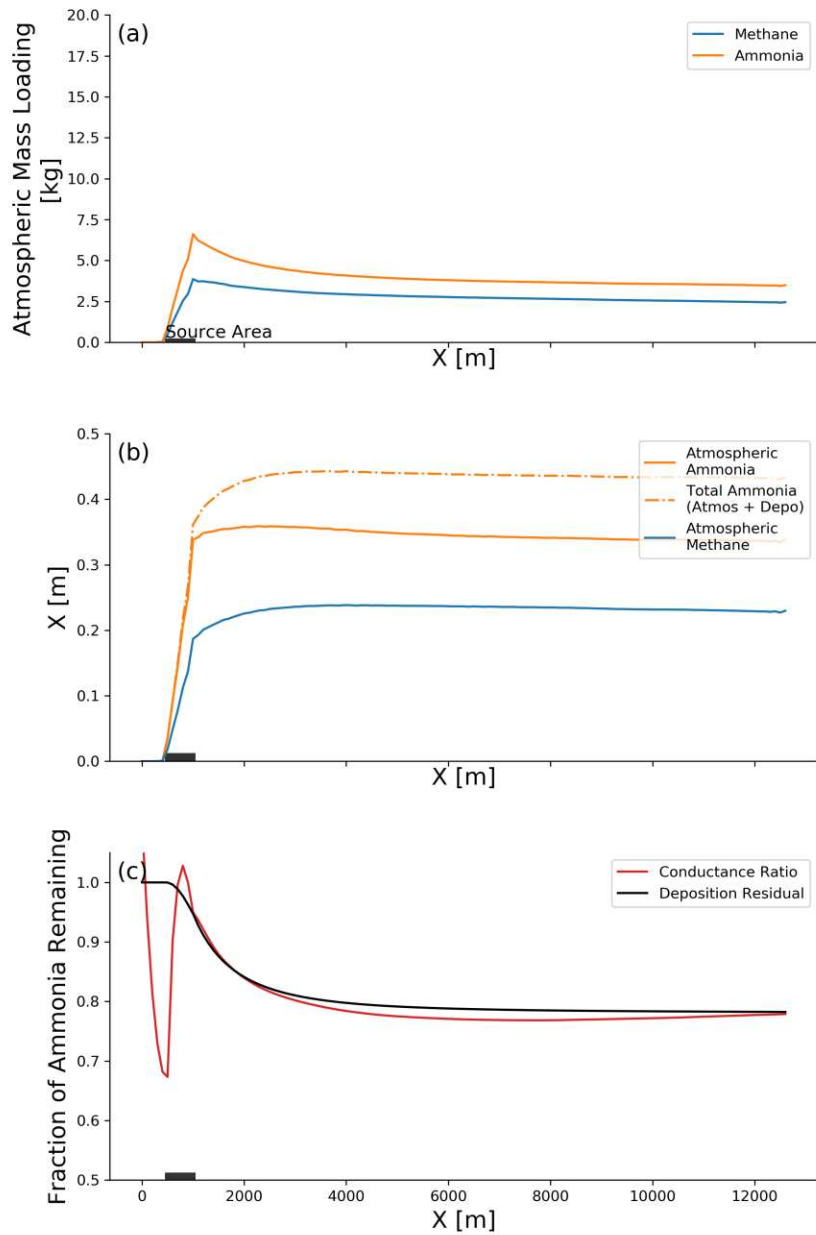


Figure 3.3: (a) the total Y-Z integrated ammonia and methane mass loading plotted as a function of x , (b) the atmospheric Y-Z mass conductance for ammonia and methane (solid lines), as well as integrated reference deposition flux (orange dashed line) and the deposition-corrected ammonia mass conductance (orange dot-dashed), and (c) the fraction of ammonia remaining calculated from the deposited mass (black) and from the ammonia/methane 3.3b, the methane conductance eventually converges to a steady-state value, but immediately

adjacent to the source area (gray shaded region), the conductance still slowly increases. We believe that this is an artifact from the LES simulation, due to the sub-grid-scale turbulence parameterization. Close to the source, large concentration gradients are present and most of the methane and ammonia mass is close to the surface where the wind speed is low, so sub-grid-scale transport dominates; further from the source, this effect becomes less important.

When considering the mass conductance integrated across the entire model domain, we construct a mass balance for ammonia through each y - z plane where ammonia is either advected through the plane or undergoes dry deposition. The advection flux of methane, which does not undergo deposition, is constant, and therefore the ratio of ammonia to methane must be directly proportional to the mass-loss of ammonia from the domain. In Figure 3.3c, we see that for these dispersion conditions, approximately 20% of the total ammonia undergoes dry deposition within the first 5km of the CAFO boundary, with fractionally very little ammonia deposition occurring in the next 6km. We also see that using the ratio of conductances agrees with the reference deposition fraction (calculated offline) to within 1%.

We have demonstrated that by integrating ammonia flux over the entire three-dimensional spatial domain, we can use the mass conductance ratio of ammonia to methane to determine the deposition rate of ammonia downwind of the CAFO. We now test how well we can determine ammonia deposition with more limited information, in particular with ammonia and methane concentrations along only the X - Z plane of the domain – for different X - Z planes extending to different heights Z . Here, we use the same basic approach as for the full domain, but we consider only values down the X - Z central plane of the domain (i.e., $Y = 4800$), and we truncate the Z -integral at various heights lower than the top of the model domain. This approach tests the calculation under scenarios where we cannot sample the entire atmosphere, but are limited in the

vertical and lateral extent of our measurements. The percent bias of the limited-domain estimate of the ammonia removal relative to the actual removal (from the reference deposition calculation,

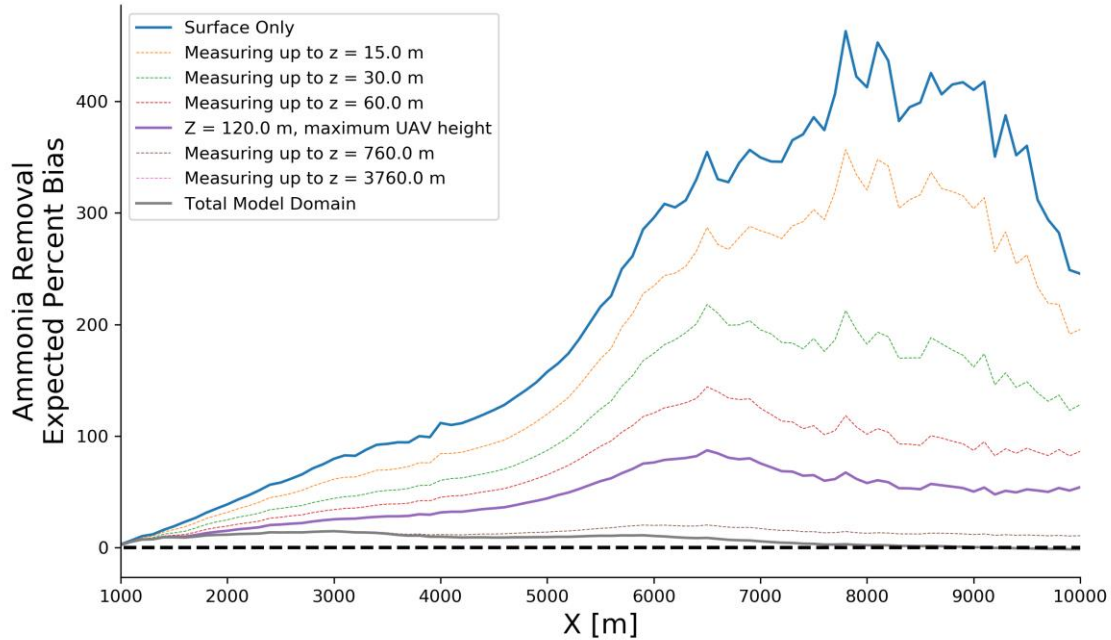


Figure 3.4: Percent bias of the fractional ammonia removal, comparing the centerline mass loading ratio (the novel method) and the offline actual deposited mass method (our reference method) plotted vs. the x coordinate in the model simulations, where $X = 1000\text{m}$ corresponds to the CAFO boundary. Each line corresponds to the inclusion of a different vertical depth in the model domain in the centerline ratio method with the solid blue line using only the surface concentrations, the purple line using 120m and below (i.e., the maximum allowed altitude for a small Unmanned Aerial System without FAA certification), and the gray line represents the entire model domain. Intermediate altitudes are represented as dashed lines. A bias of 0 denotes perfect agreement between the methods.

shown in the black curve in Figure 3.3c) is plotted in Figure 3.4. We show the expected bias for the following cases: using only the surface concentrations (solid blue line), all model output below 120 meters (solid purple line, the maximum allowed flying height assumed for the sUAS), and the result of using all model output to the domain top (gray line) with intermediate heights included in dashed lines.

From Figure 3.4, we see that by using only mass concentration ratios down the plume centerline instead of conductances from the total domain (gray curve), we introduce a small positive bias which is a result of the conductance artifact in Figure 3.3; this artifact is on the order of 5% at 9 km downwind of the source. However, by reducing the vertical extent of the vertical integral included in our ratio calculation, we introduce additional positive bias. In an extreme scenario, using only the surface concentrations produces a 100% bias in the expected deposition 4 km from the CAFO boundary because we are only sampling the surface where ammonia is more efficiently removed by deposition, rather than sampling the entire plume. However, surface-based measurements are the most common and easiest approach for atmospheric composition measurements next to sources such as CAFOs. This finding shows that by only considering the change in ammonia:methane ratio at the surface, estimates of ammonia deposition are inherently biased high. Conversely, a sUAS can be operated to a height of 120 m above the surface. Under this scenario, a sUAS-based measurement introduces ~40% positive bias for our simulated conditions, with vanishingly small biases as we approach the source, and sample the plume before it can vertically mix much higher than this upper limit. From Figure 3.4, we also show that the value added of flying higher than 120 m decreases rapidly, especially close to the source. We also see that for a given number of vertical levels, the bias for our deposition calculation under these dispersion conditions increases as a function of x for the first ~7 km past the CAFO as the tracer species continue to mix vertically, and our restricted sampling domain becomes less representative of the total column loading of the tracer species. At $x = 8000$ m, or 7 km downwind from the source boundary, the bias approaches a constant value. In the next section, we test the feasibility of using concentration ratios to estimate ammonia deposition using realistic measurements.

3.3.3 Using Vehicular and Aerial Platforms to Estimate the Fraction of Ammonia Removed

Next, we extend this general approach for quantifying ammonia deposition to simulated observations from the two potential measurement platforms: using either an automobile or a sUAS to measure atmospheric methane and ammonia concentrations. Figure 3.5 show the two time series of (implicitly background-corrected) synthetic observations of methane and ammonia atmospheric mixing ratios, from the simulated automobile and sUAS measurement platforms (Figure 3.5a and b, respectively). For both time series, values below 15 ppb were masked in order to simulate a limit-of-detection and to clearly differentiate in-plume from implicitly-corrected background

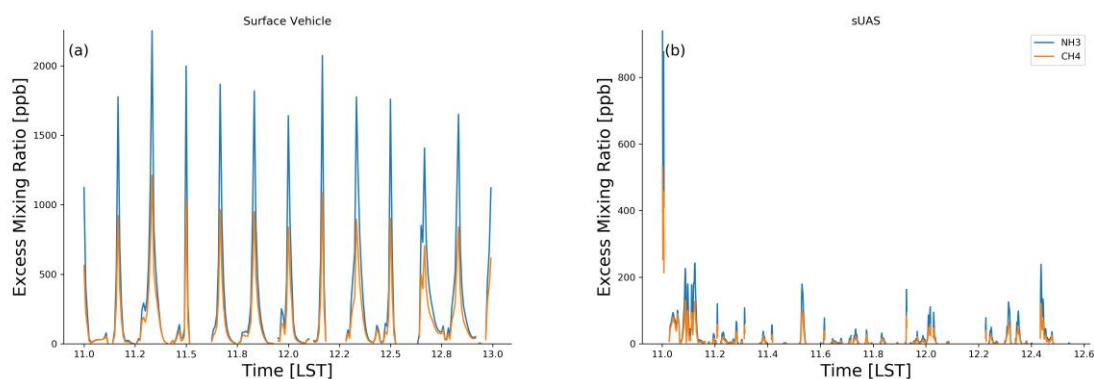


Figure 3.5: Observed ammonia and methane concentration timeseries in Local Standard Time (LST) (blue and orange, respectively) from the surface-vehicle-based platform (a) and the sUAS platform (b).

variability. On both platforms, the ammonia and methane concentrations are highly correlated ($R = 0.99$) which is expected, given that they have identical source areas and are both constantly emitted. Both time series show large variability in the observed concentrations which is driven by the measurement position relative to the source. The sUAS-based observations are more likely to experience masked observations (i.e., concentrations less than 15 ppb) because the sUAS covers a greater spatial area including elevated heights above the plume.

Figure 3.6a and 3.6b show observed ammonia/methane concentration ratios as a function of downwind position X for the two measurement platforms. In Figure 3.6a, each point represents

a single observation from the vehicle. We binned all observations by 300 m X intervals and calculate the mean ammonia and methane concentrations in each bin, then take the ratio of the two. Compared to the conductance ratios shown in Figure 3.3c, there is considerable scatter for the

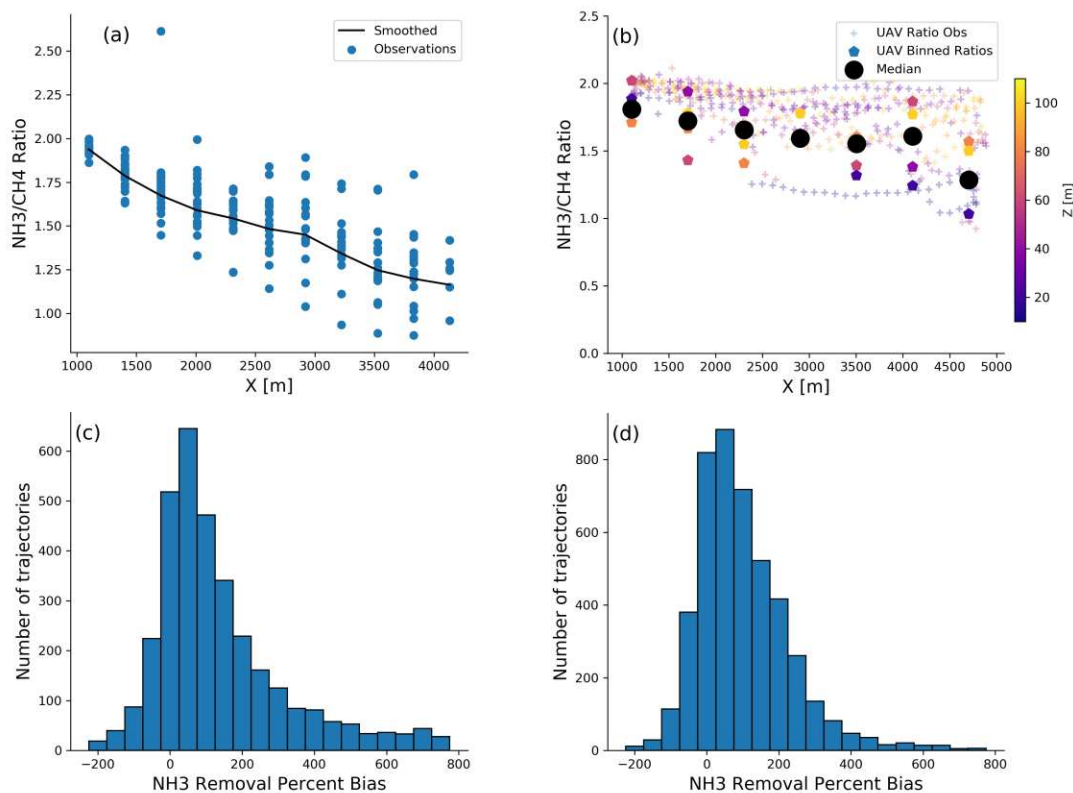


Figure 3.6: (a) Observed ammonia/methane ratios for the surface-vehicle-based and (b) sUAS-based observations with binned-by-X values overlaid. The surface vehicle base-case trajectory used a 2-hour sampling period, the sUAS trajectory used a 45 minute sampling period. The bottom two panels present histograms of the percent bias for the fraction of ammonia removed that can be inverted from a given sampling trajectory, compared to the actual deposited fraction computed with the direct offline calculation over the corresponding spatial interval. Panel (c) shows the vehicle results and (d) shows the sUAS results.

individual vehicle-based pseudo-observations, as these are real-time samples in a turbulent atmosphere. However, the bin-mean concentration ratio in Figure 3.6a follows a similar decaying pattern to Figure 3.3c with increasing X due to the surface deposition of ammonia. According to the change in the surface ratio, from the CAFO boundary (X=1100 m) to the end of the vehicle trajectory (X = 4200 m), ~40% of the total ammonia has been removed from the atmosphere, which

is almost twice what was calculated using the entire domain conductance (Figure 3.3); this high bias, when sampled at the surface, was expected from the results shown in Figure 3.4.

Figure 3.6b shows the results for the sUAS-based observations, where the symbol color denotes the altitude (z-coordinate) of the observation. Co-located ammonia and methane observations are divided to calculate the individual ratio values plotted with the '+' symbols; if either species is less than our mask, we throw out both observations. There is more scatter compared to the vehicle observations (Figure 3.6a) because the sUAS moves faster and samples a larger spatial area than the vehicle, including positions off the plume centerline. To aggregate the observations into a single decaying function, we bin the individual sUAS ammonia and methane observations by X and by Z and calculate the mean concentration of each species in each bin; the z-bins are 30 m, and the X-bins are 600 m. We chose larger x bins compared to the surface vehicle because increased rates of masking and further subdivision by Z could cause smaller sample sizes for smaller bins. We then calculate the ratio of each bin-mean concentration, which are shown in Figure 3.6b as hexagonal markers colored by Z-bin center. Finally, for each x-bin, we calculate the median of the corresponding z-bins, which are plotted in the black hexagons. From the sUAS-observations, there is less of a decrease in the ammonia:methane ratio with distance compared to the surface observations as expected from Figure 3.4. Based on the median concentration ratios, approximately 27% of the total ammonia is removed from the CAFO boundary (x=1100 m) to the end of the sUAS trajectory (X=4600 m). The sUAS estimate (27% removal) is closer than the vehicle estimate (40%) to the result shown in Figure 3.3c (20%), which is an expected result, given the discussion of Figure 3.4.

The results presented so far have been calculated based on the base-case trajectories, which require specific placement of the measurement platforms relative to the CAFO, mean wind

direction, and atmospheric stability, which determines the rate of vertical mixing. In real field deployments, due to changing wind directions, the position of roads, various private property concerns, or the presence of a potentially interfering source, it may not be possible to measure directly downwind of a CAFO as we have studied here with our simulated sampling routes. To test the robustness of this measurement approach against deviations from the base-case trajectories (Figure 3.1), we used the same SAM output and conducted a series of sensitivity pseudo-measurements where we varied the following: sampling path length, X offset from the CAFO boundary, y offset from the plume centerline, z offset (i.e., putting the instrument inlet on a mast or flying the sUAS higher or lower), angular offset from the mean wind direction, as well as the time-of-day of sampling, and the sampling duration. We conducted 1300 sensitivity trajectories for each measurement platform. The results of the sensitivity sampling trajectories are shown in histograms in Figure 3.6c and 3.6d (automobile and sUAS, respectively), where the trajectories are binned by the percent bias in predicted ammonia removal compared to the actual ammonia removed over the corresponding x-interval. Both sampling platforms have a skewed distribution. While the difference in the modal center for both distributions is minor (0% bias for the sUAS, 50% for the vehicle), the sUAS distribution is narrower than the surface vehicle. This implies that while both measurement platforms can be accurate, the sUAS method is more robust against real-world limitations on sensor placement.

In addition to the accuracy (i.e., associated bias) and precision (i.e., associated scatter and robustness against deviations from the "ideal" sampling trajectory) of a given measurement platform, it is also useful to understand which variables contribute most to bias and error. In Figure 3.7, we plotted the bias and scatter of the observations as a function of the spatial perturbations (x, y, and z) for both the sUAS and surface vehicle platforms. In this analysis, we shifted the whole

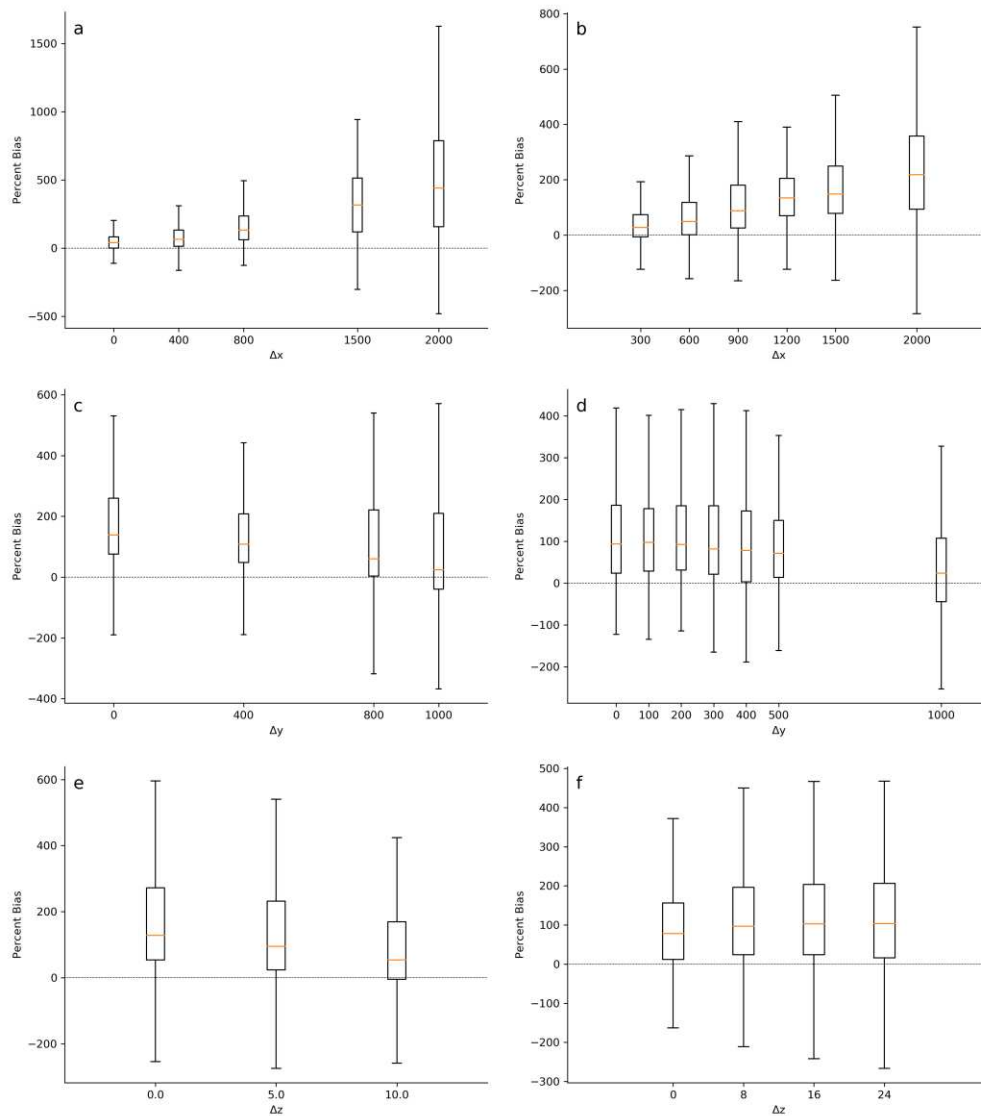


Figure 3.7: (a) Observed ammonia/methane ratios for the surface-vehicle-based and (b) sUAS-based observations with binned-by-X values overlaid. The surface vehicle base-case trajectory used a 2-hour sampling period, the sUAS trajectory used a 45 minute sampling period. The bottom two panels present histograms of the percent bias for the fraction of ammonia removed that can be inverted from a given sampling trajectory, compared to the actual deposited fraction computed with the direct offline calculation over the corresponding spatial interval. Panel (c) shows the vehicle results and (d) shows the sUAS results.

standard sampling trajectories for sUAS and the surface vehicle (Figure 3.1) in space. At each perturbed location, we rotated the trajectories from 0 to 30 degrees off the central axis sampled at 4 different start times offset by up to 2 hour to generate a distribution of expected biases. The perturbations in the X (downwind) direction have the largest effect for both platforms, with the

median bias for the surface vehicle approach increasing by a factor of two with only an 800m offset from the source. Furthermore, there is an increase associated with the error, or spread in deposition bias, associated with increasing distance from the source. For an X perturbation of 1500m, the results for a surface vehicle have an average bias of 400%, but the range of results for this method span -100% to +1000% mean bias. It is important to note that a 1500m X offset from the source is a reasonable experimental constraint, given private property and land-use constraints. The sUAS is also sensitive to an offset in the downwind distance, as almost all of the high-bias sUAS trajectories are associated with a large x-offset. The effect is small until the offset exceed 500 m. This is because the vertical mixing of the plume away from the surface has not placed a substantial fraction of the plume above the sUAS's maximum-allowed flight altitude of 120 m until further from the source under our simulated conditions. However, beyond 500 m, the bias associated with the sUAS measurement platform increases rapidly and the error associated with this measurement technique also increases.

In general, both measurement platforms are less sensitive to perturbations in the y (crosswind) and z directions. Perturbations in the y direction do not impact the total bias associated with a given approach. Likewise, there is not an obvious effect on the modal width (i.e., precision) associated with either measurement platform. The perturbations in the z direction have a small effect on the surface vehicle, where increasing the height of the measurement reduce the bias; this is expected, as the vehicle is able to sample a more-representative height within the plume where the deposition signal will be damped by transport from the surface. However, real-world implementation of this measurement would require mounting a long mast on a moving vehicle which would be a challenging experimental technique for masts longer than 10 m, and the improvement to the measurement is small. The effect of z-displacement on the sUAS results is

negligible. We explored the impact of perturbations in other parameters (trajectory angle relative to mean wind, time of day, duration of sampling period), but none had a noticeable effect on the bias. These results are presented in Appendix B3. It is also important to note that these perturbations shown here and in the appendix (other than the time-of-day) do not alter the underlying atmospheric state or dispersion. Under more stable conditions, we expect the sensitivity of the measurement approach to be less sensitive to the downwind distance, as vertical mixing will be less rapid; conversely, under extremely unstable conditions, it may not be possible to sample the plume adequately while complying with the FAA-stipulated 120m operational flight ceiling.

From the results shown here, it follows that by using observations of ammonia and methane concentrations, we can quantify the near-field deposition of ammonia by analyzing the change in the ammonia/methane concentration ratios. While using observed concentrations at the surface is likely to overestimate the ammonia removal rate by a factor of approximately 2, this can still provide an estimated upper bound for the total ammonia removal (the likelihood of underprediction from surface observations is small). Furthermore, by measuring on a sUAS up to 120 m, which is allowed without FAA certification, we show that the ammonia removal can be determined much more accurately than by surface observations alone, and that this is robust across deviations from an ideal flight path. However, under the atmospheric conditions that were simulated, it is important to minimize the distance from the feedlot boundary in order to avoid potential sources of high bias to the deposition result.

3.3.4 Approximations, Limitations, and Implications for Real Measurements

It is important to note that our study makes several assumptions and simplifications: (1) We assume that emissions and transport are close to constant for the duration of the sampling period. Therefore, this measurement approach would be most successfully implemented during

periods when the transport and temperature conditions are not changing. (2) We made our ammonia and methane sources perfectly co-located. If the sources of the two species are offset, we expect errors from using the species ratios to be larger than what we estimate here. (3) We neglect the presence of contaminating sources and background variability. Because this method is a mass balance, other sources of either ammonia or methane would cause errors in estimating the deposition rate. Therefore, the presence of other sources of ammonia (e.g., fertilized crops, waste water treatment facilities) or methane (e.g., oil and gas development sites, landfills) or both (e.g., other CAFOs) could pose problems to real-world implementation of this measurement strategy. Additional sources that are suitably upwind should not pose a problem, provided the plume is well-mixed by the time it encounters the source of interest, and that variability in these upwind sources is small enough that the background concentrations of either ammonia or methane do not undergo significant variability.

We note that while the emission rates of both species are known for these simulations, they do not need to be known to produce an estimate of the deposited fraction, as we only look at the change in ammonia concentrations relative to the change in methane. Other than differentiating the in-plume concentrations from background variability, this method does not depend on the absolute concentrations provided they are larger than the surface compensation point, and our measurement system can resolve spatial differences in the plume concentration. Furthermore, this approach does not require *a priori* information about the magnitude of the deposition velocity; in fact, quantifying the fractional deposition of ammonia may help constrain the value of the average deposition velocity over the spatial interval, though this is beyond the scope of the present study. It is also important to acknowledge that mounting sensitive ammonia and methane instruments on a sUAS is challenging, but given the recent developments of sensitive lightweight sensors and

sUAS sensor deployment, it is reasonable to expect this capability to be more readily available in the near future (McHale et al., 2016; Shadman et al., 2016). While we know of no commercially available instruments with the proper measurement specifications in terms of weight and power requirement, prototype open-path ammonia (Shadman, 2018) and methane (McHale, 2018) sensors with this application in mind have been designed and are presently undergoing testing on a sUAS platform. Furthermore, the development of sensors with sUAS capabilities is a high priority for the community (e.g., Khan et al., 2012; Whitehead et al., 2014; Yang et al., 2018). Therefore, such measurements may be routinely available within a few years. In this study, we have demonstrated an application where sUAS sensors can greatly simplify the determination of a difficult-to-measure quantity.

When using surface-based measurements to constrain dispersion and deposition, many studies employ inverse modelling tools to properly account for vertical dispersion effects (e.g., McGinn et al., 2016), which is the source of high bias in our surface-based methods. Inverse modelling is a powerful collection of techniques that can be used to deduce information about plume dispersion between the point of emission and the point of measurement. However, even state-of-the-art inverse modelling tools either fail to represent the real-time plume structure adequately under turbulent conditions (e.g., Gaussian or advection-dispersion models) or do not account for deposition or bidirectional surface interactions (e.g., backward Lagrangian stochastic methods such as WINDTRAX). While it is in principle possible to use a model to correct for the surface-bias in our measurement approach, the implementation for a dry-depositing species is challenging. The development of inverse modelling techniques to estimate ammonia during dispersion is an active area of research and beyond the scope of this study.

In this study, we have focused on simulated atmospheric state from northern CO in June, 2013. While this represents a small fraction of all meteorological conditions that occur adjacent to CAFOs, it is not possible to explore all possible atmospheric states downwind of a representative number of CAFO locations. In northern CO, ammonia emissions and their impact on CFR air quality and N_R deposition in the nearby rocky mountain ecosystems is a topic of concern for the National Park Service (“High elevations under threat from nitrogen deposition,” 2016). The N_R deposition is driven primarily by diurnal mountain-valley circulation in the summer and synoptic-scale systems in the spring. Therefore, we have repeated this study for April 1st, 2013 to verify that the approach performs well under another set of atmospheric conditions. The results suggest that the total fraction of ammonia recapture is smaller, due to different turbulent structure in the atmosphere, and that while the sUAS out-performs the surface vehicle, the difference between the two platforms is smaller. The detailed results can be found in Appendix B2. Likewise, we do not test the viability of this approach during the night. During stable stratified night time conditions, LES models often require extremely high resolution in order to reproduce the low-turbulence conditions, making these types of simulations difficult to perform (Zhou and Chow, 2011). Likewise, many field measurement techniques for quantifying surface fluxes (e.g., eddy-covariance and flux-gradient methods) are ineffective at night due to lack of turbulence (Goulden et al., 1996; Högström et al., 1989; Wu et al., 2015). The method we propose in this study could in principal work at night, as it is based on conservation of mass, rather than assumptions about turbulent transport near the surface. However, other practical limitations, such as safely operating a fixed-wing sUAS at night, could pose a challenge. Adapting this methodology for night time, and testing its accuracy and precision, is an important next step in the development of this measurement strategy.

3.4 Conclusions

In this study, we have demonstrated and tested a novel approach for quantifying nearfield ammonia deposition adjacent to a CAFO using LES of turbulent dispersion from an area source. This method uses the ratio of background-corrected ammonia/methane to simultaneously constrain the dispersion, allowing us to construct a mass balance on ammonia as it mixes downwind of the source. Neglecting chemical loss of ammonia or uptake by aerosols (Staebler et al., 2009), the residual from the mass balance is the deposited quantity of ammonia. In our test simulations, the model parameters we selected produced a system where approximately 25% of the total ammonia is removed within the first 3 km downwind of the source. Outside of the first 3 km, a relatively small fraction of the total deposition occurs as the atmospheric layers near the surface are depleted of ammonia; however, given the magnitude of the total ammonia emissions, the subsequent far-field dry deposition can still constitute a large BAN input to sensitive ecosystems. Furthermore, if the emissions enter a precipitating cloud, much of the remaining ammonia can be efficiently removed from the atmosphere via wet deposition. While these results from the simulation do not correspond to any particular CAFO, a qualitatively similar result has been found in observational studies of ammonia deposition adjacent to CAFOs; most of the dry deposition of ammonia occurs within a small distance on the order of 2-5 km, and beyond this boundary, the fractional deposited mass is much smaller (McGinn et al., 2016; Shen et al., 2018, 2016).

We tested two mobile measurement strategies, one based on a surface vehicle and one on a sUAS, and sampled our model output to produce synthetic observations of ammonia and methane downwind of the source; we found that subject to reasonable constraints, we were able to reproduce the ammonia deposition results found with the full model output. The surface vehicle result was biased high by approximately 40%, as suggested in our use of full SAM output. The sUAS result

reproduced the deposited fraction without a systematic bias, which was also suggested by the full-model results. Because deposition depletes the ammonia from the surface layer in the atmosphere, the estimated fraction of ammonia removed is much larger when only considering concentrations near the surface; however, our method is based on conservation of mass, so the deposition rate must be calculated with respect to the total column loading of ammonia, with methane to control for horizontal dispersion. Therefore, the high bias in the deposition rate derived from surface-only observations is not surprising. While it is in principle possible to correct for the high bias using inverse modelling approaches, such modelling approaches are not straightforward for species that undergo dry deposition. In contrast, the sUAS samples enough of the vertical extent of the plume that we are able to obtain an estimate for the deposition rate with little or no bias, without using a model to correct the results. Next, we performed sensitivity analysis of the measurement platform trajectories where we perturbed the measurement positions spatially and temporally. This was intended to test the robustness of the method against real-world constraints on vehicle or sUAS positions and changing wind directions. While this introduced some variability in the resulting deposition calculation, the distributions are centered around the base-case trajectory values, and the sUAS trajectory perturbations appeared to have a smaller effect on the results. We believe that this measurement principle could be successfully implemented to accurately estimate the nearfield ammonia deposition adjacent to a CAFO if simultaneous ammonia and methane measurements on a sUAS platform are possible, or that an upper bound could be more easily measured from surface vehicles.

Logistically, we anticipate a few additional challenges to implementing this method in the field that our analysis does not explicitly account for: (1) the CAFO emissions need to be sufficiently large that variability in the background and the presence of other small sources of

ammonia and methane in the region can safely be neglected; (2) the CAFO emissions cannot change significantly during the 2-hour measurement time period; (3) the land downwind of the CAFO needs to be accessible for observations by either vehicles or sUAS, and operating a sUAS on public property or private property without explicit consent from the land owners can be legally challenging; this is complicated by changes to the mean wind direction constantly requiring relocation of the measurement trajectories; designing methane and ammonia measurements that can operate safely on a sUAS platform is a challenging engineering problem. However, we do not believe any of these challenges are insurmountable. Large CAFOs that dominate the local ammonia and methane emissions exist in many places in the western US and while CAFO emissions are a function of atmospheric state as well as management practices and activities, we do not expect the emission fluxes to change dramatically over a short sampling time period. Furthermore, obtaining permission to make measurements on the adjacent land is a common procedure in Earth and environmental science disciplines. Finally, given the advances in optical measurements and sUAS technology, we believe that while challenging, such a measurement system is possible with today's technology (McHale et al., 2016; Shadman et al., 2016) and may be easy to implement in near future. There are numerous advantages to our recommended approach as well: (1) it does not require observations as fast as required for eddy covariance techniques (e.g., 20hz); (2) because we are using real-time measurements, and due to the small number of instruments required, a single measurement period can be as short as 45 minutes, allowing for rapid deployment and sampling under certain meteorological conditions or certain activities at the CAFO; (3) because these measurements are real-time optical measurements of atmospheric mixing ratios, there is no need to perform soil or leaf nitrogen measurements in a lab after the fact. Therefore, we believe that this measurement approach could be a useful addition to the different

ways we measure ammonia deposition. Finally, while we have centered our analysis around ammonia deposition near a CAFO, this basic measurement approach can be used to quantify any surface flux (deposition or emissions) over a homogeneous source/sink when the depositing species is co-emitted with an inert, non-depositing species.

REFERENCES

- Aref'ev, V.N., Akimenko, R.M., Kashin, F.V., Upenek, L.B., 2016. Background component of methane concentration in surface air (Obninsk monitoring station). *Izv. Atmos. Ocean. Phys.* 52, 37–44. <https://doi.org/10.1134/S0001433815060031>
- Asem-Hiablíe, S., Battagliese, T., Stackhouse-Lawson, K.R., Alan Rotz, C., 2019. A life cycle assessment of the environmental impacts of a beef system in the USA. *Int J Life Cycle Assess* 24, 441–455. <https://doi.org/10.1007/s11367-018-1464-6>
- Beem, K.B., Raja, S., Schwandner, F.M., Taylor, C., Lee, T., Sullivan, A.P., Carrico, C.M., McMeeking, G.R., Day, D., Levin, E., Hand, J., Kreidenweis, S.M., Schichtel, B., Malm, W.C., Collett, J.L., 2010. Deposition of reactive nitrogen during the Rocky Mountain Airborne Nitrogen and Sulfur (RoMANS) study. *Environmental Pollution* 158, 862–872. <https://doi.org/10.1016/j.envpol.2009.09.023>
- Benedict, K.B., Carrico, C.M., Kreidenweis, S.M., Schichtel, B., Malm, W.C., Collett, J.L., 2013. A seasonal nitrogen deposition budget for Rocky Mountain National Park. *Ecological Applications* 23, 1156–1169. <https://doi.org/10.1890/12-1624.1>
- Berner, A.H., Bretherton, C.S., Wood, R., 2015. Large eddy simulation of ship tracks in the collapsed marine boundary layer: a case study from the Monterey area ship track experiment. *Atmospheric Chemistry and Physics* 15, 5851–5871. <https://doi.org/10.5194/acp-15-5851-2015>
- Boucher, O., Randall, D.A., Artaxo, P., Bretherton, C., Feingold, G., Forster, P., Kerminen, V.-M., Kondo, Y., Liao, H., Lohmann, U., Rasch, P., Satheesh, S.K., Sherwood, S., Stevens, B., Zhang, X.-Y., n.d. Clouds and Aerosols, in: *Climate Change 2013: The Physical*

Science Basis. Contribution of Working Group I to the Fifth Assessment Report of the Intergovernmental Panel on Climate Change. Cambridge University Press, Cambridge, United Kingdom and New York, NY USA.

Damme, M.V., Clarisse, L., Whitburn, S., Hadji-Lazaro, J., Hurtmans, D., Clerbaux, C., Coheur, P.-F., 2018. Industrial and agricultural ammonia point sources exposed. *Nature* 564, 99. <https://doi.org/10.1038/s41586-018-0747-1>

Dockery, D.W., Pope, C.A., Xu, X., Spengler, J.D., Ware, J.H., Fay, M.E., Ferris, B.G.Jr., Speizer, F.E., 1993. An Association between Air Pollution and Mortality in Six U.S. Cities. *New England Journal of Medicine* 329, 1753–1759. <https://doi.org/10.1056/NEJM199312093292401>

Eilerman, S.J., Peischl, J., Neuman, J.A., Ryerson, T.B., Aikin, K.C., Holloway, M.W., Zondlo, M.A., Golston, L.M., Pan, D., Floerchinger, C., Herndon, S., 2016. Characterization of Ammonia, Methane, and Nitrous Oxide Emissions from Concentrated Animal Feeding Operations in Northeastern Colorado. *Environ. Sci. Technol.* 50, 10885–10893. <https://doi.org/10.1021/acs.est.6b02851>

Farquhar, G.D., Firth, P.M., Wetselaar, R., Weir, B., 1980. On the Gaseous Exchange of Ammonia between Leaves and the Environment: Determination of the Ammonia Compensation Point. *Plant Physiology* 66, 710–714. <https://doi.org/10.1104/pp.66.4.710>

Flechard, C.R., Fowler, D., 1998. Atmospheric ammonia at a moorland site. II: Long-term surface-atmosphere micrometeorological flux measurements. *Quarterly Journal of the Royal Meteorological Society* 124, 759–791. <https://doi.org/10.1002/qj.49712454706>

- Gentine, P., Bellon, G., van Heerwaarden, C.C., 2014. A Closer Look at Boundary Layer Inversion in Large-Eddy Simulations and Bulk Models: Buoyancy-Driven Case. *J. Atmos. Sci.* 72, 728–749. <https://doi.org/10.1175/JAS-D-13-0377.1>
- Gentine, P., Garelli, A., Park, S.-B., Nie, J., Torri, G., Kuang, Z., 2016. Role of surface heat fluxes underneath cold pools. *Geophysical Research Letters* 43, 874–883. <https://doi.org/10.1002/2015GL067262>
- Gong, L., Lewicki, R., Griffin, R.J., Tittel, F.K., Lonsdale, C.R., Stevens, R.G., Pierce, J.R., Malloy, Q.G.J., Travis, S.A., Bobmanuel, L.M., Lefer, B.L., Flynn, J.H., 2013. Role of atmospheric ammonia in particulate matter formation in Houston during summertime. *Atmospheric Environment* 77, 893–900. <https://doi.org/10.1016/j.atmosenv.2013.04.079>
- Goulden, M.L., Munger, J.W., Fan, S.-M., Daube, B.C., Wofsy, S.C., 1996. Measurements of carbon sequestration by long-term eddy covariance: methods and a critical evaluation of accuracy. *Global Change Biology* 2, 169–182. <https://doi.org/10.1111/j.1365-2486.1996.tb00070.x>
- Gu, B., Sutton, M.A., Chang, S.X., Ge, Y., Chang, J., 2014. Agricultural ammonia emissions contribute to China's urban air pollution. *Frontiers in Ecology and the Environment* 12, 265–266. <https://doi.org/10.1890/14.WB.007>
- Hacker, J.M., Chen, D., Bai, M., Ewenz, C., Junkermann, W., Lief, W., McManus, B., Neininger, B., Sun, J., Coates, T., Denmead, T., Flesch, T., McGinn, S., Hill, J., 2016. Using airborne technology to quantify and apportion emissions of CH₄ and NH₃ from feedlots. *Anim. Prod. Sci.* 56, 190–203. <https://doi.org/10.1071/AN15513>

- Högström, U., Bergström, H., Smedman, A.-S., Halldin, S., Lindroth, A., 1989. Turbulent exchange above a pine forest, I: Fluxes and gradients. *Boundary-Layer Meteorol* 49, 197–217. <https://doi.org/10.1007/BF00116411>
- Hristov, A.N., Hanigan, M., Cole, A., Todd, R., McAllister, T.A., Ndegwa, P.M., Rotz, A., 2011. Review: Ammonia emissions from dairy farms and beef feedlots. *Canadian Journal of Animal Science* 91, 1–35. <https://doi.org/10.1139/CJAS10034>
- Khairoutdinov, M.F., Randall, D.A., 2003. Cloud Resolving Modeling of the ARM Summer 1997 IOP: Model Formulation, Results, Uncertainties, and Sensitivities. *J. Atmos. Sci.* 60, 607–625. [https://doi.org/10.1175/1520-0469\(2003\)060<0607:CRMOTA>2.0.CO;2](https://doi.org/10.1175/1520-0469(2003)060<0607:CRMOTA>2.0.CO;2)
- Khairoutdinov, M.F., Randall, D.A., 2002. Similarity of Deep Continental Cumulus Convection as Revealed by a Three-Dimensional Cloud-Resolving Model. *J. Atmos. Sci.* 59, 2550–2566. [https://doi.org/10.1175/1520-0469\(2002\)059<2550:SODCCC>2.0.CO;2](https://doi.org/10.1175/1520-0469(2002)059<2550:SODCCC>2.0.CO;2)
- Khan, A., Schaefer, D., Tao, L., Miller, D.J., Sun, K., Zondlo, M.A., Harrison, W.A., Roscoe, B., Lary, D.J., 2012. Low Power Greenhouse Gas Sensors for Unmanned Aerial Vehicles. *Remote Sensing* 4, 1355–1368. <https://doi.org/10.3390/rs4051355>
- Li, Y., Schichtel, B.A., Walker, J.T., Schwede, D.B., Chen, X., Lehmann, C.M.B., Puchalski, M.A., Gay, D.A., Collett, J.L., 2016. Increasing importance of deposition of reduced nitrogen in the United States. *PNAS* 113, 5874–5879. <https://doi.org/10.1073/pnas.1525736113>
- Lonsdale, C.R., Alvarado, M.J., Hodshire, A.L., Ramnarine, E., Pierce, J.R., 2019. Simulating Forest Fire Plume Dispersion, Chemistry, and Aerosol Formation Using SAM-ASP version 1.0. *Geoscientific Model Development Discussions* 1–19. <https://doi.org/10.5194/gmd-2019-221>

- Loubet, B., Decuq, C., Personne, E., Massad, R.S., Flechard, C., Fanucci, O., Mascher, N., Gueudet, J.-C., Masson, S., Durand, B., Genermont, S., Fauvel, Y., Cellier, P., 2012. Investigating the stomatal, cuticular and soil ammonia fluxes over a growing tritical crop under high acidic loads. *Biogeosciences* 9, 1537–1552. <https://doi.org/10.5194/bg-9-1537-2012>
- Loubet, B., Milford, C., Hensen, A., Daemmgen, U., Erisman, J.-W., Cellier, P., Sutton, M.A., 2009. Advection of NH₃ over a pasture field and its effect on gradient flux measurements. *Biogeosciences* 6, 1295–1309. <https://doi.org/10.5194/bg-6-1295-2009>
- McGinn, S.M., Flesch, T.K., Crenna, B.P., Beauchemin, K.A., Coates, T., 2007. Quantifying Ammonia Emissions from a Cattle Feedlot using a Dispersion Model. *Journal of Environmental Quality* 36, 1585–1590. <https://doi.org/10.2134/jeq2007.0167>
- McGinn, S.M., Janzen, H.H., Coates, T.W., Beauchemin, K.A., Flesch, T.K., 2016. Ammonia Emission from a Beef Cattle Feedlot and Its Local Dry Deposition and Re-Emission. *Journal of Environmental Quality* 45, 1178–1185. <https://doi.org/10.2134/jeq2016.01.0009>
- McHale, L., 2018. Development of mobile open-path cavity ring-down spectrometer for measurement of trace atmospheric methane gas (Thesis). Colorado State University. Libraries.
- McHale, L.E., Hecobian, A., Yalin, A.P., 2016. Open-path cavity ring-down spectroscopy for trace gas measurements in ambient air. *Opt. Express*, OE 24, 5523–5535. <https://doi.org/10.1364/OE.24.005523>

- McLaughlin, A., Mineau, P., 1995. The impact of agricultural practices on biodiversity. *Agriculture, Ecosystems & Environment* 55, 201–212. [https://doi.org/10.1016/0167-8809\(95\)00609-V](https://doi.org/10.1016/0167-8809(95)00609-V)
- Miller, D.J., Sun, K., Tao, L., Pan, D., Zondlo, M.A., Nowak, J.B., Liu, Z., Diskin, G., Sachse, G., Beyersdorf, A., Ferrare, R., Scarino, A.J., 2015. Ammonia and methane dairy emission plumes in the San Joaquin Valley of California from individual feedlot to regional scales. *Journal of Geophysical Research: Atmospheres* 120, 9718–9738. <https://doi.org/10.1002/2015JD023241>
- Roscioli, J.R., Zahniser, M.S., Nelson, D.D., Herndon, S.C., Kolb, C.E., 2016. New Approaches to Measuring Sticky Molecules: Improvement of Instrumental Response Times Using Active Passivation. *J. Phys. Chem. A* 120, 1347–1357. <https://doi.org/10.1021/acs.jpca.5b04395>
- Rotz, C.A., Asem-Hiablíe, S., Place, S., Thoma, G., 2019. Environmental footprints of beef cattle production in the United States. *Agricultural Systems* 169, 1–13. <https://doi.org/10.1016/j.agry.2018.11.005>
- Sakamoto, K.M., Laing, J.R., Stevens, R.G., Jaffe, D.A., Pierce, J.R., 2016. The evolution of biomass-burning aerosol size distributions due to coagulation: dependence on fire and meteorological details and parameterization. *Atmospheric Chemistry and Physics* 16, 7709–7724. <https://doi.org/10.5194/acp-16-7709-2016>
- Schrader, F., Brümmer, C., 2014. Land Use Specific Ammonia Deposition Velocities: a Review of Recent Studies (2004–2013). *Water Air Soil Pollut* 225. <https://doi.org/10.1007/s11270-014-2114-7>

- Shadman, S., 2018. Measurement of ammonia emission from agricultural sites using open-path cavity ring-down spectroscopy and wavelength modulation spectroscopy based analyzers (Thesis). Colorado State University. Libraries.
- Shadman, S., Rose, C., Yalin, A.P., 2016. Open-path cavity ring-down spectroscopy sensor for atmospheric ammonia. *Appl. Phys. B* 122, 194. <https://doi.org/10.1007/s00340-016-6461-5>
- Shen, J., Chen, D., Bai, M., Sun, J., Coates, T., Lam, S.K., Li, Y., 2016. Ammonia deposition in the neighbourhood of an intensive cattle feedlot in Victoria, Australia. *Scientific Reports* 6, srep32793. <https://doi.org/10.1038/srep32793>
- Shen, J., Chen, D., Bai, M., Sun, J., Lam, S.K., Mosier, A., Liu, X., Li, Y., 2018. Spatial variations in soil and plant nitrogen levels caused by ammonia deposition near a cattle feedlot. *Atmospheric Environment* 176, 120–127. <https://doi.org/10.1016/j.atmosenv.2017.12.022>
- Shonkwiler, K.B., Ham, J.M., 2018. Ammonia emissions from a beef feedlot: Comparison of inverse modeling techniques using long-path and point measurements of fenceline NH₃. *Agricultural and Forest Meteorology, Greenhouse gas and ammonia emissions from livestock production* 258, 29–42. <https://doi.org/10.1016/j.agrformet.2017.10.031>
- Staebler, R.M., McGinn, S.M., Crenna, B.P., Flesch, T.K., Hayden, K.L., Li, S.-M., 2009. Three-dimensional characterization of the ammonia plume from a beef cattle feedlot. *Atmospheric Environment* 43, 6091–6099. <https://doi.org/10.1016/j.atmosenv.2009.08.045>
- Stevens, R.G., Pierce, J.R., Brock, C.A., Reed, M.K., Crawford, J.H., Holloway, J.S., Ryerson, T.B., Huey, L.G., Nowak, J.B., 2012. Nucleation and growth of sulfate aerosol in coal-

- fired power plant plumes: sensitivity to background aerosol and meteorology. *Atmospheric Chemistry and Physics* 12, 189–206. <https://doi.org/10.5194/acp-12-189-2012>
- Sun, K., Tao, L., Miller, D.J., Khan, M.A., Zondlo, M.A., 2014. On-Road Ammonia Emissions Characterized by Mobile, Open-Path Measurements. *Environ. Sci. Technol.* 48, 3943–3950. <https://doi.org/10.1021/es4047704>
- Sun, K., Tao, L., Miller, D.J., Zondlo, M.A., Shonkwiler, K.B., Nash, C., Ham, J.M., 2015. Open-path eddy covariance measurements of ammonia fluxes from a beef cattle feedlot. *Agricultural and Forest Meteorology* 213, 193–202. <https://doi.org/10.1016/j.agrformet.2015.06.007>
- Sutton, M.A., Burkhardt, J.K., Guerin, D., Fowler, D., 1995. Measurement and modelling of ammonia exchange over arable croplands, in: Heij, G.J., Erisman, J.W. (Eds.), *Studies in Environmental Science, Acid Rain Research: Do We Have Enough Answers?* Elsevier, pp. 71–80. [https://doi.org/10.1016/S0166-1116\(06\)80274-8](https://doi.org/10.1016/S0166-1116(06)80274-8)
- Tao, L., Sun, K., Miller, D., Pan, D., Golston, L., Zondlo, M., 2015. Low-power, open-path mobile sensing platform for high-resolution measurements of greenhouse gases and air pollutants. *Applied Physics B: Lasers & Optics* 119, 153–164. <https://doi.org/10.1007/s00340-015-6069-1>
- Thompson, T.M., Rodriguez, M.A., Barna, M.G., Gebhart, K.A., Hand, J.L., Day, D.E., Malm, W.C., Benedict, K.B., Collett, J.L., Schichtel, B.A., 2015. Rocky Mountain National Park reduced nitrogen source apportionment. *Journal of Geophysical Research: Atmospheres* 120, 4370–4384. <https://doi.org/10.1002/2014JD022675>

- Tonnessen, K. High elevations under threat from nitrogen deposition: Air quality monitoring, research, and management at Rocky Mountain National Park (U.S. National Park Service) [WWW Document], March, 2016. URL https://www.nps.gov/articles/parkscience32_2_tonnessen_3842.htm (accessed 10.31.19).
- US EPA, O., 2016. 2014 National Emissions Inventory (NEI) Data [WWW Document]. US EPA. URL <https://www.epa.gov/air-emissions-inventories/2014-national-emissions-inventory-nei-data> (accessed 7.14.17).
- Vitousek, P.M., Menge, D.N.L., Reed, S.C., Cleveland, C.C., 2013. Biological nitrogen fixation: rates, patterns and ecological controls in terrestrial ecosystems. *Philosophical Transactions of the Royal Society B: Biological Sciences* 368, 20130119. <https://doi.org/10.1098/rstb.2013.0119>
- Whitehead, K., Hugenholtz, C.H., Myshak, S., Brown, O., LeClair, A., Tamminga, A., Barchyn, T.E., Moorman, B., Eaton, B., 2014. Remote sensing of the environment with small unmanned aircraft systems (UASs), part 2: scientific and commercial applications. *J. Unmanned Veh. Sys.* 02, 86–102. <https://doi.org/10.1139/juvs-2014-0007>
- Wu, Z.Y., Zhang, L., Wang, X.M., Munger, J.W., 2015. A modified micrometeorological gradient method for estimating O₃ dry depositions over a forest canopy. *Atmospheric Chemistry and Physics* 15, 7487–7496. <https://doi.org/10.5194/acp-15-7487-2015>
- Yang, S., Talbot, R.W., Frish, M.B., Golston, L.M., Aubut, N.F., Zondlo, M.A., Gretencord, C., McSpirtitt, J., 2018. Natural Gas Fugitive Leak Detection Using an Unmanned Aerial Vehicle: Measurement System Description and Mass Balance Approach. *Atmosphere* 9, 383. <https://doi.org/10.3390/atmos9100383>

Yang, Y., Liao, W., Wang, X., Liu, C., Xie, Q., Gao, Z., Ma, W., He, Y., 2016. Quantification of ammonia emissions from dairy and beef feedlots in the Jing-Jin-Ji district, China.

Agriculture, Ecosystems & Environment 232, 29–37.

<https://doi.org/10.1016/j.agee.2016.07.016>

Zhou, B., Chow, F.K., 2011. Large-Eddy Simulation of the Stable Boundary Layer with Explicit Filtering and Reconstruction Turbulence Modeling. *J. Atmos. Sci.* 68, 2142–2155.

<https://doi.org/10.1175/2011JAS3693.1>

CHAPTER 4. USING LOW-COST MEASUREMENT SYSTEMS TO INVESTIGATE AIR QUALITY: A CASE STUDY IN PALAPYE, BOTSWANA

Exposure to particulate air pollution is a major cause of mortality and morbidity worldwide. In developing countries, the combustion of solid fuels is widely used as a source of energy, and this process can produce exposure to harmful levels of PM_{2.5}. However, as countries develop, solid fuel may be replaced by centralized coal combustion, and vehicles burning diesel and gasoline may become common, changing the concentration and composition of PM_{2.5}, which ultimately changes the health effects. Therefore, there is a continuous need for in-situ monitoring of air pollution in developing nations, both to estimate of human exposure and to monitor for changes.

In this study, we present measurements from a 5 week field experiment in Palapye, Botswana. We used a low-cost, highly portable instrument package to measure surface-based aerosol optical depth, real-time PM_{2.5} concentrations using a third-party optical sensor, and time-integrated PM_{2.5} concentration and composition by using a cyclone to collect PM_{2.5} onto Teflon filters. Furthermore, we used other low-cost measurements of real-time black carbon and time-integrated ammonia to help interpret the PM_{2.5} composition and concentration information we obtained. We found that, while the average PM_{2.5} concentration ($9.5 \mu\text{g m}^{-3}$) are below the WHO annual limit and closely agree with GBD estimates for this region, the accumulation of sulfate and carbonaceous aerosol (33% and 27% of total PM_{2.5} mass respectively) produced moderately unhealthy concentrations ($14.5 \mu\text{g m}^{-3}$) for the first half of our measurement period.

4.1 Introduction

Exposure to particulate air pollution with aerodynamic diameters smaller than $2.5 \mu\text{m}$ ($\text{PM}_{2.5}$) is linked with premature mortality (Dockery et al., 1993) and morbidity (Pope, 2000), and is currently one of the most important causes of premature mortality in developing and rapidly industrializing nations (Forouzanfar et al., 2015). State-of-the-art methods for quantifying the global health burden of air pollution use remote sensing tools and atmospheric chemical transport models (CTMs) fused with in situ measurements to produce estimates of pollutant concentrations in regions where surface measurements are sparse (e.g. Brauer et al., 2012; van Donkelaar et al., 2011). There is uncertainty associated with each step in this process that propagate through health-impact assessments (Ford and Heald, 2016; Kodros et al., 2018). Therefore, despite advancements in CTM and remote sensing capabilities, there is a need for in situ measurements to develop process-based understanding of the sources and chemical processes that drive local and regional scale population exposure to $\text{PM}_{2.5}$. Specifically, estimates of mortality due to air pollution exposure in sub-Saharan Africa are large (Kodros et al., 2018), and in situ measurements of air pollution are rare.

Over 40% of the population in sub-saharan African nations uses domestic biomass burning for heating and cooking (Bonjour et al., 2013; Forouzanfar et al., 2015). However, estimates of emissions from domestic biomass burning vary (Bond et al., 2004; Coffey et al., 2017), leading to uncertainty in the representation of these sources in regional and global CTMs, which propagates to estimates of disease burden (Kodros et al., 2018). Moreover, as sub-saharan African nations undergo economic development, the important regional sources of aerosols will change, as coal combustion for electricity production replace domestic solid fuel use, and fossil fuel vehicles become more common (Marais et al., 2019). Therefore, many different measurement studies of

various air pollutants and precursors will become increasingly important to capture these changes in emissions and to reduce uncertainties of population-level exposure. Furthermore, “sub-saharan Africa” refers to a large collection of countries with different climate regions and cultures, spanning an area three times the size of the United States. While there have been some measurements of combustion emissions in some locations in southern Africa, combustion emissions vary considerably from one country to the next, and the number and duration of studies currently in the literature is inadequate to accurately represent the entire region.

Botswana is a medium-sized African nation. While sparsely populated, it is experiencing population growth and rapid economic development and industrialization (“Statistics Botswana,” 2017). Consequently, the sources, and therefore the magnitude, composition, exposure, and impact of human exposure to $PM_{2.5}$ is rapidly changing. According to recent global estimates, air pollution in Botswana is not currently a major public health concern (Forouzanfar et al., 2015) but may become one as economic development progresses (Marais et al., 2019). Additionally, biomass burning is widely used in Botswana for cooking and heating, and the use of household solid fuels has been directly linked to poor health outcomes in the capital city of Gaborone (Kelly et al., 2015). However, Botswana also produces electricity using coal power plants; according to official estimates, domestic electrical generating capacity has increased by over 50% in the last three years (Statistics Botswana). Coal power plants emit precursors for sulfate and sulfuric acid, and there are multiple examples of coal power plant emissions impacting ambient $PM_{2.5}$ concentrations, which in turn affect human health (Dockery et al., 1993). Furthermore, increases in the size of the Botswana automobile fleet, which has more than doubled in size since 2002 (“Transport and Infrastructure Report” 2017), can also contribute to $PM_{2.5}$ exposure. Because of these rapid changes, the role $PM_{2.5}$ plays in public health in Botswana is also likely changing.

In situ air quality monitoring traditionally has required expensive instrumentation and technical expertise to operate the instruments continuously. The cost of conducting these measurements can be prohibitive for many developing nations, and thus datasets to evaluate satellite/model estimates of air pollution exposure, such as from the GBD, are often unavailable. Therefore, there is a need to develop lower-cost approaches for assessing air pollution. The development of low-cost sensors to measure atmospheric pollutants such as PM_{2.5}, ozone, NO_x (etc... include citations) is an active area of research. Many of these sensors sacrifice accuracy and precision in order to reduce manufacturing and operational costs; therefore, they may not be suitable for some research questions or in situ monitoring applications (Clements et al., 2017). However, lower cost per sensor may allow for the deployment of more sensors, and integration with IoT technology may allow for distributed sensor networks, which can open the door for new research methodologies (Rai et al., 2017). It is important to understand the technical limitations of these instrument platforms, and how the tradeoff in accuracy and precision can impact the types of research and monitoring applications that are feasible. Furthermore, there are other practical limitations of the use of new sensor platforms in real-world scenarios that are difficult to anticipate without pilot-scale studies. Therefore, in addition to sensor validation studies where low-cost measurement techniques are compared to established methods or data sources, field measurements under many different scenarios, such as deployment in challenging conditions, or with limited access to different types of infrastructure, are required to understand the practical limitations, in addition to the technical limitations, of this new generation of sensors.

In June 2018, a collaboration between North Carolina A&T University (NCAT) and Botswana International University of Science and Technology (BIUST) was started to establish a long-term record of surface-based sunphotometer measurements of aerosol optical depth. During

a 5-week visit to establish the measurement protocol, we also deployed a suite of low-cost instruments in order to better understand the aerosol concentration and composition in this region during the five week measurement period. The primary instrument that we deployed during the 5 weeks was the Aerosol Mass and Optical Depth (AMOD) device, developed for a Citizen Science project (CEAMS) (Ford et al., 2019; Wendt et al., 2019); the AMOD collects PM_{2.5} mass on a teflon filter, while simultaneously conducting a surface-based aerosol optical depth measurement and measuring real-time PM₁, PM_{2.5}, and PM₁₀ from a third party optical sensor (Plantower PMS 5003). In addition to the AMOD, we collected time-integrated samples of gas-phase ammonia, as well as real-time black carbon concentrations using two low-cost commercial measurements. To our knowledge, these are the first measurements of aerosol concentrations and composition in this region in Botswana that have been published. In this study, we present the results of the measurements and post-measurement analysis. Here we will compare the total measured PM_{2.5} concentrations to Global Burden of Disease estimates, as well as present speciated-PM results, put the PM measurements in context of AOD measured by the AMOD and satellites, and briefly discuss the important sources for PM_{2.5} in this region.

4.2 Methods.

4.2.1 Site Description and Important Sources

The measurements were made on the campus of the Botswana International University of Science and Technology (BIUST) located in Palapye, Botswana. Palapye is a village located at 22.59 °S, 27.12 °E, more than 150 km from the nearest major metropolitan area (Figure 4.1). Palapye is located in a semi-arid climate zone characterized by hot and dry weather, with less than 300 mm of precipitation annually. Our measurements were made between June 19th and July 20th

2018, which is in the southern hemisphere winter. Daytime temperatures generally range between 25 and 30°C, with nighttime lows between 0 and 6°C with little or no cloud cover during our measurement period. However, from July 5th - July 10th, the weather was overcast and cool with some light precipitation, associated with a synoptic-scale system (“Cold front expected to hit parts of SA,” SABC News, 2018; “Giraffe in the snow”, The Guardian 2018). The area surrounding Palapye consists of arid shrubland with sandy soils. Blowing and suspended dust from arid soils is an important source of coarse-mode particulate matter in this region (Wiston, 2017), though traditionally dust is not a major source of PM_{2.5}. Grazing of livestock is a major part of Botswana’s economy (Wiston, 2017), and this land is frequently used for cattle grazing as well. Cattle and other livestock can be a source of ammonia, which is a precursor for PM_{2.5} (Eilerman et al., 2016; Shonkwiler and Ham, 2018; Yang et al., 2016).

In addition to these regional sources of aerosol, there are important anthropogenic sources as well. Traditionally, developing countries rely on domestic solid-fuel combustion for energy, which is an important source of carbonaceous aerosol and is a major health concern (Forouzanfar et al., 2015). In Botswana, studies have shown that domestic biomass burning can impact ambient air quality in the capital city Gaborone (Jayaratne and Verma, 2001) and has a detectable effect on pediatric pneumonia health outcomes (Kelly et al., 2015). While the rest of Botswana also uses solid-fuel combustion for energy (Marais and Wiedinmyer, 2016), no measurement studies have been performed outside of Gaborone. In addition to domestic biomass burning, Botswana has some industrial sources, such as metal processing and coal combustion (Wiston, 2017). A notable example near Palapye is the Morupule Power Station, a coal power plant with an adjacent coal mine to provide fuel for the power station. The Morupule Power Station has been operational since 1990 but has undergone a recent expansion to a nominal capacity of 600MW, although it was not

operating at 100% capacity during our sampling period. Although it is a functioning power plant, it is not listed as operational in emission inventories used in the most-recent modelling study of

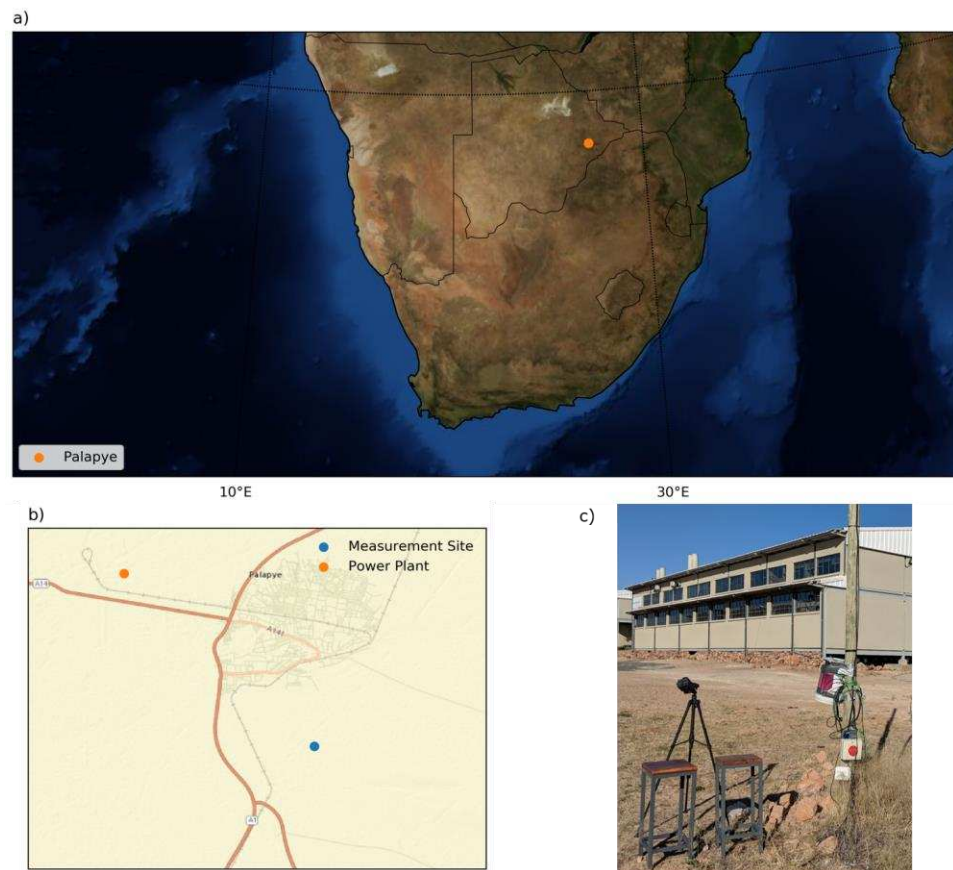


Figure 4.1: (a) map of BIUST campus relative to the village of Khurumela, the village of Palapye, the A1 Highway, and the Morupule power station (mean winds are east-north-easterly). (b) photograph of the experimental setup with the CEAMS AMOD on the black tripod, the Radiello Passive Ammonia sampler under the bucket and the AethLabs MicroAethalometerTM mounted to the wooden electrical pole.

PM_{2.5} for this region (Marais et al., 2019), so modelling studies will not capture its contributions to ambient air quality. Coal power plants are known sources of SO₂, which reacts in the atmosphere to form sulfate and sulfuric acid, and NO_x, which can affect ozone formation and form nitrate and nitric acid, but certain emission control technologies may be effective at reducing the emissions (Lonsdale et al., 2012). As the capacity of this power station increases and/or control technologies are changed, the impact on regional air quality will continue to evolve.

In addition to the power plant, Palapye experiences a variety of other potential sources of $PM_{2.5}$. The most recent census estimates indicate that the population of Palapye was 36,000 in 2011; however, the village is undergoing rapid population growth, and the 2018 population is thought to be closer to 80,000. In addition to the establishment of BIUST (target size 6000 students, plus employees), Palapye is the site of rapid construction and development, including construction of a new commercial district to support the growing population. Additionally, the growing automobile fleet, both locally and nationally, are increasing the potential impact of traffic emissions on our measurement site. The A1, which is the busiest road in Botswana, travels directly through the town center and within 5 km of our measurement site. Vehicles in Botswana exclusively use diesel fuel, which can emit more black carbon and organic aerosol precursors than other gasoline vehicles (Nelson et al., 2008). Finally, as Palapye grows, heavy construction and off-road diesel equipment may be an important source as well.

Figure 4.1a denotes the location of our sampling site relative to the BIUST campus, the villages of Khurumela and Palapye, the Morupule Power Station, and the A1. Outside of the region shown on the map, the surrounding area is sparsely populated desert shrubland with light animal grazing. In Figure 4.1b, we show our experimental setup with the CEAMS AMOD instrument mounted on a tripod (Section 4.2.2), and the MicroAethelomter (Section 4.2.3) and ammonia measurement (Section 4.2.4) secured to the wooden utility pole approximately 1.3m off the ground. The measurements are approximately 50m from the nearest structure, as shown in Figure 1B.

4.2.2 Field Measurements

To perform many of our measurements, we used the Aerosol Mass and Optical Depth (AMOD) measurement system (Wendt et al., 2019), developed with Access Sensor Technologies. The AMOD AOD measurement uses 4 photodiodes at 440, 520, 680, and 870nm to measure

optical extinction along these wavelengths. The AMOD also uses the same cyclone-filter system to collect PM_{2.5} on teflon filters from the more-widely used UPAS sensor (Volckens et al., 2017) to collect samples of PM_{2.5} for laboratory characterization described below. Finally, the AMOD devices include a third-party Plantower PMS5003 sensor, which estimates PM₁₀, PM_{2.5}, and PM₁ concentrations; however, these size bin values are based on a theoretical model rather than measurements (Kelly et al., 2017). The Plantower PMS5003 has a resolution of 1 ug/m³, and the instrument specifications suggest that it can effectively measure particles with a diameter greater than 0.5 um (98% efficiency, only 50% efficiency for 0.3 um), with concentrations in the range of 0-500ug/m³ (Yong, 2016). However, evaluation studies have suggested that it underpredicts particles in the small size bins and overpredicts in the large size bins (e.g., Kelly et al., 2017). Thus, we only show PM_{2.5} measurements here, which previous studies have shown to have good correlation with reference monitor methods (e.g., Bulot et al., 2019; Kelly et al., 2017; Sayahi et al., 2019; Wendt et al., 2019). Validation of the AMOD system can be found in Wendt et al., (2019), and an example of its application for local air quality studies can be found in Ford et al., (2019).

In this study, we used two AMOD devices to perform the measurements, deploying the sensors alternately while allowing the other sensor to recharge. Each sensor was deployed for 48 hours, with the exception of the final two measurements which were 24-hour deployments. Each filter collected PM_{2.5} for the duration of the measurement period, using a 2 litre-per-minute flow rate of ambient air. We collected 14 total samples, with an additional 6 filters that were transported to the measurement site for use as blanks. The teflon filters were sealed inside plastic containers before and after deployment. Filters were weighed pre and post deployment, and were further characterized by SootscanTM Black Carbon technique and X-ray fluorescence (XRF) to detect

inorganic elements that were present on the filter surface. Additionally, we extracted the filters in DI water and used ion chromatography to characterize the concentration of ions, and we used a Sievers TOC analyzer to measure the water-soluble organic carbon (WSOC) concentration in the filter extract. We used the average concentration of WSOC species and ionic species from the blank filters to blank-correct our measurements.

In addition to the AMOD, we used a microAeth^(R) AE51 aethalometer to measure real-time black carbon concentrations. We used a 150ml/min flowrate, and a sampling timebase of 5 minutes. The AE51 battery life was approximately 18 hours, then it would need 12 hours to recharge before being redeployed. The instrument was deployed at variable times during the day, and retrieved the following morning, where it was allowed to charge to full battery before redeployment. Therefore, the exact time of day of instrument deployment varied.

To measure the ambient gas-phase NH₃, we used RadielloTM passive NH₃ adsorption cartridges inside diffusive bodies. The cartridges were deployed for 3-4 days, depending on the cartridge, and stored in an air-tight glass vial for transport to/from Botswana. The cartridges were extracted in DI water, and the NH₄⁺ ionic concentration was determined using ion chromatography.

4.2.3 Ancillary and remote observations, and back-trajectory modelling

In addition to the measurements that we conducted, we made use of other available data. BIUST maintains a meteorological instrument station that provides measurements of windspeed, wind direction, temperature, relative humidity, and solar flux at hourly resolution. For satellite observations, we use the Moderate Resolution Imaging Spectroradiometer (MODIS) instrument aboard the Terra and Aqua polar-orbiting satellites. The MODIS instrument consists of a 36 radiometer wavelengths; the AOD product is available twice daily, in mid-morning and early

afternoon (~10:30am and 1:30pm local time). In this analysis, we use the Level 2 Dark Target retrieval 10km product.

Finally, we use NOAA HYSPLIT back-trajectory modelling to trace air parcels backwards to determine what sources may have impacted these air masses. For the HYSPLIT trajectories, we used the Frequency Back trajectory method. We initiated trajectories every 6 hours, starting at 500m above the surface, for the duration of the field measurement period. We aggregated the trajectory frequencies for the first and second halves of the measurement period (June 15-30, and July 1-15, respectively).

4.3 Results and Discussion

4.3.1 $PM_{2.5}$ concentrations at BIUST

First, we present the $PM_{2.5}$ time series from the AMOD devices in Figure 2: the real-time Plantower observations are denoted by the points, distinguishing between the two AMOD instruments; the filter observations are denoting by the horizontal black lines with the width representing the duration of the measurement period (all measurements were for 48 hours except

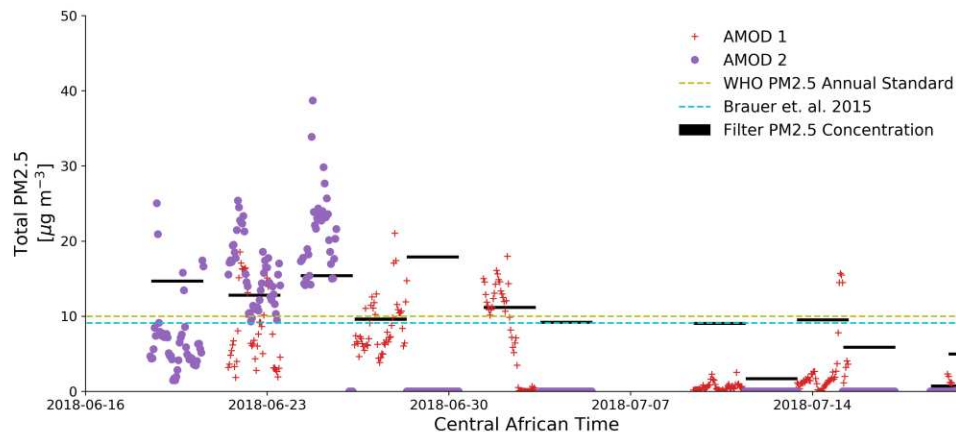


Figure 4.2: Time series plot of real-time $PM_{2.5}$ and filter $PM_{2.5}$ from the two AMOD instruments, with the estimates from the Global Burden of Disease Report (Brauer et al., 2015) and the World Health Organization annual standard overlaid.

for the last two, which were 24 hour duration). As shown in the timeseries, the Plantower sensor on AMOD 2 was offline after the third deployment of that sensor. Additionally, the sensors were not deployed during the overcast/raining period from July 5th-July 10th.

In Figure 2, the filter and Plantower measurements both show that the $PM_{2.5}$ concentrations before (June 18th-July 4th) are generally greater than the concentrations after the overcast period (July 10th-20th). The average concentration during the first half of the measurement campaign was $14.0 \mu\text{g m}^{-3}$, as compared to $6.5 \mu\text{g m}^{-3}$ during the second half of the measurement period, according to the filter-based measurements. In Figure 2, we have overlaid the World Health Organization (WHO) standard for annual average $PM_{2.5}$ concentrations ($10\mu\text{g m}^{-3}$) and the Brauer et al. (2015) estimates used for the 10 km by 10 km box around our measurement site in the 2015 GBD report ($9.1\mu\text{g m}^{-3}$). The actual average concentration during this time period was $9.4\mu\text{g m}^{-3}$, which is very close to the GBD estimate and below the WHO annual limit. However, given the limited duration of our measurements and high variability in the concentrations we observed, it is difficult to conclusively determine the actual mean concentration, or whether the “high-concentration period” or “low-concentration period” is more common in Palapye, or how these may vary seasonally. Therefore, we will attempt to use other information to identify the mechanism for this variability, in order to extract some more generalizable information about air quality in Palapye. In addition to our measurements of mean $PM_{2.5}$ concentration, we also have the characterization of the filters that we collected to provide some information on the $PM_{2.5}$ composition. Additionally, we can use the Plantower and MicroAeth observations to learn about the daily variability in $PM_{2.5}$ and black carbon, an important tracer for combustion. We will discuss the composition information in Section 4.3.2 and the temporal variability in Section 4.3.3.

4.3.2 Filter $PM_{2.5}$ composition characterization

In Figure 4.3, we show the breakdown of the filter $PM_{2.5}$ samples by different compositional types: inorganic ionic species, water-soluble organic carbon species (WSOC), and black carbon (BC); we plot the residual $PM_{2.5}$ mass in blue and refer to it as “unspeciated” $PM_{2.5}$. Each filter is blank corrected and plotted where the bar width is reflective of the sample duration (as in Figure 4.2). From Figure 4.3, we see that: (i) the most important speciated fraction of the

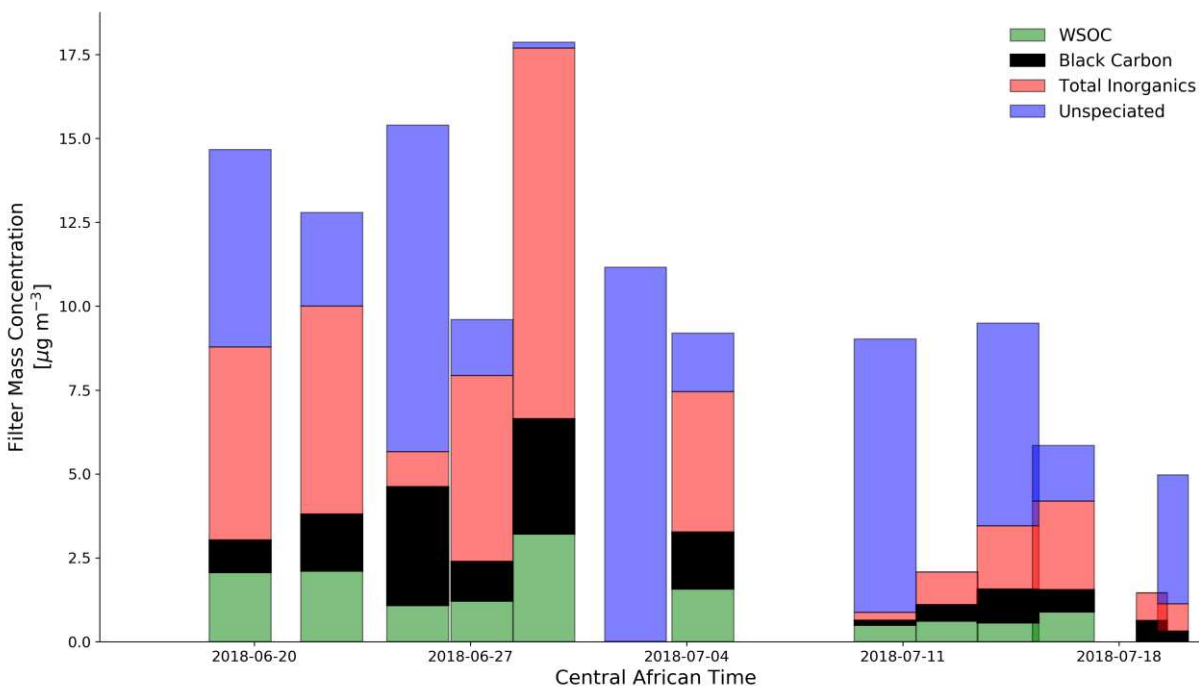


Figure 4.3: Results of analytical characterization of filters, showing the mass of black carbon (black, water-soluble organic aerosol mass (green), inorganic aerosol mass (red), and the residual unspeciated aerosol mass (blue). The width of each bar is the duration of the filter sample.

$PM_{2.5}$ mass is inorganic in nature, (ii) the black carbon mass is typical for $PM_{2.5}$ with some combustion influence, but (iii) there is little WSOC (often less than BC) on these filter samples and (iv) there remains a significant unspeciated fraction. The two most important aerosol types that could constitute the unspeciated fraction are insoluble organic aerosol species or dust. However, we do not expect dust to be an important fraction of this unspeciated aerosol mass based

on the X-ray diffraction results that will be discussed shortly. The presence of BC suggests that combustion from either domestic solid fuel use or diesel vehicles is impacting the $PM_{2.5}$ in this region. Given that Palapye is too remote to be significantly influenced by long-range transport of urban emissions in general, it is likely that the combustion is generally local. As organic aerosol ages, oxidative processes in the atmosphere increase the aerosol O/C ratio (Jimenez et al., 2009); this typically increases the solubility of the organic aerosol species in water. Because the combustion emissions impacting our measurement site may be local, the chemical compounds may have undergone less oxidation and are therefore less soluble in water.

The most important single constituent of the aerosol by mass is the inorganic ionic fraction of the aerosol. The mass concentrations for the common ionic aerosol species from the ion chromatography characterization are shown in Figure 4.4. By mass, sulfate is the most abundant ionic species in the particle phase, followed by ammonium. Sulfate and sulfuric acid is most commonly formed from the oxidation of SO_2 by two oxidation pathways: gas-phase oxidation by OH radical, and aqueous-phase oxidation inside cloud droplets. These two processes have very different timescales associated with them; the gas-phase mechanism has a lifetime of approximately 1 week, while the aqueous-phase mechanism is much faster. Given the lack of clouds in the region during the first two weeks, the gas-phase mechanism is likely dominant for this measurement site during this time period. While the Moropule Power plant is located within 10 km of the measurement site, and is likely a large regional source of SO_2 , it is unlikely that the oxidation of SO_2 is occurring quickly enough to produce lots of sulfate at the measurement site. To produce the observed mass of sulfate so close to the source of SO_2 , either the air in the region must have stagnated to prevent ventilation of SO_2 emissions, allowing the production of sulfate over a period of a few days. While there is evidence that some stagnation occurred during the

first half of the measurement period, the prevailing winds never directed emissions from the powerplant to the measurement site. However, another possibility is that the measured sulfate is regional background. South Africa generates much more electricity annually than Botswana, including electricity that is exported to Botswana and other surrounding nations. Due to South Africa's possession of rich coal deposits, coal-fire power plants are ubiquitous in the north east of the country. Therefore, a substantial fraction of the regional sulfate could be advected from the east and south.

The second-most important species in the aerosol phase is NH_4^+ , followed by sodium, chloride, potassium, and other salts that are usually associated with sea salt aerosol or dust. The masses of NH_4^+ and SO_4^{2-} on each day in Figure 4.4 generally correspond a molar ratio of 2:1,

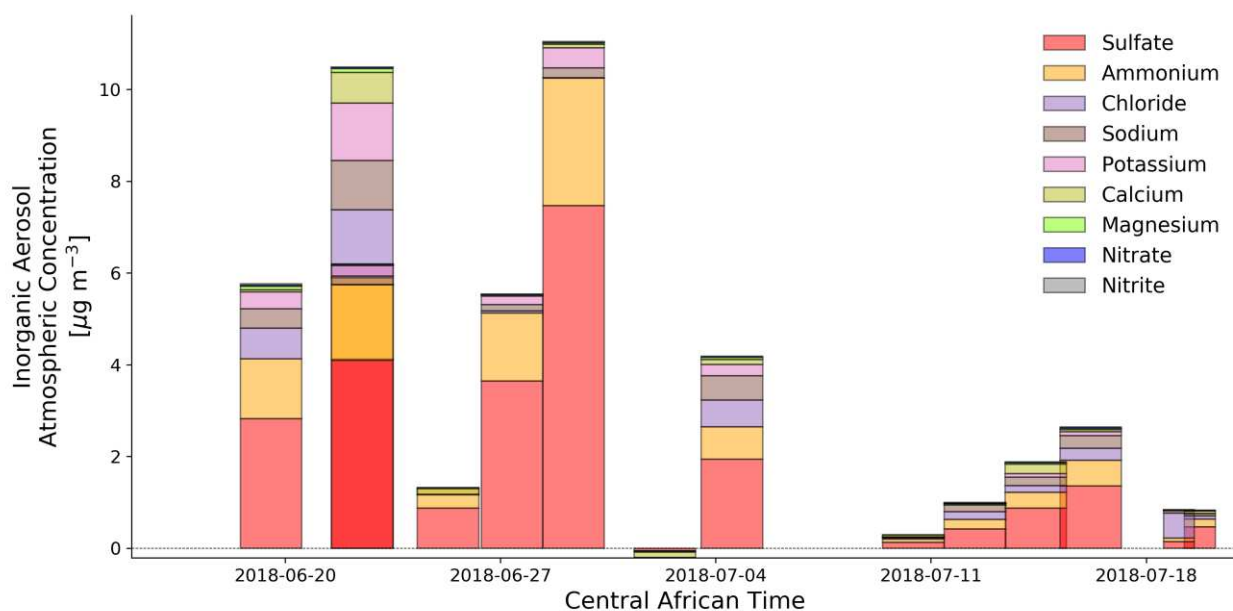


Figure 4.4: Results of ion chromatography characterization of filter samples.

meaning SO_4^{2-} is completely or nearly completely neutralized by NH_4^+ . In addition to the AMOD filter analysis, we conducted time-integrated measurements of gas-phase NH_3 at 3.5 day resolution. However, none of the measurements that we conducted indicated any gas-phase NH_3 above the limit of detection of 3.6 ppb. It seems unlikely that there was enough total ammonia to nearly

completely neutralize SO_4^{2-} each day, yet gas phase NH_3 was never above the 3.6 ppb detection limit. We have identified two potential artifacts of the filter analysis that may be a reason for SO_4^{2-} but NH_3 below its detection limit. (1) The AMOD filter system has no secondary filter or denuder system to account for evaporation of semivolatile species such as ammonium nitrate or semivolatile organic aerosol, that may have previously deposited on the filter in the particle phase (Hering and Cass, 1999); we see no evidence of nitrate in our filters, but this may be due to off-gassing of ammonium nitrate during or after the measurement period. Given that sulfate was fully neutralized, it is possible that ammonium nitrate formed if enough nitric acid was present. If ammonium nitrate was present and was ammonia limited (e.g. excess nitric acid relative to ammonia), ammonia equilibrium vapor pressures could have been orders of magnitude lower than the 3.6 ppb ammonia detection limit as verified by E-AIM (<http://www.aim.env.uea.ac.uk/aim/aim.php>; Wexler and Clegg, 2002). The presence of ammonia-limited ammonium nitrate could explain the neutralized sulfate but ammonia below the detection limit throughout the measurement period; however, we do not have nitric acid measurements in the region to verify. (2) Ammonium may actually have been too low to neutralize sulfate, which would cause ammonia concentrations to be below detection limits, but the filter was exposed to ammonia at some point between the measurement period and analysis (potentially due to offgassing of ammonia from the 3D-printed AMOD chassis). It is possible that total ammonia concentrations in the region are in fact low; while livestock is an important part of the Botswana economy (Rennie et al., 1977), and livestock production is a known source of NH_3 to the environment, the free-range manner in which Botswana cattle are raised are not conducive to the massive ammonia emissions observed near more industrialized cattle operations in the United State (Shonkwiler and Ham, 2018), Australia (Shen et al., 2016), Canada (Hristov et al., 2011;

McGinn et al., 2016) and Europe (Sutton et al., 1998; Webb et al., 2005). In short, due to the low-cost nature of the measurement system, there are many potential sources of error in the measurement of various inorganic semi-volatile aerosol constituents. However, we expect the quantification of sulfate and other non-volatile species (e.g. sodium, chloride, potassium) to be more robust.

In addition to the IC analysis, we conducted x-ray diffraction (XRD) analysis of the filters to identify the metallic species present on the aerosol; the results of the XRD analysis are shown in Figure 4.5. Many of the atomic species detectable by the XRF analysis are also present in ions detected by IC. If the IC ions dominate the form of the XRF atom (e.g., low amounts of organic sulfur), the XRD and IC analysis may agree. For example, the mass of sulfur atoms obtained via XRD agrees well with the mass of ionic sulfate, as determined via the IC. Likewise, there is agreement for Cl and Na species from the two methods. However, the XRD also allows us to see the quantity of silicon and iron in the aerosol, which are tracers for dust in this region. Based on

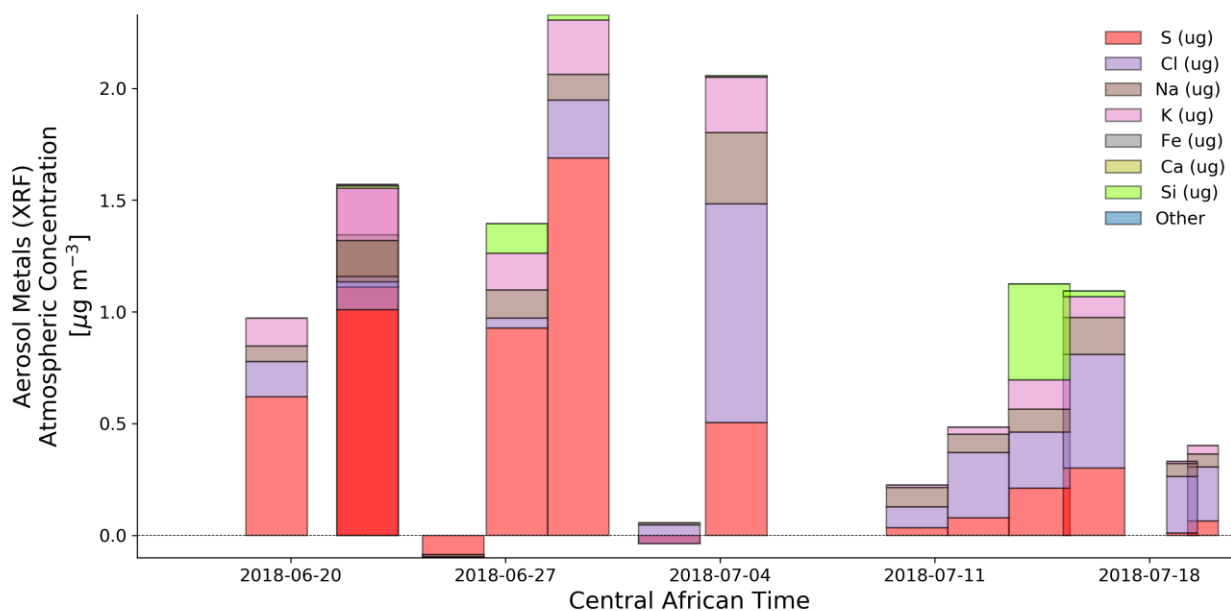


Figure 4.5: X-Ray Fluorescence analysis results from filter samples; colors for important chemical elements are colored corresponding to the IC results in Figure 4.4.

the results in Figure 4.5, the dust in this region is not important for PM_{2.5} particles.. However, this does not preclude that suspended dust is present in coarse particles, and dust is known to be important in this region for visibility (Wiston, 2017).

4.3.3 Temporal Variability

In addition to the filter samples, we use the Plantower real-time PM_{2.5} measurement, along with the MicroAeth black carbon measurements to investigate the diurnal variability in aerosol at the BIUST measurement site. We plot the Plantower data for the entire time period in Figure 4.6a with the black carbon concentrations using a different scale on the second Y axis. In Figure 4.6a, we see that the concentrations for total PM_{2.5} were much higher during the first half of the time period, and comparatively lower during the second half, which is corroborated by the filter-based measurements as described above. There appears to be a difference in black carbon concentrations, but it is much less pronounced than the difference in total PM_{2.5}. We will revisit this difference between the first and second halves of the measurement period shortly.

In Figure 4.6b, we show only the first half of the measurement period, when concentrations were elevated. The total PM_{2.5} concentrations are consistently the highest on the late evening or early morning, peaking between 20 and 40 $\mu\text{g m}^{-3}$ depending on the day. Concentrations are lowest during the middle afternoon, typically around 6 $\mu\text{g m}^{-3}$. Such diurnal cycles in aerosol pollution are not uncommon and can be driven by several different mechanisms: (1) diurnal variability in the sources of aerosols (e.g. human activity or photo-oxidation), (2) variability in transport (i.e. prevailing wind patterns produce effective transport from a point source during certain times of day) or (3) changes in boundary layer height impacting dilution of relatively constant local

emissions. All three mechanisms are important during the more-polluted first half of our measurement period.

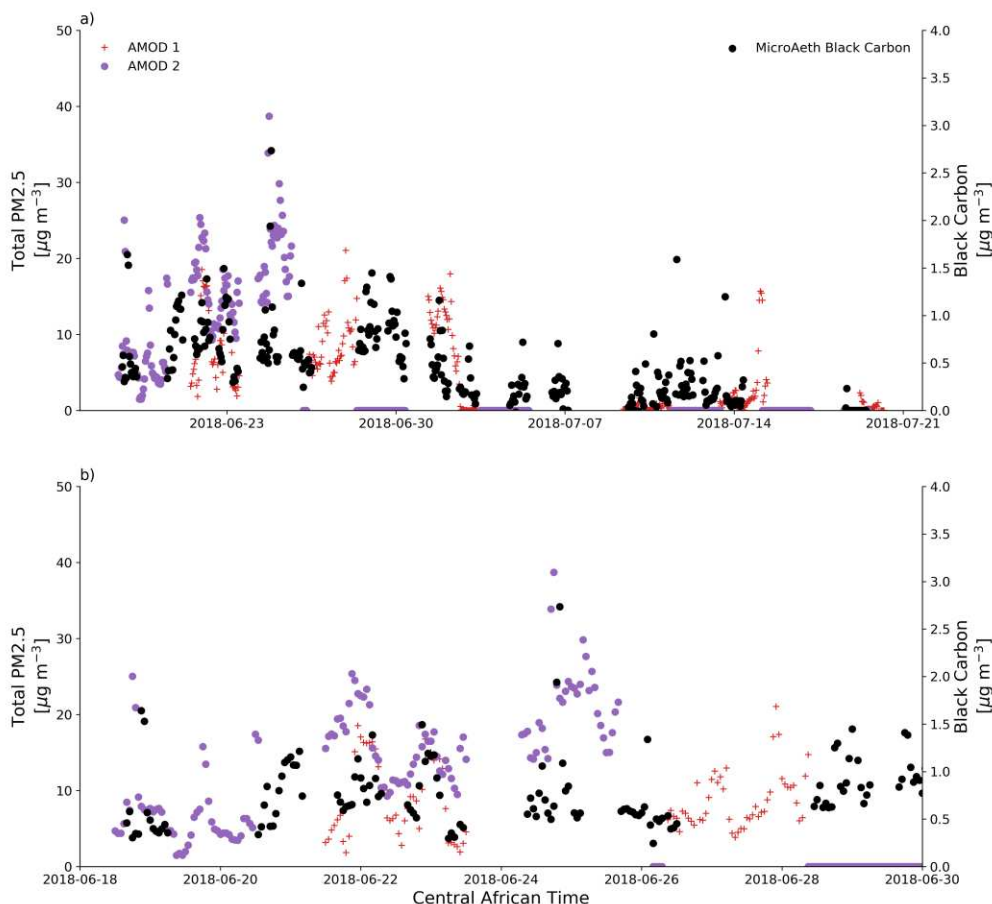


Figure 4.6: Time series of plantower $PM_{2.5}$ and black carbon (a) for the entire time period and (b) zoomed in on the first half of the time period, where a regular diurnal cycle is present.

First, human activity has a known diurnal cycle that has been observed to impact air quality (McDonald et al., 2018). An important source of $PM_{2.5}$ in this region is domestic SFU for cooking and heating. Most SFU occurs overnight to provide heat during the relatively cold nighttime during winter, as well as for cooking, and this was observed during the measurement period. Black carbon, which is a tracer for combustion, exhibits the same diurnal variability as the total $PM_{2.5}$, suggesting

that domestic SFU is the dominant source of combustion-PM_{2.5} in this region. The other major source of black carbon is from diesel vehicles on the A1 highway. However, if this was the dominant source, emissions would peak during times of heavy traffic (the diurnal pattern of traffic in Botswana is not trivial to estimate but likely is lowest overnight). This would not necessarily lead to highest concentrations in the middle of the day, due to differences in boundary layer height and transport; however, the peak in concentrations we observed was well after the vehicle traffic slows down for the night, supporting the hypothesis that SFU is the dominant combustion-aerosol source for this site.

Due to the spatial arrangement of anthropogenic sources of PM_{2.5} relative to our measurement position, wind direction is likely important for PM_{2.5} concentration. In Figure 4.7, we plot hourly wind measurements from the BIUST campus weather station with temporal subsets as follows: (a) contains the windrose for the entire time period, (b) contains the daytime (7am-7pm) observations during the first half of the measurement campaign, (c) contains the nighttime measurements (7pm-7am) from the first half of the campaign, and (d) and (e) contain the daytime and nighttime measurements from the second half of the measurement period respectively. Throughout the measurement period, the dominant wind direction is from the northeast, and east northeast. Wind speeds are typically higher during the day, and in Figure 4.7c (first half, nighttime), there are a larger number of hours with southwesterly winds, though most of these measurements are associated with low wind speeds (i.e. stagnant conditions). The wind direction does not appear to follow a diurnal cycle. The closest potentially important point source near the measurement site is the coal power station located to the west-northwest as a source of sulfate for the region. The wind data show that during this observation period, the wind would have rarely transported power plant emissions to our measurement site. Given the relatively slow rate by which SO₂ is converted

to sulfate in the atmosphere (in the absence of clouds), sulfate is typically a regional-scale pollutant, and does not typically exhibit diurnal variability. Differences in wind behavior do impact sulfate concentrations in this study on longer timescales.

Finally, the diurnal cycle in boundary layer height is likely a key driver in $PM_{2.5}$ and black carbon concentrations at the surface. Due to the warm days with high insolation, the high sensible

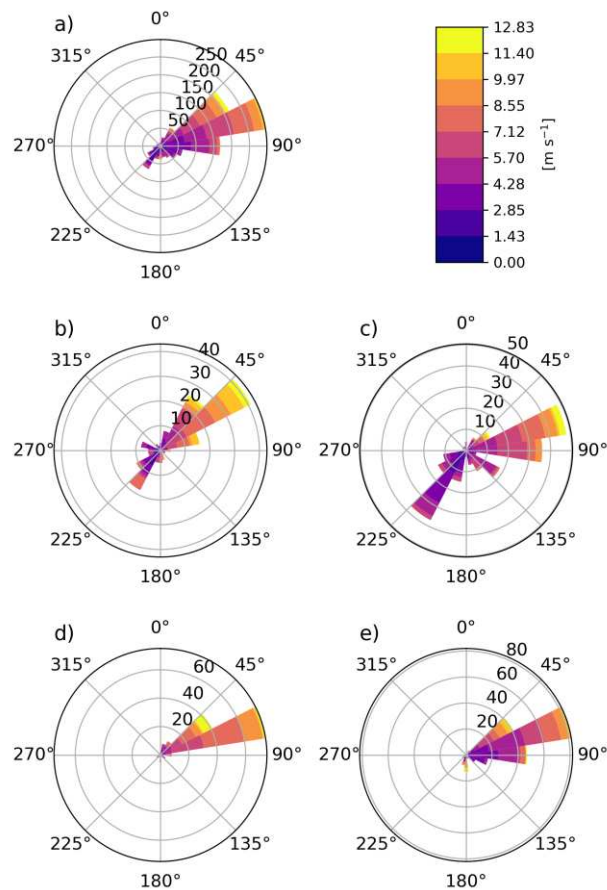


Figure 4.7: Windroses: (a) total time period; (b) first half, day; (c) first half, night; (d) second half day; (e) second half, night.

heat flux from the surface can produce a high boundary layer; likewise, rapid radiative cooling due to the lack of water vapor in the atmosphere can produce cold temperatures and a much shallower boundary layer overnight. The change in boundary layer height impacts the effective volume of air that emissions are diluted into, and for an unchanging emission rate, concentrations increase

for a shallow boundary layer. The boundary layer height typically maximizes mid-afternoon when the sensible heat flux is highest, and minimizes at sunrise when the surface radiative cooling is fastest. The maximum and minimum $\text{PM}_{2.5}$ concentrations occur early relative to the expected maxima and minima of the boundary layer height, suggesting that there are other factors (such as timing of human behavior and the associated emissions) modulating the effect of boundary layer height. With measurements of boundary layer height, we could constrain the emission flux and timing, which would help to better account for the role local combustion sources are impacting the $\text{PM}_{2.5}$ concentration as opposed to advection of regional-scale emissions or upwind point sources. Because boundary layer height depends on surface fluxes as well as larger-scale meteorological conditions, it can be challenging to accurately estimate.

In addition to the diurnal cycle in $\text{PM}_{2.5}$ concentrations, there is a big difference in concentrations between the first and second half of the time period. Concentrations are much larger during the first half of the time period (two-week average concentration of $14.0 \mu\text{g m}^{-3}$) as compared to the second (two-week average concentration $6.5 \mu\text{g m}^{-3}$). From Figure 4.3, we see that there is no obvious change in aerosol composition during the two time periods. In Figure 4.6a, we see that despite the lower concentrations, there is still a diurnal profile associated with black carbon, but the daytime concentrations are close to zero and the overnight concentrations are much lower than during the first half of the measurement period. There was no decrease in overnight temperatures, during the second half of the time period, and consequently there is no reason to believe that there was a systematic change in residential SFU use during this time period. Furthermore, there were no obvious changes in vehicle traffic or on-campus construction activity near the measurement site between the two time periods, though there is no information to thoroughly test this hypothesis. This suggests that the primary driver behind the concentration

differences are related to transport patterns and ventilation of emissions away from our measurement location associated with the synoptic or local-scale meteorological conditions. In Figure 4.7d-e, we show that the second half of the time period was associated with faster wind speeds with more of an easterly contribution; this difference is especially pronounced during night. The differences in wind speed and direction may account for some of the differences between the two time periods; faster winds overnight prevented nighttime concentrations from building up in the second half of the time period, causing a decrease in the 48-hour average $PM_{2.5}$ concentration. During the first half of the time period, nighttime winds were occasionally weak and from the southwest; this diurnal wind behavior could help explain the nighttime increases in $PM_{2.5}$ seen during the first half of the time period. Conversely, the second half time period has winds almost uniformly from the east, even at night. East of the measurement site is sparsely populated desert vegetation with no obvious local sources of $PM_{2.5}$.

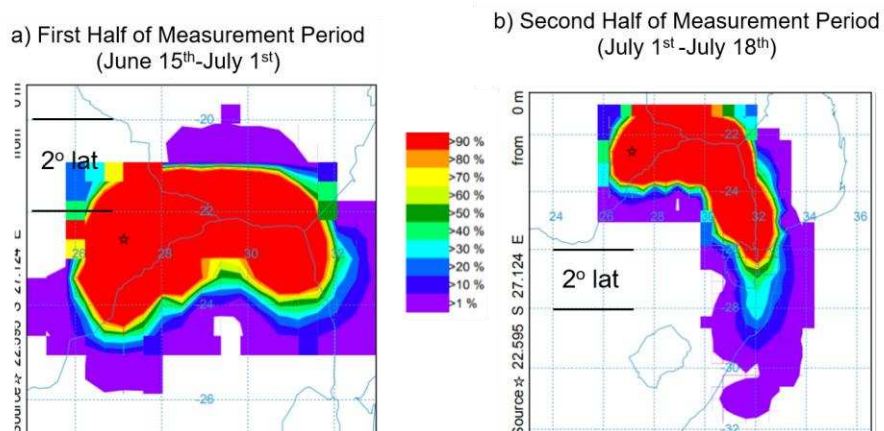


Figure 4.8: HYSPLIT back-trajectories for (a) the first half of the measurement period and (b) the second half of the measurement period (note that (b) spans a much larger area)

During the period between July 3rd and July 8th during the second half, much of southern Africa experienced cold temperatures and anomalous precipitation due to synoptic weather activity (“Cold front expected to hit parts of SA,” 2018; staff, 2018); it is possible that during the first half of the measurement period, regional stagnation allowed local pollution to build up in Palapye. The

cold front passage removed pollution by precipitation and allowed cleaner air to mix into this region. In Figure 4.8, we plot 24-hour HYSPLIT back-trajectories for the two time-periods (8a shows the first half of the measurement period, 8b shows the second half, note the different spatial scales of the two figures). In Figure 4.8a, we see that most of the trajectories originate in a very comparatively small spatial area, while in Figure 4.8b, many of the trajectories originate as far away as South Africa. While the trajectories tend to originate to the east of the measurement site in both cases, the trajectories travel over twice as far in 24 hours during the second half. This faster moving air more effectively dilutes emissions.

Finally, we will discuss the AOD measurement results. In Figure 4.9, we show the AMOD AOD observations during our measurement period plotted alongside MODIS observations interpolated to our measurement site, as well as an average of both overpasses over all pixels within 100 km of the measurement site (labelled as “smoothed” in the figure legend), composited according to the methodology in Lassman et al., (2017). First, the AOD observations from all platforms are low relative to a more polluted parts of the world, with the highest AODs in this period being less than 0.3. The AMOD AOD generally higher than MODIS during the entire measurement period. There are two likely explanations for this: first, AMOD measurements were not performed exactly at the Terra or Aqua overpass times, so the difference may be due to temporal offset between the measurement times; second, the MODIS AOD product has not been thoroughly evaluated for this part of the world. The MODIS AOD retrieval can produce inaccurate results over certain surface types, such as highly reflective desert surfaces. The MODIS AOD product uses surface-based AOD measurements, such as the AERONET network to calibrate the AOD retrieval in different locations with varying surface properties, and for different atmospheric conditions. However, there are few AERONET observations in southern Africa; only two sites

have data available with a data record longer than two years, and both of these sites are over 600 km away on different land surface types. Therefore, MODIS retrievals for this region may be biased low relative to the true atmospheric loading of aerosols. While the AMOD has been shown to accurately compare to MODIS and AERONET data, there are several reasons the AMOD may be biased high, including calibration errors. Longer term measurements and intercomparisons to other sun photometers will help to explain the discrepancy between the AMOD and MODIS AOD retrievals. The primary purpose of this field experiment was to establish a long-term data record of surface-based AOD using a different low-cost sun photometer design, data from which will be included in a subsequent study; these data will present a good opportunity to evaluate the AMOD AOD measurements against another low-cost surface-based technique.

Despite the difference in absolute magnitude for the AOD measurements, the AMOD AOD and MODIS AOD both show the same qualitative result; the AOD is elevated during the first half of the measurement period relative to the second half, which is consistent with the elevated surface concentrations of $PM_{2.5}$ during this period. However, the single-point MODIS observations exhibit a fair amount of day-to-day variability which is unsurprising, given the signal-to-noise ratio inherent to values for AOD around 0.1 over land. In addition to the single-location MODIS AOD, we overlay the average MODIS AOD over a larger spatial area, including all observations in a 50 km radius. In addition to being smoother, the spatial averaging shows a more pronounced increase in AOD during the first half of the measurement period. The spatial averaging helps to reduce the noise in the AOD retrieval, but if the increase in $PM_{2.5}$ were local to Palapye, then it would also wash out the local increases in $PM_{2.5}$. This is not what is observed, as the spatially smoothed MODIS AOD retrieval shows a elevated AOD during the period of elevated surface concentrations. Taken together with the results from the HYSPLIT back-trajectories shown in Figure 4.8, this

suggests that the increase in $PM_{2.5}$ is larger in scale than a local change in emissions near our measurement site in Palapye. Our hypothesis is that this difference between the first and second halves was due to a regional-scale stagnation event during the first half, which was ultimately abated by the passage of a cold front during the first week of July.

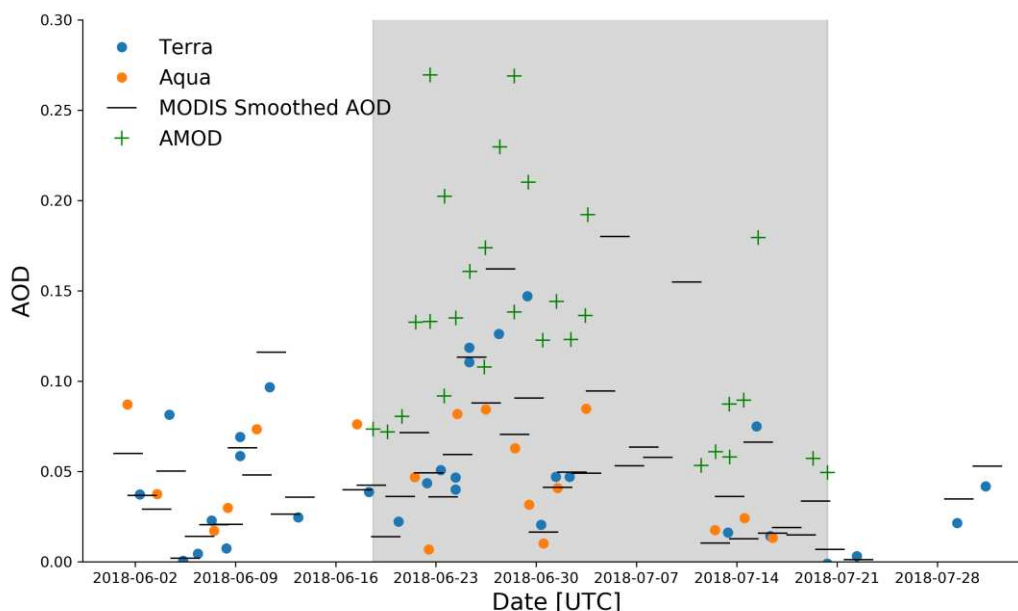


Figure 4.9: MODIS AOD retrieval from Terra (blue) and Aqua (orange) overpasses for Palapye (points) as well as the surrounding 100km average (black), with AMOD AOD overlaid (green crosses). The shaded gray area refers to the duration of the measurement campaign.

4.4 Conclusions

In this study, we share results from a serendipitous measurement campaign coinciding with an NSF-IRES field research study at BIUST in Palapye, Botswana. We used low-cost AMOD measurement systems that are capable of collecting $PM_{2.5}$ samples on teflon filters, along with surface-based AOD, and real-time $PM_{2.5}$ concentrations, all in a portable, low-cost system. In addition, we used Radiello passive NH_3 gas-phase measurements with time-integrated

observations over 3.5 days, and a MicroAeth Aethelometer to measure real-time black carbon concentrations. Using these three low-cost instruments for a measurement period of 5 weeks, we were able to make some observations about the concentration and composition of PM_{2.5} on the BIUST campus. According to the more robust filter-based observations, the average PM_{2.5} concentrations during our measurement period were 9.4 μg m⁻³, which is less than the WHO-recommended annual limit of 10 μg m⁻³ and very close to estimate derived from satellite and model data used by the GBD of 9.1 μg m⁻³ (Brauer et al., 2015). From chemical analysis of the filters, we found that the most important constituent of the particle phase is the inorganic aerosol, which is composed mostly of ammonium sulfate (35% by mass, on average). Potential artifacts in the filters limit our knowledge of ammonium and nitrate. The importance of sulfate is not a surprise, given the number of large coal power plants upwind of the site. The proximity to a coal power plant, and the fact that coal power plants can be important sources of sulfate aerosol to the atmosphere. In addition to inorganic sulfate, a sizeable fraction of the aerosol is composed of carbonaceous species, such as water-soluble organic carbon (12% by mass on average) or black carbon (18% by mass on average); this is also unsurprising, given the prevalence of solid fuel combustion in this region and a nearby major highway. We also determined that dust was not a major component of the PM_{2.5} mixture. Finally, an ~35% of the aerosol mass on average was not speciated by any of our analytical techniques. By elimination, we believe that an important fraction of this is likely insoluble organic aerosol; solid-fuel combustion is a source of carbonaceous aerosol, but usually requires time in the atmosphere to age and become soluble in water. Because our extraction of the AMOD filters used water as a solvent, we are unable to test for the presence of insoluble carbonaceous compounds; this is a major shortcoming of our experimental approach.

In addition to the time-integrated filters, we also were able to obtain real-time measurements of $PM_{2.5}$ from the AMOD Planttower sensors and black carbon from the Aethlabs MicroAeth. Both of these measurement principles require assumptions about the optical properties, morphology, and size of the respective particles/substances that are being measured, and so these may not produce unbiased measurements of concentration, for either BC or $PM_{2.5}$. However, when properly interpreted, such measurements provide us with qualitative information about the diurnal variability in BC and $PM_{2.5}$. From these measurements, we see that the BC and $PM_{2.5}$ are correlated on the diurnal timescale, and that both species exhibit similar diurnal cycles with concentrations maximizing overnight. Based on our observations, our analysis of wind speed and direction measurements from the BIUST campus, and the types of sources that are present, we attribute the diurnal cycle in BC and $PM_{2.5}$ to residential SFU for cooking and heating and changes in boundary layer height likely play a role as well.

Next, we compared the AMOD AOD measurements with MODIS AOD retrievals. The primary purpose of the study was to establish a longer-term data record of surface-based AOD measurements using a different low-cost design. Those measurements will be shared in the future and are beyond the scope of this 5-week case study. However, they reflect the need for surface-based AOD measurements to help calibrate the MODIS and other satellite-based AOD retrievals while accounting for local differences in surface reflectance. Finally, it is important to accept the limitations of our measurements. The measurements were performed using low-cost instruments, and the data record is short. However, given the lack of available data for this region, we demonstrated how such low-cost measurement campaigns can be used to advance our knowledge of the type, and severity, of aerosol pollution and sources in a region where no other measurement data are available

REFERENCES

- Bond, T.C., Streets, D.G., Yarber, K.F., Nelson, S.M., Woo, J.-H., Klimont, Z., 2004. A technology-based global inventory of black and organic carbon emissions from combustion. *Journal of Geophysical Research: Atmospheres* 109. <https://doi.org/10.1029/2003JD003697>
- Bonjour, S., Adair-Rohani, H., Wolf, J., Bruce, N.G., Mehta, S., Prüss-Ustün, A., Lahiff, M., Rehfuss, E.A., Mishra, V., Smith, K.R., 2013. Solid Fuel Use for Household Cooking: Country and Regional Estimates for 1980–2010. *Environ Health Perspect* 121, 784–790. <https://doi.org/10.1289/ehp.1205987>
- Brauer, M., Amann, M., Burnett, R.T., Cohen, A., Dentener, F., Ezzati, M., Henderson, S.B., Krzyzanowski, M., Martin, R.V., Van Dingenen, R., van Donkelaar, A., Thurston, G.D., 2012. Exposure Assessment for Estimation of the Global Burden of Disease Attributable to Outdoor Air Pollution. *Environmental Science & Technology* 46, 652–660. <https://doi.org/10.1021/es2025752>
- Bulot, F.M.J., Johnston, S.J., Basford, P.J., Easton, N.H.C., Apetroaie-Cristea, M., Foster, G.L., Morris, A.K.R., Cox, S.J., Loxham, M., 2019. Long-term field comparison of multiple low-cost particulate matter sensors in an outdoor urban environment. *Scientific Reports* 9, 1–13. <https://doi.org/10.1038/s41598-019-43716-3>
- Clements, A.L., Griswold, W.G., Rs, A., Johnston, J.E., Herting, M.M., Thorson, J., Collier-Oxandale, A., Hannigan, M., 2017. Low-Cost Air Quality Monitoring Tools: From Research to Practice (A Workshop Summary). *Sensors* 17, 2478. <https://doi.org/10.3390/s17112478>

- Coffey, E.R., Muvandimwe, D., Hagar, Y., Wiedinmyer, C., Kanyomse, E., Piedrahita, R., Dickinson, K.L., Oduro, A., Hannigan, M.P., 2017. New Emission Factors and Efficiencies from in-Field Measurements of Traditional and Improved Cookstoves and Their Potential Implications. *Environ. Sci. Technol.* 51, 12508–12517. <https://doi.org/10.1021/acs.est.7b02436>
- Cold front expected to hit parts of SA [WWW Document], 2018. . SABC News - Breaking news, special reports, world, business, sport coverage of all South African current events. Africa's news leader. URL <http://www.sabcnews.com/sabcnews/cold-front-expected-to-hit-parts-of-sa/> (accessed 11.20.19).
- Dockery, D.W., Pope, C.A., Xu, X., Spengler, J.D., Ware, J.H., Fay, M.E., Ferris, B.G.Jr., Speizer, F.E., 1993. An Association between Air Pollution and Mortality in Six U.S. Cities. *New England Journal of Medicine* 329, 1753–1759. <https://doi.org/10.1056/NEJM199312093292401>
- Eilerman, S.J., Peischl, J., Neuman, J.A., Ryerson, T.B., Aikin, K.C., Holloway, M.W., Zondlo, M.A., Golston, L.M., Pan, D., Floerchinger, C., Herndon, S., 2016. Characterization of Ammonia, Methane, and Nitrous Oxide Emissions from Concentrated Animal Feeding Operations in Northeastern Colorado. *Environ. Sci. Technol.* 50, 10885–10893. <https://doi.org/10.1021/acs.est.6b02851>
- Ford, B., Heald, C.L., 2016. Exploring the uncertainty associated with satellite-based estimates of premature mortality due to exposure to fine particulate matter. *Atmos. Chem. Phys.* 16, 3499–3523. <https://doi.org/10.5194/acp-16-3499-2016>
- Ford, B., Pierce, J.R., Wendt, E., Long, M., Jathar, S., Mehaffy, J., Tryner, J., Quinn, C., Zyl, L. van, L'Orange, C., Miller-Lionberg, D., Volckens, J., 2019. A low-cost monitor for

measurement of fine particulate matter and aerosol optical depth – Part 2: Citizen science pilot campaign in northern Colorado. *Atmospheric Measurement Techniques Discussions* 1–20. <https://doi.org/10.5194/amt-2019-109>

Forouzanfar, M.H., Alexander, L., Anderson, H.R., Bachman, V.F., Biryukov, S., Brauer, M., Burnett, R., Casey, D., Coates, M.M., Cohen, A., Delwiche, K., Estep, K., Frostad, J.J., Astha, K.C., Kyu, H.H., Moradi-Lakeh, M., Ng, M., Slepak, E.L., Thomas, B.A., Wagner, J., Aasvang, G.M., Abbafati, C., Abbasoglu Ozgoren, A., Abd-Allah, F., Abera, S.F., Aboyans, V., Abraham, B., Abraham, J.P., Abubakar, I., Abu-Rmeileh, N.M.E., Aburto, T.C., Achoki, T., Adelekan, A., Adofo, K., Adou, A.K., Adsuar, J.C., Afshin, A., Agardh, E.E., Al Khabouri, M.J., Al Lami, F.H., Alam, S.S., Alasfoor, D., Albittar, M.I., Alegretti, M.A., Aleman, A.V., Alemu, Z.A., Alfonso-Cristancho, R., Alhabib, S., Ali, R., Ali, M.K., Alla, F., Allebeck, P., Allen, P.J., Alsharif, U., Alvarez, E., Alvis-Guzman, N., Amankwaa, A.A., Amare, A.T., Ameh, E.A., Ameli, O., Amini, H., Ammar, W., Anderson, B.O., Antonio, C.A.T., Anwari, P., Argeseanu Cunningham, S., Arnlöv, J., Arsenijevic, V.S.A., Artaman, A., Asghar, R.J., Assadi, R., Atkins, L.S., Atkinson, C., Avila, M.A., Awuah, B., Badawi, A., Bahit, M.C., Bakfalouni, T., Balakrishnan, K., Balalla, S., Balu, R.K., Banerjee, A., Barber, R.M., Barker-Collo, S.L., Barquera, S., Barregard, L., Barrero, L.H., Barrientos-Gutierrez, T., Basto-Abreu, A.C., Basu, A., Basu, S., Basulaiman, M.O., Batis Ruvalcaba, C., Beardsley, J., Bedi, N., Bekele, T., Bell, M.L., Benjet, C., Bennett, D.A., Benzian, H., Bernabé, E., Beyene, T.J., Bhala, N., Bhalla, A., Bhutta, Z.A., Bikbov, B., Bin Abdulhak, A.A., Blore, J.D., Blyth, F.M., Bohensky, M.A., Bora Başara, B., Borges, G., Bornstein, N.M., Bose, D., Boufous, S., Bourne, R.R., Brainin, M., Brazinova, A., Breitborde, N.J., Brenner, H., Briggs, A.D.M., Broday, D.M., Brooks, P.M., Bruce, N.G.,

Brugha, T.S., Brunekreef, B., Buchbinder, R., Bui, L.N., Bukhman, G., Bulloch, A.G., Burch, M., Burney, P.G.J., Campos-Nonato, I.R., Campuzano, J.C., Cantoral, A.J., Caravanos, J., Cárdenas, R., Cardis, E., Carpenter, D.O., Caso, V., Castañeda-Orjuela, C.A., Castro, R.E., Catalá-López, F., Cavalleri, F., Çavlin, A., Chadha, V.K., Chang, J.-C., Charlson, F.J., Chen, H., Chen, W., Chen, Z., Chiang, P.P., Chimed-Ochir, O., Chowdhury, R., Christophi, C.A., Chuang, T.-W., Chugh, S.S., Cirillo, M., Claßen, T.K.D., Colistro, V., Colomar, M., Colquhoun, S.M., Contreras, A.G., Cooper, C., Cooperrider, K., Cooper, L.T., Coresh, J., Courville, K.J., Criqui, M.H., Cuevas-Nasu, L., Damsere-Derry, J., Danawi, H., Dandona, L., Dandona, R., Dargan, P.I., Davis, A., Davitoiu, D.V., Dayama, A., de Castro, E.F., De la Cruz-Góngora, V., De Leo, D., de Lima, G., Degenhardt, L., del Pozo-Cruz, B., Dellavalle, R.P., Deribe, K., Derrett, S., Des Jarlais, D.C., Dessalegn, M., deVeber, G.A., Devries, K.M., Dharmaratne, S.D., Dherani, M.K., Dicker, D., Ding, E.L., Dokova, K., Dorsey, E.R., Driscoll, T.R., Duan, L., Durrani, A.M., Ebel, B.E., Ellenbogen, R.G., Elshrek, Y.M., Endres, M., Ermakov, S.P., Erskine, H.E., Eshrati, B., Esteghamati, A., Fahimi, S., Faraon, E.J.A., Farzadfar, F., Fay, D.F.J., Feigin, V.L., Feigl, A.B., Fereshtehnejad, S.-M., Ferrari, A.J., Ferri, C.P., Flaxman, A.D., Fleming, T.D., Foigt, N., Foreman, K.J., Paleo, U.F., Franklin, R.C., Gabbe, B., Gaffikin, L., Gakidou, E., Gamkrelidze, A., Gankpé, F.G., Gansevoort, R.T., García-Guerra, F.A., Gasana, E., Geleijnse, J.M., Gessner, B.D., Gething, P., Gibney, K.B., Gillum, R.F., Ginawi, I.A.M., Giroud, M., Giussani, G., Goenka, S., Goginashvili, K., Gomez Dantes, H., Gona, P., Gonzalez de Cosio, T., González-Castell, D., Gotay, C.C., Goto, A., Gouda, H.N., Guerrant, R.L., Gugnani, H.C., Guillemin, F., Gunnell, D., Gupta, Rahul, Gupta, Rajeev, Gutiérrez, R.A., Hafezi-Nejad, N., Hagan, H., Hagstromer, M., Halasa, Y.A., Hamadeh, R.R.,

Hammami, M., Hankey, G.J., Hao, Y., Harb, H.L., Haregu, T.N., Haro, J.M., Havmoeller, R., Hay, S.I., Hedayati, M.T., Heredia-Pi, I.B., Hernandez, L., Heuton, K.R., Heydarpour, P., Hajar, M., Hoek, H.W., Hoffman, H.J., Hornberger, J.C., Hosgood, H.D., Hoy, D.G., Hsairi, M., Hu, G., Hu, H., Huang, C., Huang, J.J., Hubbell, B.J., Huiart, L., Husseini, A., Iannarone, M.L., Iburg, K.M., Idrisov, B.T., Ikeda, N., Innos, K., Inoue, M., Islami, F., Ismayilova, S., Jacobsen, K.H., Jansen, H.A., Jarvis, D.L., Jassal, S.K., Jauregui, A., Jayaraman, S., Jeemon, P., Jensen, P.N., Jha, V., Jiang, F., Jiang, G., Jiang, Y., Jonas, J.B., Juel, K., Kan, H., Kany Roseline, S.S., Karam, N.E., Karch, A., Karema, C.K., Karthikeyan, G., Kaul, A., Kawakami, N., Kazi, D.S., Kemp, A.H., Kengne, A.P., Keren, A., Khader, Y.S., Khalifa, S.E.A.H., Khan, E.A., Khang, Y.-H., Khatibzadeh, S., Khonelidze, I., Kieling, C., Kim, D., Kim, S., Kim, Y., Kimokoti, R.W., Kinfu, Y., Kinge, J.M., Kissela, B.M., Kivipelto, M., Knibbs, L.D., Knudsen, A.K., Kokubo, Y., Kose, M.R., Kosen, S., Kraemer, A., Kravchenko, M., Krishnaswami, S., Kromhout, H., Ku, T., Kuate Defo, B., Kucuk Bicer, B., Kuipers, E.J., Kulkarni, C., Kulkarni, V.S., Kumar, G.A., Kwan, G.F., Lai, T., Lakshmana Balaji, A., Lalloo, R., Lallukka, T., Lam, H., Lan, Q., Lansingh, V.C., Larson, H.J., Larsson, A., Laryea, D.O., Lavados, P.M., Lawrynowicz, A.E., Leasher, J.L., Lee, J.-T., Leigh, J., Leung, R., Levi, M., Li, Yichong, Li, Yongmei, Liang, J., Liang, X., Lim, S.S., Lindsay, M.P., Lipshultz, S.E., Liu, S., Liu, Y., Lloyd, B.K., Logroscino, G., London, S.J., Lopez, N., Lortet-Tieulent, J., Lotufo, P.A., Lozano, R., Lunevicius, R., Ma, J., Ma, S., Machado, V.M.P., MacIntyre, M.F., Magis-Rodriguez, C., Mahdi, A.A., Majdan, M., Malekzadeh, R., Mangalam, S., Mapoma, C.C., Marape, M., Marcenes, W., Margolis, D.J., Margono, C., Marks, G.B., Martin, R.V., Marzan, M.B., Mashal, M.T., Masiye, F., Mason-Jones, A.J., Matsushita, K., Matzopoulos, R., Mayosi, B.M., Mazorodze, T.T.,

McKay, A.C., McKee, M., McLain, A., Meaney, P.A., Medina, C., Mehndiratta, M.M., Mejia-Rodriguez, F., Mekonnen, W., Melaku, Y.A., Meltzer, M., Memish, Z.A., Mendoza, W., Mensah, G.A., Meretoja, A., Mhimbira, F.A., Micha, R., Miller, T.R., Mills, E.J., Misganaw, A., Mishra, S., Mohamed Ibrahim, N., Mohammad, K.A., Mokdad, A.H., Mola, G.L., Monasta, L., Montañez Hernandez, J.C., Montico, M., Moore, A.R., Morawska, L., Mori, R., Moschandreas, J., Moturi, W.N., Mozaffarian, D., Mueller, U.O., Mukaigawara, M., Mullany, E.C., Murthy, K.S., Naghavi, M., Nahas, Z., Naheed, A., Naidoo, K.S., Naldi, L., Nand, D., Nangia, V., Narayan, K.M.V., Nash, D., Neal, B., Nejjari, C., Neupane, S.P., Newton, C.R., Ngalesoni, F.N., Ngirabega, J. de D., Nguyen, G., Nguyen, N.T., Nieuwenhuijsen, M.J., Nisar, M.I., Nogueira, J.R., Nolla, J.M., Nolte, S., Norheim, O.F., Norman, R.E., Norrving, B., Nyakarahuka, L., Oh, I.-H., Ohkubo, T., Olusanya, B.O., Omer, S.B., Opio, J.N., Orozco, R., Pagcatipunan, R.S., Pain, A.W., Pandian, J.D., Panelo, C.I.A., Papachristou, C., Park, E.-K., Parry, C.D., Paternina Caicedo, A.J., Patten, S.B., Paul, V.K., Pavlin, B.I., Pearce, N., Pedraza, L.S., Pedroza, A., Pejcin Stokic, L., Pekerikli, A., Pereira, D.M., Perez-Padilla, R., Perez-Ruiz, F., Perico, N., Perry, S.A.L., Pervaiz, A., Pesudovs, K., Peterson, C.B., Petzold, M., Phillips, M.R., Phua, H.P., Plass, D., Poenaru, D., Polanczyk, G.V., Polinder, S., Pond, C.D., Pope, C.A., Pope, D., Popova, S., Pourmalek, F., Powles, J., Prabhakaran, D., Prasad, N.M., Qato, D.M., Quezada, A.D., Quistberg, D.A.A., Racapé, L., Rafay, A., Rahimi, K., Rahimi-Movaghar, V., Rahman, S.U., Raju, M., Rakovac, I., Rana, S.M., Rao, M., Razavi, H., Reddy, K.S., Refaat, A.H., Rehm, J., Remuzzi, G., Ribeiro, A.L., Riccio, P.M., Richardson, L., Riederer, A., Robinson, M., Roca, A., Rodriguez, A., Rojas-Rueda, D., Romieu, I., Ronfani, L., Room, R., Roy, N., Ruhago, G.M., Rushton, L., Sabin, N., Sacco, R.L., Saha, S., Sahathevan, R., Sahraian,

M.A., Salomon, J.A., Salvo, D., Sampson, U.K., Sanabria, J.R., Sanchez, L.M., Sánchez-Pimienta, T.G., Sanchez-Riera, L., Sandar, L., Santos, I.S., Sapkota, A., Satpathy, M., Saunders, J.E., Sawhney, M., Saylan, M.I., Scarborough, P., Schmidt, J.C., Schneider, I.J.C., Schöttker, B., Schwebel, D.C., Scott, J.G., Seedat, S., Sepanlou, S.G., Serdar, B., Servan-Mori, E.E., Shaddick, G., Shahraz, S., Levy, T.S., Shangguan, S., She, J., Sheikhabaei, S., Shibuya, K., Shin, H.H., Shinohara, Y., Shiri, R., Shishani, K., Shiue, I., Sigfusdottir, I.D., Silberberg, D.H., Simard, E.P., Sindi, S., Singh, A., Singh, G.M., Singh, J.A., Skirbekk, V., Sliwa, K., Soljak, M., Soneji, S., Søreide, K., Soshnikov, S., Sposato, L.A., Sreeramareddy, C.T., Stapelberg, N.J.C., Stathopoulou, V., Steckling, N., Stein, D.J., Stein, M.B., Stephens, N., Stöckl, H., Straif, K., Stroumpoulis, K., Sturua, L., Sunguya, B.F., Swaminathan, S., Swaroop, M., Sykes, B.L., Tabb, K.M., Takahashi, K., Talongwa, R.T., Tandon, N., Tanne, D., Tanner, M., Tavakkoli, M., Te Ao, B.J., Teixeira, C.M., Téllez Rojo, M.M., Terkawi, A.S., Texcalac-Sangrador, J.L., Thackway, S.V., Thomson, B., Thorne-Lyman, A.L., Thrift, A.G., Thurston, G.D., Tillmann, T., Tobollik, M., Tonelli, M., Topouzis, F., Towbin, J.A., Toyoshima, H., Traebert, J., Tran, B.X., Trasande, L., Trillini, M., Trujillo, U., Dimbuene, Z.T., Tsilimbaris, M., Tuzcu, E.M., Uchendu, U.S., Ukwaja, K.N., Uzun, S.B., van de Vijver, S., Van Dingenen, R., van Gool, C.H., van Os, J., Varakin, Y.Y., Vasankari, T.J., Vasconcelos, A.M.N., Vavilala, M.S., Veerman, L.J., Velasquez-Melendez, G., Venketasubramanian, N., Vijayakumar, L., Villalpando, S., Violante, F.S., Vlassov, V.V., Vollset, S.E., Wagner, G.R., Waller, S.G., Wallin, M.T., Wan, X., Wang, H., Wang, J., Wang, L., Wang, W., Wang, Y., Warouw, T.S., Watts, C.H., Weichenthal, S., Weiderpass, E., Weintraub, R.G., Werdecker, A., Wessells, K.R., Westerman, R., Whiteford, H.A., Wilkinson, J.D., Williams, H.C., Williams, T.N.,

- Woldeyohannes, S.M., Wolfe, C.D.A., Wong, J.Q., Woolf, A.D., Wright, J.L., Wurtz, B., Xu, G., Yan, L.L., Yang, G., Yano, Y., Ye, P., Yenesew, M., Yentür, G.K., Yip, P., Yonemoto, N., Yoon, S.-J., Younis, M.Z., Younoussi, Z., Yu, C., Zaki, M.E., Zhao, Y., Zheng, Y., Zhou, M., Zhu, J., Zhu, S., Zou, X., Zunt, J.R., Lopez, A.D., Vos, T., Murray, C.J., 2015. Global, regional, and national comparative risk assessment of 79 behavioural, environmental and occupational, and metabolic risks or clusters of risks in 188 countries, 1990-2013: a systematic analysis for the Global Burden of Disease Study 2013. *Lancet* 386, 2287–2323. [https://doi.org/10.1016/S0140-6736\(15\)00128-2](https://doi.org/10.1016/S0140-6736(15)00128-2)
- Hering, S., Cass, G., 1999. The Magnitude of Bias in the Measurement of PM_{2.5} Arising from Volatilization of Particulate Nitrate from Teflon Filters. *Journal of the Air & Waste Management Association* 49, 725–733. <https://doi.org/10.1080/10473289.1999.10463843>
- Hristov, A.N., Hanigan, M., Cole, A., Todd, R., McAllister, T.A., Ndegwa, P.M., Rotz, A., 2011. Review: Ammonia emissions from dairy farms and beef feedlots. *Canadian Journal of Animal Science* 91, 1–35. <https://doi.org/10.1139/CJAS10034>
- Jayarathne, E.R., Verma, T.S., 2001. The impact of biomass burning on the environmental aerosol concentration in Gaborone, Botswana. *Atmospheric Environment* 35, 1821–1828. [https://doi.org/10.1016/S1352-2310\(00\)00561-6](https://doi.org/10.1016/S1352-2310(00)00561-6)
- Jimenez, J.L., Canagaratna, M.R., Donahue, N.M., Prevot, A.S.H., Zhang, Q., Kroll, J.H., DeCarlo, P.F., Allan, J.D., Coe, H., Ng, N.L., Aiken, A.C., Docherty, K.S., Ulbrich, I.M., Grieshop, A.P., Robinson, A.L., Duplissy, J., Smith, J.D., Wilson, K.R., Lanz, V.A., Hueglin, C., Sun, Y.L., Tian, J., Laaksonen, A., Raatikainen, T., Rautiainen, J., Vaattovaara, P., Ehn, M., Kulmala, M., Tomlinson, J.M., Collins, D.R., Cubison, M.J., E, Dunlea, J., Huffman, J.A., Onasch, T.B., Alfarra, M.R., Williams, P.I., Bower, K., Kondo, Y., Schneider, J., Drewnick,

- F., Borrmann, S., Weimer, S., Demerjian, K., Salcedo, D., Cottrell, L., Griffin, R., Takami, A., Miyoshi, T., Hatakeyama, S., Shimono, A., Sun, J.Y., Zhang, Y.M., Dzepina, K., Kimmel, J.R., Sueper, D., Jayne, J.T., Herndon, S.C., Trimborn, A.M., Williams, L.R., Wood, E.C., Middlebrook, A.M., Kolb, C.E., Baltensperger, U., Worsnop, D.R., 2009. Evolution of Organic Aerosols in the Atmosphere. *Science* 326, 1525–1529. <https://doi.org/10.1126/science.1180353>
- Kelly, K.E., Whitaker, J., Petty, A., Widmer, C., Dybwad, A., Sleeth, D., Martin, R., Butterfield, A., 2017. Ambient and laboratory evaluation of a low-cost particulate matter sensor. *Environmental Pollution* 221, 491–500. <https://doi.org/10.1016/j.envpol.2016.12.039>
- Kelly, M.S., Wirth, K.E., Madrigano, J., Feemster, K.A., Cunningham, C.K., Arscott-Mills, T., Boiditswe, S., Shah, S.S., Finalle, R., Steenhoff, A.P., 2015. The effect of exposure to wood smoke on outcomes of childhood pneumonia in Botswana. *Int J Tuberc Lung Dis* 19, 349–355. <https://doi.org/10.5588/ijtld.14.0557>
- Kodros, J.K., Carter, E., Brauer, M., Volckens, J., Bilsback, K.R., L'Orange, C., Johnson, M., Pierce, J.R., 2018. Quantifying the Contribution to Uncertainty in Mortality Attributed to Household, Ambient, and Joint Exposure to PM_{2.5} From Residential Solid Fuel Use. *GeoHealth* 2, 25–39. <https://doi.org/10.1002/2017GH000115>
- Lassman, W., Ford, B., Gan, R.W., Pfister, G., Magzamen, S., Fischer, E.V., Pierce, J.R., 2017. Spatial and temporal estimates of population exposure to wildfire smoke during the Washington state 2012 wildfire season using blended model, satellite, and in situ data. *GeoHealth* 1, 2017GH000049. <https://doi.org/10.1002/2017GH000049>
- Lonsdale, C.R., Stevens, R.G., Brock, C.A., Makar, P.A., Knipping, E.M., Pierce, J.R., 2012. The effect of coal-fired power-plant SO₂ and NO_x control technologies on aerosol nucleation

- in the source plumes. *Atmospheric Chemistry and Physics* 12, 11519–11531.
<https://doi.org/10.5194/acp-12-11519-2012>
- Marais, E.A., Silvern, R.F., Vodonos, A., Dupin, E., Bockarie, A.S., Mickley, L.J., Schwartz, J., 2019. Air Quality and Health Impact of Future Fossil Fuel Use for Electricity Generation and Transport in Africa. *Environ. Sci. Technol.* 53, 13524–13534.
<https://doi.org/10.1021/acs.est.9b04958>
- Marais, E.A., Wiedinmyer, C., 2016. Air Quality Impact of Diffuse and Inefficient Combustion Emissions in Africa (DICE-Africa). *Environ. Sci. Technol.* 50, 10739–10745.
<https://doi.org/10.1021/acs.est.6b02602>
- McDonald, B.C., Gouw, J.A. de, Gilman, J.B., Jathar, S.H., Akherati, A., Cappa, C.D., Jimenez, J.L., Lee-Taylor, J., Hayes, P.L., McKeen, S.A., Cui, Y.Y., Kim, S.-W., Gentner, D.R., Isaacman-VanWertz, G., Goldstein, A.H., Harley, R.A., Frost, G.J., Roberts, J.M., Ryerson, T.B., Trainer, M., 2018. Volatile chemical products emerging as largest petrochemical source of urban organic emissions. *Science* 359, 760–764.
<https://doi.org/10.1126/science.aag0524>
- McGinn, S.M., Janzen, H.H., Coates, T.W., Beauchemin, K.A., Flesch, T.K., 2016. Ammonia Emission from a Beef Cattle Feedlot and Its Local Dry Deposition and Re-Emission. *Journal of Environmental Quality* 45, 1178–1185.
<https://doi.org/10.2134/jeq2016.01.0009>
- Nelson, P.F., Tibbett, A.R., Day, S.J., 2008. Effects of vehicle type and fuel quality on real world toxic emissions from diesel vehicles. *Atmospheric Environment* 42, 5291–5303.
<https://doi.org/10.1016/j.atmosenv.2008.02.049>

- Pope, C.A., 2000. Epidemiology of fine particulate air pollution and human health: biologic mechanisms and who's at risk? *Environ Health Perspect* 108, 713–723.
- Rai, A.C., Kumar, P., Pilla, F., Skouloudis, A.N., Di Sabatino, S., Ratti, C., Yasar, A., Rickerby, D., 2017. End-user perspective of low-cost sensors for outdoor air pollution monitoring. *Science of The Total Environment* 607–608, 691–705. <https://doi.org/10.1016/j.scitotenv.2017.06.266>
- Rennie, T., Light, D., Rutherford, A., Miller, M., Fisher, I., Pratchett, D., Capper, B., Buck, N., Trail, J., 1977. Beef cattle productivity under traditional and improved management in Botswana. *Trop Anim Health Prod* 9, 1–6. <https://doi.org/10.1007/BF02297380>
- Sayahi, T., Butterfield, A., Kelly, K.E., 2019. Long-term field evaluation of the Plantower PMS low-cost particulate matter sensors. *Environmental Pollution* 245, 932–940. <https://doi.org/10.1016/j.envpol.2018.11.065>
- Shen, J., Chen, D., Bai, M., Sun, J., Coates, T., Lam, S.K., Li, Y., 2016. Ammonia deposition in the neighbourhood of an intensive cattle feedlot in Victoria, Australia. *Scientific Reports* 6, srep32793. <https://doi.org/10.1038/srep32793>
- Shonkwiler, K.B., Ham, J.M., 2018. Ammonia emissions from a beef feedlot: Comparison of inverse modeling techniques using long-path and point measurements of fence-line NH₃. *Agricultural and Forest Meteorology, Greenhouse gas and ammonia emissions from livestock production* 258, 29–42. <https://doi.org/10.1016/j.agrformet.2017.10.031>
- Spotted: giraffes in the snow. *The Guardian*. 2018
- Statistics Botswana [WWW Document], 2017. Statistics Botswana. URL <http://www.statsbots.org.bw/> (accessed 5.9.19).

- Sutton, M.A., Milford, C., Dragosits, U., Place, C.J., Singles, R.J., Smith, R.I., Pitcairn, C.E.R., Fowler, D., Hill, J., ApSimon, H.M., Ross, C., Hill, R., Jarvis, S.C., Pain, B.F., Phillips, V.C., Harrison, R., Moss, D., Webb, J., Espenhahn, S.E., Lee, D.S., Hornung, M., Ullyett, J., Bull, K.R., Emmett, B.A., Lowe, J., Wyers, G.P., 1998. Dispersion, deposition and impacts of atmospheric ammonia: quantifying local budgets and spatial variability. *Environmental Pollution, Nitrogen, the Confer-N-s First International Nitrogen Conference 1998* 102, 349–361. [https://doi.org/10.1016/S0269-7491\(98\)80054-7](https://doi.org/10.1016/S0269-7491(98)80054-7)
- Transport and Infrastructure Report 2017 [WWW Document], 2018. . Statistics Botswana. URL <http://www.statsbots.org.bw/transport-and-infrastructure-report-2017> (accessed 11.7.19).
- van Donkelaar, A., Martin, R.V., Levy, R.C., da Silva, A.M., Krzyzanowski, M., Chubarova, N.E., Semutnikova, E., Cohen, A.J., 2011. Satellite-based estimates of ground-level fine particulate matter during extreme events: A case study of the Moscow fires in 2010. *Atmospheric Environment* 45, 6225–6232. <https://doi.org/10.1016/j.atmosenv.2011.07.068>
- Volckens, J., Quinn, C., Leith, D., Mehaffy, J., Henry, C.S., Miller-Lionberg, D., 2017. Development and evaluation of an ultrasonic personal aerosol sampler. *Indoor Air* 27, 409–416. <https://doi.org/10.1111/ina.12318>
- Webb, J., Menzi, H., Pain, B.F., Misselbrook, T.H., Dämmgen, U., Hendriks, H., Döhler, H., 2005. Managing ammonia emissions from livestock production in Europe. *Environmental Pollution, The National Atmospheric Deposition Program (25th Anniversary) and Ammonia Workshop* 135, 399–406. <https://doi.org/10.1016/j.envpol.2004.11.013>
- Wendt, E.A., Quinn, C.W., Miller-Lionberg, D.D., Tryner, J., L'Orange, C., Ford, B., Yalin, A.P., Pierce, J.R., Jathar, S., Volckens, J., 2019. A low-cost monitor for simultaneous

- measurement of fine particulate matter and aerosol optical depth – Part 1: Specifications and testing. *Atmospheric Measurement Techniques* 12, 5431–5441. <https://doi.org/10.5194/amt-12-5431-2019>
- Wexler, A.S., Clegg, S.L., 2002. Atmospheric aerosol models for systems including the ions H⁺, NH₄⁺, Na⁺, SO₄²⁻, NO₃⁻, Cl⁻, Br⁻, and H₂O. *Journal of Geophysical Research: Atmospheres* 107, ACH 14-1-ACH 14-14. <https://doi.org/10.1029/2001JD000451>
- Wiston, M., 2017. Status of Air Pollution in Botswana and Significance to Air Quality and Human Health. *Journal of Health and Pollution* 7, 8–17. <https://doi.org/10.5696/2156-9614-7.15.8>
- Yang, Y., Liao, W., Wang, X., Liu, C., Xie, Q., Gao, Z., Ma, W., He, Y., 2016. Quantification of ammonia emissions from dairy and beef feedlots in the Jing-Jin-Ji district, China. *Agriculture, Ecosystems & Environment* 232, 29–37. <https://doi.org/10.1016/j.agee.2016.07.016>
- Yong, Z., 2016. Digital universal particle concentration sensor PMS5003 series data manual, available at http://www.aqmd.gov/docs/default-source/aq-spec/resources-page/plantower-pms1003-manual_v2-5.pdf?sfvrsn=2.

CHAPTER 5. CONCLUSIONS

5.1 Summary of Chapter 2

In Chapter 1, I coupled OpenFOAM, an open source CFD model in a RANS configuration, to MODDAS, a Lagrangian Stochastic canopy model that includes a multi-level ammonia bidirectional exchange parameterization. In addition to porting MODDAS to a UNIX environment, I updated the model to facilitate running it in a high-performance computing environment. I then used the coupled model framework to simulate ammonia dispersion from a CAFO under neutral atmospheric conditions, and I calculated the ammonia dry deposition near the CAFO using the bidirectional flux model.

I found that the ammonia dry deposition varies depending on the land surface type. While bare soil absorbs very little ammonia, deciduous and coniferous forests removed 50% and 40% of the total CAFO ammonia emissions over 1500 m downwind, respectively. A maize crop, which is frequently grown near CAFOs to provide locally grown feed for the animals, can recapture approximately 30%, while unmanaged grassland recaptures approximately 10%. However, there are few studies to compare these results to. Two studies (Shen et al., 2016; 2018) conducted measurements downwind of a CAFO in Australia and found similar concentrations and deposition rates of ammonia as were estimated by OpenFOAM-MODDAS over a grassland surface. However, they also observed changes in grass and herbaceous cover near the CAFO boundary (ammonia deposition is known to affect soil pH, N_R concentration, and other biological processes in soil and plant canopies). To understand the importance of this on ammonia deposition, I performed simulations while varying the ammonia emission potential parameter over maize to quantify the effect of this parameter on ammonia recapture. Under cold and humid conditions, the emission

potential has little or no effect on ammonia deposition. However, under hot dry conditions, the emission potential has a big impact on the ammonia recapture percentage. In real plant canopies, the emission potential increases as a result of N_R input; therefore, there is likely a saturation effect on plant canopies near CAFOs and their ability to absorb ammonia from the atmosphere.

5.2 Summary of Chapter 3

Next, I used SAM, a LES model, to simulate dispersion downwind of a CAFO of two tracer species (ammonia and methane) to investigate a novel method for measuring ammonia deposition. Unlike OpenFOAM in RANS configuration used in Chapter 1, SAM is turbulence-resolving 4-D atmospheric model driven by reanalysis boundary conditions and latent and sensible heat flux. One of the tracers was implemented with a first-order loss process at the model surface, representing ammonia undergoing dry deposition; the other tracer is chemically inert, representing methane. While I demonstrated in Chapter 1 that the dry deposition of ammonia is a complicated bidirectional process that depends on many environmental conditions, we do not need to model this bidirectional complexity in order to produce “realistic” conditions of turbulent dispersion downwind of an idealized CAFO; therefore, I made the simplifying assumption of a constant deposition velocity.

By analyzing the change in ammonia:methane concentration ratio in the atmosphere, I demonstrate that we can use conservation of mass to calculate the relative fraction of ammonia that undergoes dry deposition. However, by only including the ratio change at the surface, the method is inherently biased high, and overestimates ammonia deposition. It is necessary to account for the vertical gradient in the ammonia: methane concentration ratio. Finally I produced synthetic measurements by sampling the SAM output from simulated instruments mounted from a vehicle

and sUAS. Even complying with FAA regulations for recreational sUAS operation, which limits flight altitude, we are able to quantify the ammonia deposition with a relatively small amount of bias. While ammonia and methane instruments that can fly on sUAS are still in early development, this promises to be a relatively inexpensive approach for quantifying ammonia deposition near CAFOs.

5.3 Summary of Chapter 4

In Chapter 3, I showed results from a measurement study in Palapye, Botswana. Like the Colorado Front Range, Botswana is an arid grassland climate where beef production is an important economic activity outside of the major urban areas. However, Botswana is a developing nation with a much sparser population, and therefore the air quality is likely governed by different types of sources, and different agricultural and livestock practices.. In Chapter 3, I showed that based on 5 weeks of measurements, $PM_{2.5}$ does not exceed the WHO guidelines and is well represented by the Global Burden of Disease study (GBD) estimates of $PM_{2.5}$ in the region. The $PM_{2.5}$ is mostly composed of WSOC, ammonium sulfate, and unspciated material that is likely to be insoluble organic carbon. This suggests that combustion, such as domestic solid fuel use or diesel combustion are important sources in Palapye, while regional sulfate is another important contributor to total $PM_{2.5}$ mass. The concentrations were comparatively higher during the first half of the measurement period, likely due to a regional stagnation event. The real-time $PM_{2.5}$ and black carbon concentrations were highly correlated with a strong diurnal cycle, suggesting that boundary layer depth and diurnal cycles in human activity (i.e., burning solid fuel for heating during the cool night) are the main drivers in day-to-day variability in $PM_{2.5}$ concentrations. However, longer-term studies with more-sophisticated instrument packages, such as a denuder system that can fully

account for ammonium nitrate volatilization from filters, are required to comprehensively assess the longer-term PM_{2.5} trends and behavior, as well as the corresponding public health burden from exposure to air pollution.

5.4 Synthesis and Future Work

One of the major conclusions from Chapter 1 was that the ammonia emission potential (Γ) is a crucial model parameter, to which the ammonia recapture fraction is potentially very sensitive. The degree to which this parameter saturates is a key constraint on the capacity of a plant canopy to recapture CAFO ammonia emissions. One study (Shen et al., 2018) measured changes in total plant nitrogen closer to the CAFO boundary and also observed changes in the total plant cover as well as the relative abundance of herbaceous vs grass land cover. The findings of Shen et al. (2018) are evidence that the plant canopy does respond to excessive inputs of ammonia, and the increases in plant nitrogen suggest that the emission potential does increase. However, beyond constraining bidirectional flux model parameters for this specific scenario, such measurements would help to provide insights on how massive fluxes of ammonia can impact the soil pH and microbial processes, and whether this may affect N₂O emissions as well. This process can be explored mechanistically by coupling OpenFOAM-MODDAS to a plant/soil model to understand how the dynamics of this entire system respond to ammonia input. Alternatively, this could be explored with the existing analytical tools introduced in Chapter 1 as well; by subdividing the deposition domain into segments and separately modelling Γ in response to the calculated ammonia input. By iterating over this procedure and tuning the Γ values in each segment of the model domain, these methods could be used to calculate a refined estimate of the ammonia atmospheric concentration and deposition flux at various distances downwind of the CAFO while taking into account canopy

saturation due to F increases. However, such a model would still require additional measurements to validate its performance.

While I cited several studies that quantify ammonia concentration changes (e.g., Hacker et al., 2016; Miller et al., 2015; Staebler et al., 2009 as a non-exhaustive list), comparatively fewer studies attempted to quantify deposition at various distances downwind; such studies (McGinn et al., 2016; Shen et al., 2018, 2016) have all relied on labor-intensive chemical analysis of soil and plant material, labor-intensive denuder extractions, and dry-deposition models with uncertain parameters. While these approaches are important for estimating deposition, their real strength is the ability to simultaneously tease apart the bidirectional flux model by measuring individual parameters. However, these studies are too labor-intensive to monitor deposition across multiple seasons, meteorological conditions, or time-varying activities on an individual CAFO site, or across multiple CAFO sites with differing surrounding ecosystems. The methodology that I describe in Chapter 2 offers a good alternative. While the initial capital investment of the measurement system is high (ammonia and methane analyzers, mobile laboratory and/or sUAS) and may require a high degree of technical proficiency to operate, the method can be rapidly deployed and only requires a few hours of sampling to conduct the experiment, and pre-developed software to interpret the data. It is true that the technology to build ammonia and methane analyzers that can fly on a sUAS is experimental at this time, but I expect this approach to become significantly easier and less expensive to implement than chemical characterization of soil and plant samples in the future. Therefore, it is important that the community adopt this approach. One related approach is using larger aircraft to perform the sampling. There are challenges associated with using a larger aircraft for this measurement approach including the following: (1) higher minimum flight height, (2) more restrictions on where the pilot can safely position the plane, (3)

faster speeds complicating the precision of the sampling. However, there are numerous advantages as well: (1) a more sophisticated instrument payload can quantify other processes, such as $\text{NH}_3/\text{NH}_4^+$ partitioning; tracers for contaminating sources, such as ethane can be measured; (2) detection of N_2O emission from soils can be estimated; (3) the greater range and flight time allows for longer measurement flights or sampling a larger number of CAFOs in a single experiment. Campaigns using large aircraft are more resource-intensive, so this approach would not be a good fit for routine ambient monitoring, but could be very useful for targeted studies of certain sources, or as a proof-of-concept to refine the techniques described in Chapter 2. Additionally, large-aircraft studies allow the study of the NH_3/CH_4 ratio on larger spatial scales than individual CAFOs.

In parallel to refined measurements of ammonia deposition near these sources, advances in modelling capabilities are essential in order to apply the approaches outlined in this dissertation to more realistic scenarios. In Chapter 1, with the exception of one sensitivity analysis, the results hold only for neutral conditions. Generalizing these techniques to other stability profiles would allow the simulation of a broader class of conditions. In principle, simulating all atmospheric stabilities is a logical next step; OpenFOAM can be run in a LES configuration, and there are examples in the literature of representing maize and other plant canopies in LES models. OpenFOAM is an open-source platform that is undergoing continued development, and it also features external modules that simplify the addition of new physics to the model. While LES simulations are more computationally expensive than K-epsilon, and the canopy representations are more complex in LES, simulating LES flow in and around different plant canopies is a very achievable goal with the current state of physical understanding, model development, and available computing resources. By investigating the ammonia recapture fraction under a wider range of stability conditions, we can more rigorously assess the effectiveness of different land surface types,

as well as shelter belt features, given the strong effect stability can have on boundary layer dispersion.

Beyond gaining a physical understanding of ammonia deposition and recapture, a more complete modelling tool could eventually be used to design CAFO layouts and test ammonia sequestration strategies that are tuned to individual CAFO sites. This type of modelling framework would require 3-D simulations with historical climate data for wind speed, wind direction, stability, temperature, and RH. All of these environmental variables are generally available from meteorological monitoring sites (e.g., CoAgMet for Colorado) or reanalysis. Furthermore, the seasonal behavior of plant canopies would need to be represented in both the CFD model as well as in the MODDAS, though this is in principle possible. However, for this application, the coupled CFD-dispersion-bidirectional flux models would need to be run in three spatial dimensions over a wide range of environmental conditions. With respect to the OpenFOAM simulations, it is feasible to extend to three spatial dimensions. The largest barrier would be computing resources available to run the model for this wide range of conditions. There are also some broader concerns about the performance of LES simulations in the nocturnal atmospheric boundary layer, given the stable conditions that usually arise. Extending MODDAS to three spatial dimensions would be more complex; while the Lagrangian Stochastic model could in theory be performed in three dimensions, it would require an order of magnitude more trajectories to generate the proper statistics for the dispersion. While this could be accomplished by parallelizing MODDAS to allow for distribution of trajectories across a larger number of processors, this parallelization would require some modification of the model, including file I/O; however, I argue that these modifications are likely a good next step for developing this model to perform well in a broader range of ammonia-deposition circumstances in a high-performance computing environment. The more challenging

step is the inversion of the dispersion matrix, which is a necessary step for the bidirectional flux calculation. In three spatial dimensions, the dispersion matrix will become extremely large. Even in the 2-D implementation of MODDAS, the dispersion matrix was on the order of 12gb for the largest domains, and in three dimensions, this may increase the size by 4 orders of magnitude. While there are computational techniques, including pre-built libraries for solving sparse matrix inversion problems in a parallel high-performance computing environment, or porting the code to a GPU environment, the sheer size of this matrix inversion problem could make these simulations impractical to perform in a research or design context. This has the potential to be a challenging numerical problem to overcome.

Another key finding from both Chapters 1 and 2 is that while concentrations may be elevated over long distance from the CAFO, the deposition flux quickly decreases to close to background value at distances longer than 5-10 km from the source. While this work has focused on constraining the local ammonia deposition, an important next step is using these results to more-narrowly constrain the impact of CAFOs at broader spatial scales, such as 20-50 km from the source, or even on regional air quality. The role ammonia plays in air pollution, and the lifetime of ammonia in the atmosphere, are both strongly impacted by the presence of atmospheric acids for the ammonia to neutralize, or the cloud water for ammonia to dissolve in, which are processes that are represented in chemical transport models, but I have neglected in this dissertation. However, there are additional processes, such as in-canopy or soil chemical processing of ammonia, that need to be pursued as areas of fundamental research in order to develop a fully processed-based understanding of ammonia's role in the nitrogen cycle. While CAFO methane emissions are already actively studied because of their role in climate change, understanding N₂O production from soils next to CAFOs may further link these types of agricultural practices to

climate change, and advance the conversation of whether these types of agricultural practices are indeed sustainable in the changing climate.

Finally, there are interesting comparisons to be made between the Colorado Front Range, and similar regions with highly industrialized agricultural systems, with developing countries like Botswana. Botswana does have a large cattle population in a hot and dry climate, but ammonia does not seem to be an important pollutant in the region where I made measurements. In the US, we have prioritized cleaning up emissions from coal power plants and combustion sources, which has led to decreases in ambient $PM_{2.5}$ concentrations; consequently, the United States is moving more towards fully-neutralized aerosol. Botswana has a large contribution of sulfuric acid to its regional aerosol; as it, and its neighboring countries experiencing rapid economic growth, combustion and sulfate emissions are likely to increase, which is well-correlated with fossil fuel combustions (Galeotti, 2003). However, as these economies manage emissions from these other sources, Botswana will likely experience similar changes to its source characteristics as we have observed in the US. One key unknown is the future of agriculture in Botswana; will developing countries adopt a industrial-agriculture approach similar to the CAFOs in the US, or will they develop more sustainable practices for beef production? This is a complicated interdisciplinary question linking economics and development, atmospheric science and chemistry, climate change, and human behavior, and is beyond the scope of this dissertation.

REFERENCES

- Galeotti, M., 2003. Economic Development and Environmental Protection (SSRN Scholarly Paper No. ID 465200). Social Science Research Network, Rochester, NY.
- Hacker, J.M., Chen, D., Bai, M., Ewenz, C., Junkermann, W., Lieff, W., McManus, B., Neining, B., Sun, J., Coates, T., Denmead, T., Flesch, T., McGinn, S., Hill, J., 2016. Using airborne technology to quantify and apportion emissions of CH₄ and NH₃ from feedlots. *Anim. Prod. Sci.* 56, 190–203. <https://doi.org/10.1071/AN15513>
- McGinn, S.M., Janzen, H.H., Coates, T.W., Beauchemin, K.A., Flesch, T.K., 2016. Ammonia Emission from a Beef Cattle Feedlot and Its Local Dry Deposition and Re-Emission. *Journal of Environmental Quality* 45, 1178–1185. <https://doi.org/10.2134/jeq2016.01.0009>
- Miller, D.J., Sun, K., Tao, L., Pan, D., Zondlo, M.A., Nowak, J.B., Liu, Z., Diskin, G., Sachse, G., Beyersdorf, A., Ferrare, R., Scarino, A.J., 2015. Ammonia and methane dairy emission plumes in the San Joaquin Valley of California from individual feedlot to regional scales. *Journal of Geophysical Research: Atmospheres* 120, 9718–9738. <https://doi.org/10.1002/2015JD023241>
- Shen, J., Chen, D., Bai, M., Sun, J., Coates, T., Lam, S.K., Li, Y., 2016. Ammonia deposition in the neighbourhood of an intensive cattle feedlot in Victoria, Australia. *Scientific Reports* 6, srep32793. <https://doi.org/10.1038/srep32793>
- Shen, J., Chen, D., Bai, M., Sun, J., Lam, S.K., Mosier, A., Liu, X., Li, Y., 2018. Spatial variations in soil and plant nitrogen levels caused by ammonia deposition near a cattle feedlot. *Atmospheric Environment* 176, 120–127. <https://doi.org/10.1016/j.atmosenv.2017.12.022>

Staebler, R.M., McGinn, S.M., Crenna, B.P., Flesch, T.K., Hayden, K.L., Li, S.-M., 2009. Three-dimensional characterization of the ammonia plume from a beef cattle feedlot. *Atmospheric Environment* 43, 6091–6099. <https://doi.org/10.1016/j.atmosenv.2009.08.045>

APPENDIX A. OTHER OPENFOAM-MODDAS MODEL INPUTS

This section contains some additional values used as inputs to run MODDAS, as well as to test the sensitivity to parameters. Figure A.1 shows the leaf area density profiles used to model the drag as well as to determine the resistances in the bidirectional flux model. The CAFO LAD profile was only used only to represent turbulence in the OpenFOAM simulations, and does not undergo bidirectional flux in MODDAS.

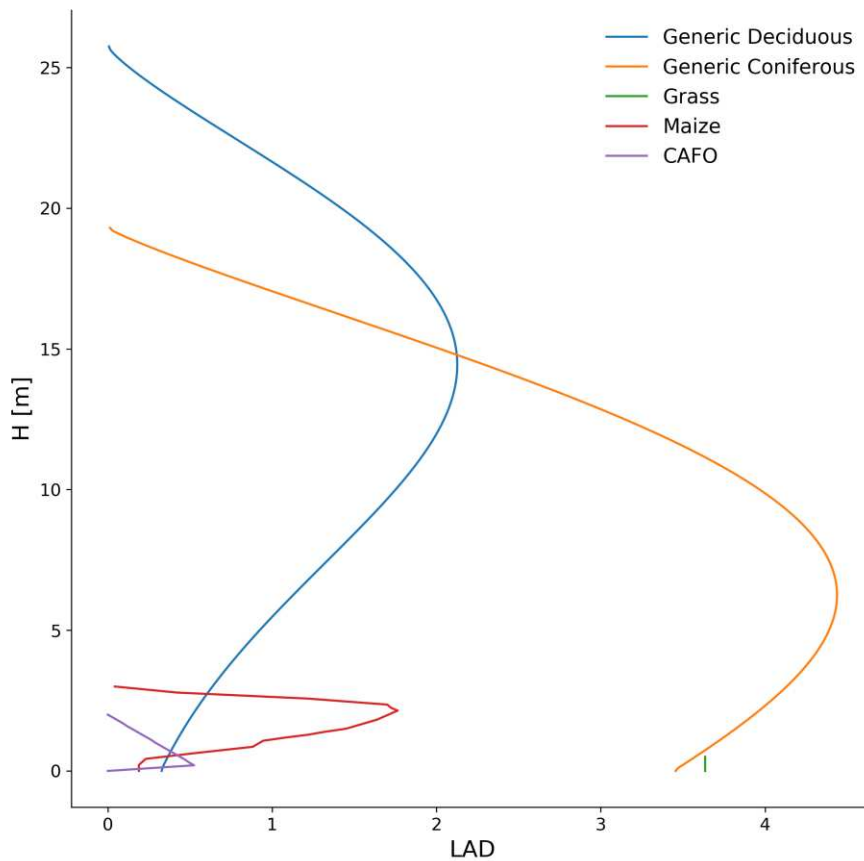


Figure A.1: Leaf area density profiles for the different plant canopies (plus the representation of the CAFO surface)

In Table A.1, I list the different values used for ammonia emission potential in the maize canopy for the sensitivity simulations, along with the ammonia recapture percentage for the base-case and hot-dry simulation scenarios. Γ_s has little-to-no effect on the recapture fraction in cold humid conditions, but can have a big effect under hot dry conditions. The complete results can be found in Chapter 2.3.3 and the analysis and discussion can be found in Chapter 2.4.2.

Table A.1: Different values for Γ_s used in the sensitivity simulations, and the associated ammonia recapture fractions for base-case conditions (T = 8 degrees C, RH = 75%) and for the hot-dry case (T = 26 degrees C, RH = 30%).

Γ_s	Value	Recapture (base case)	Recapture (hot and dry)
Γ_1	1186	33.9%	30.8%
Γ_2	4744	33.8%	28.0%
Γ_3	9488	33.3%	24.2%
Γ_4	14232	33.3%	20.5%
Γ_5	18976	32.6%	16.9%
Γ_6	23720	32.2%	12.8%
Γ_7	28464	31.9%	9.1%
Γ_8	33208	31.4%	5.6%

APPENDIX B. SUPPLEMENTAL MATERIAL FROM CHAPTER 3

This appendix contains supplemental material from Chapter 3, which is currently undergoing peer review. Appendix B.1 contains a comparison between SAM simulations and some surface observations of meteorological data and ammonia measurements next to a CAFO.

B.1 Comparison of SAM Simulations to Observations

Below, we present our comparison between SAM simulations and surface observations.

Figure B.1 compares a few meteorological variables to observations taken from the CoAgMet

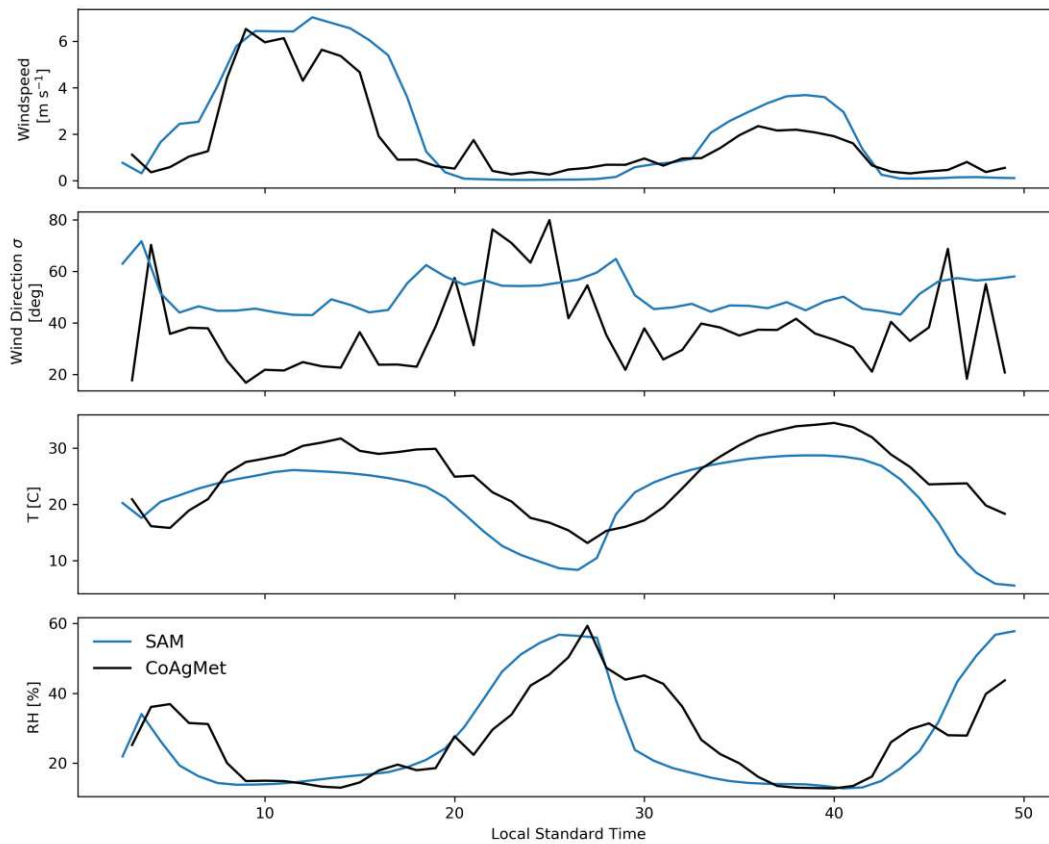


Figure B.1: Comparison of SAM meteorological variables (blue) with CoAgMet measurements for the dates simulated. CoAgMet site FTC01 met variables are compared to SAM domain average variables over 28 hour simulation from top to bottom: windspeed, wind direction standard deviation, T, and RH.

network, site FTC01, which is located near our simulation location on the same days. The CoAgMet data is plotted at hourly intervals, and the SAM output is averaged over the model domain and plotted at hourly intervals. The model reproduces the wind speed, T, and RH during the time period reasonably well; the wind speed follows more of a diurnal cycle, but the magnitude and general trends of wind speed throughout the day. When running SAM, the model domain is rotated so that the mean wind always blows in the positive x direction, so there are no mean changes in wind direction, which may complicated the wind direction comparison. However, we think that this comparison reflects well on SAM to produce realistic turbulent conditions.

In Figure B.2, we compare the fenceline ammonia concentrations to an observational dataset. The data shown here are from the field study Shonkwiler et al., (2017), which measured fenceline ammonia concentrations from a medium-sized CAFO in northern CO. While we use the emission fluxes that are reported in that study, and the CAFO is approximately the same size, there are a number of factors that differ between the real ammonia concentrations and our simulations: (1) the measurements were taken in a different location with different meteorology, surface roughness, sensible/latent heat flux, and boundary condition wind profiles; (2) the real-life CAFO likely is not perfectly square-shaped; (3) the CAFO buildings and fences and cattle are not present in the SAM simulation and wake effects could redirect the flow; (4) the emissions at the real CAFO are dynamic functions of environmental conditions such as wind and T. Based on these differences, we do not expect SAM to exactly reproduce the measurements. Rather, we have selected 4 days (of approximately 4 months of measurements) where the measured concentrations appear to be well-represented by the simulations. On many days not plotted here, the measurements showed very low NH₃ concentrations, due to the monitoring site being positioned upwind of the CAFO. Furthermore, the ammonia obs are only available at 15 minute temporal resolution. However, on

days with winds blowing in directions represented by our simulations, and given similar emissions fluxes and source sizes, the concentrations qualitatively appear to be reasonable, given the

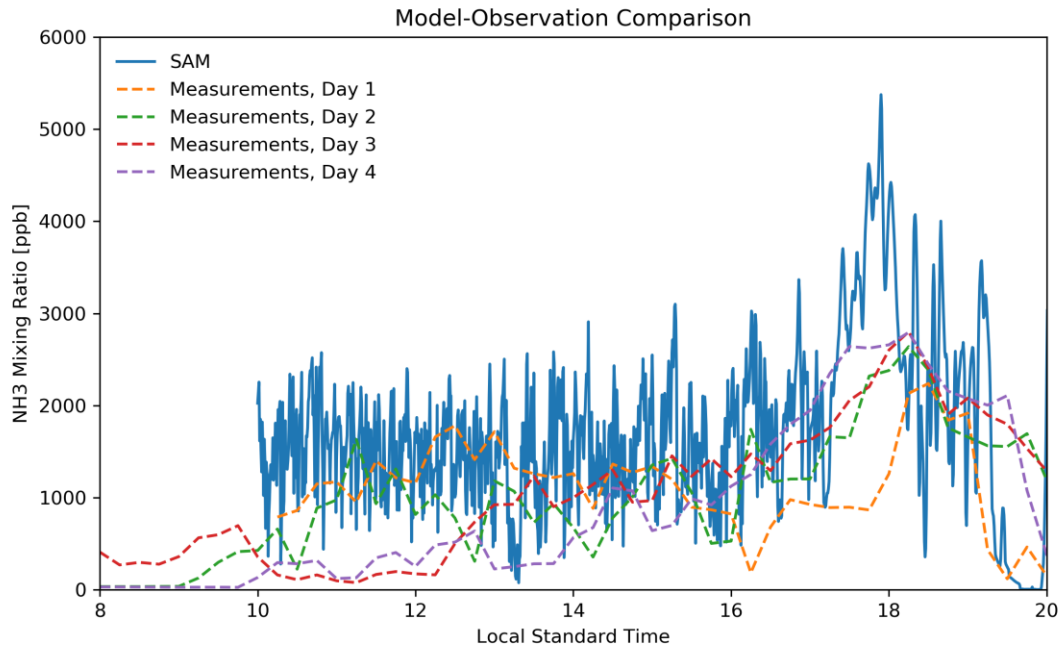


Figure B.2: Comparison of SAM NH₃ concentrations with Picarro measurements from a CAFO fenceline in northern Colorado.

numerous simplification/approximations required to run an LES model such as SAM.

Both for the comparison of meteorological variables and for the ammonia comparison, we had to rely on measurements and data that are published and available or that we could obtain through collaborators, as we did not have the budget or time to conduct a measurement experiment. Both comparisons indicate that based on the available information, SAM simulations are producing turbulence that is realistic, and the idealized CAFO representation is producing atmospheric loading that reflects real life behavior.

B.2 SAM Simulations from April

In this section, we share figures analogous to Figure 2-4 in the main manuscript, but for simulations performed during the springtime (April 1-3, 2013). These figures are included to demonstrate that the methodology can work in other times of year with different environmental conditions. The days we selected were sunny with no precipitation, or frontal passage occurring.

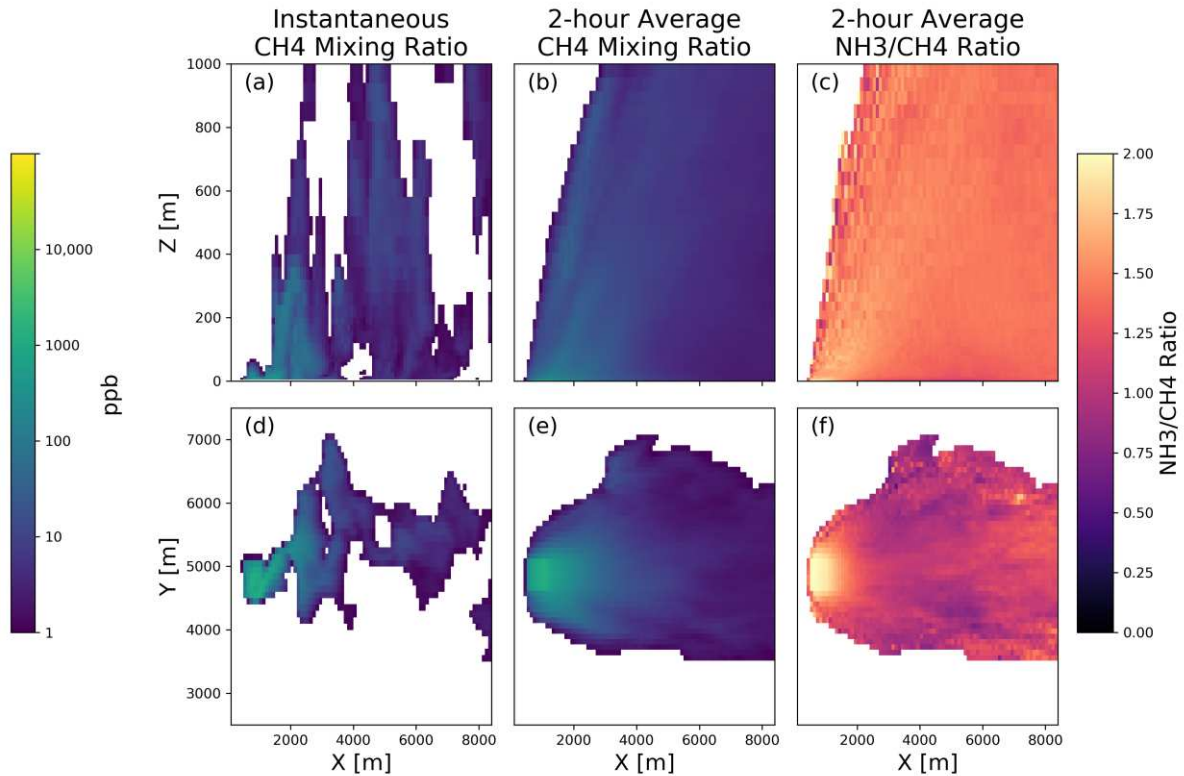


Figure B.3: The instantaneous and steady-state plume behavior from SAM simulation output. Analogous to main-text Figure 3.2, the instantaneous and steady-state plume behavior from SAM simulation output for April simulations. The top row shows domain centerline concentrations (x vs z) with (a) showing excess methane concentration model output from a single timestep, (b) showing a 2-hour average from 10-12, and (c) shows the ammonia/methane excess concentration ratios. The bottom row (d, e, and f, respectively) shows the same

The discussion of these figures is analogous to that for the June simulations, which is contained in Chapter 3, sections .3.1-3.3.2. The main difference with April atmospheric conditions is that there appears to be more vertical mixing, and slightly less deposition (18%) as compared to June (20%).

The bias associated with considering only surface ratio is less severe than the June atmospheric

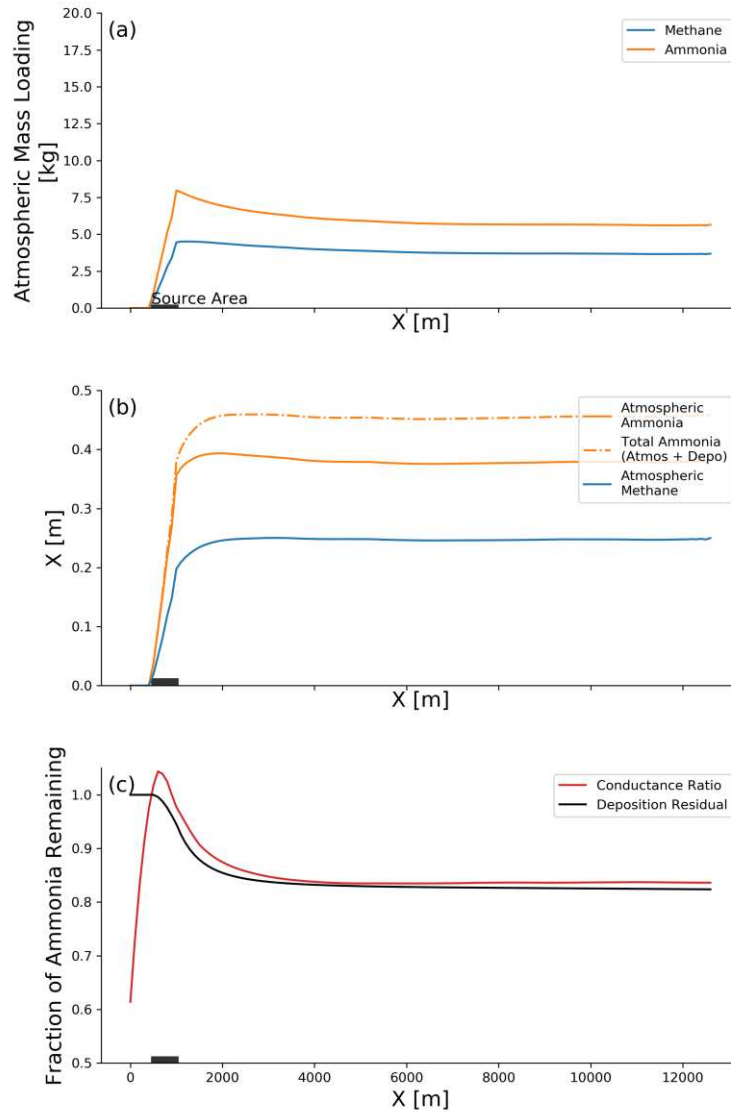


Figure B.4: Analogous to Figure 3.3 but for April; (a) the total Y-Z integrated ammonia and methane mass loading plotted as a function of x , (b) the atmospheric Y-Z mass conductance for ammonia and methane (solid lines), as well as integrated reference deposition flux (orange dashed line) and the deposition-corrected ammonia mass conductance (orange dot-dashed), and (c) the fraction of ammonia remaining calculated from the deposited mass (black) and from the ammonia/methane conductance ratios (red).

conditions, though the difference is most pronounced outside of 4 km from CAFO boundary ($x > 5000$).

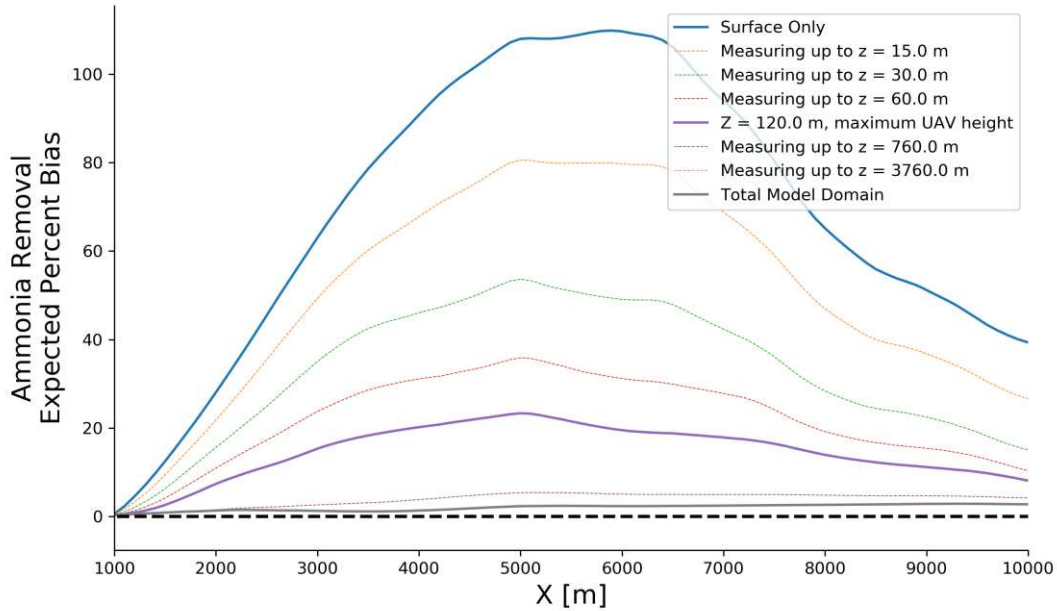


Figure B.5: Analogous to Figure 3.4, but for April; percent bias of the fractional ammonia removal, comparing the centerline mass loading ratio (the novel method) and the offline actual deposited mass method (our reference method) plotted vs. the x coordinate in the model simulations, where $X = 1000\text{m}$ corresponds to the CAFO boundary. Each line corresponds to the inclusion of a different vertical depth in the model domain in the centreline ratio method with the solid blue line using only the surface concentrations, the purple line using 120m and below (i.e., the maximum allowed altitude for a small Unmanned Aerial System without FAA certification), and the gray line represents the entire model domain. Intermediate altitudes are represented as dashed lines. A bias of 0 denotes perfect agreement between the methods.

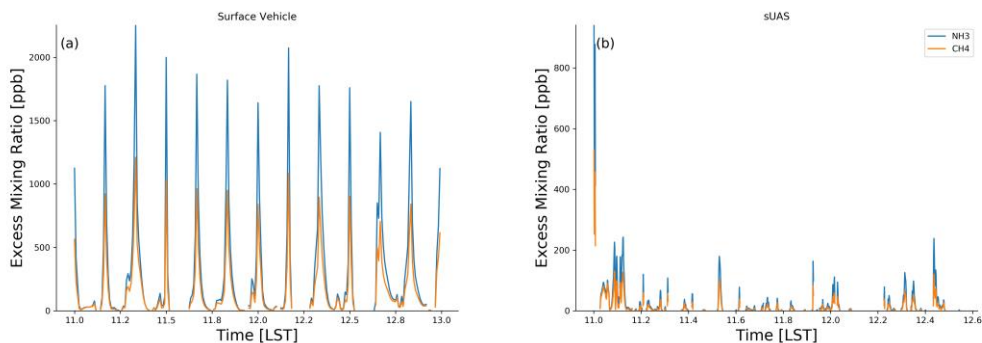


Figure B.6: Analogous to Figure 3.5, but for April; observed ammonia and methane concentration timeseries in Local Standard Time (LST) (blue and orange, respectively) from the surface-vehicle-based platform (a) and the sUAS platform (b).

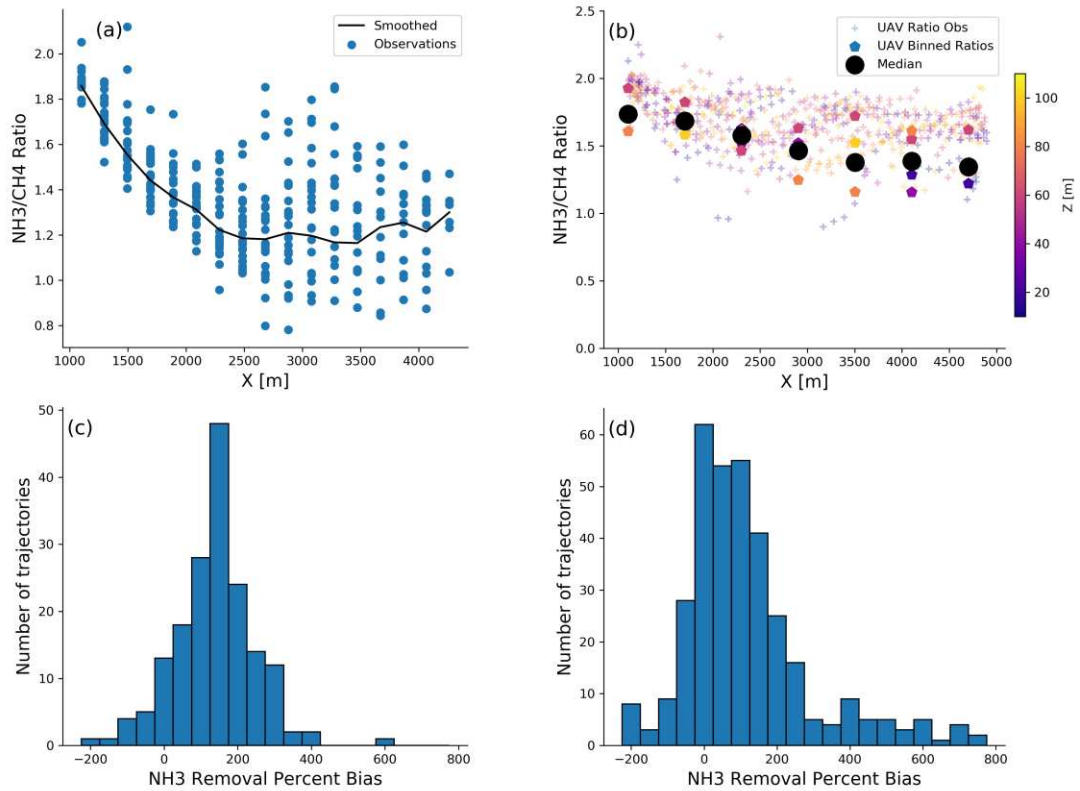


Figure B.7: Analogous to Figure 3.6 but for April; (a) Observed ammonia/methane ratios for the surface-vehicle-based and (b) sUAS-based observations with binned-by-X values overlaid. The surface vehicle base-case trajectory used a 2-hour sampling period, the sUAS trajectory used a 45 minute sampling period. The bottom two panels present histograms of the percent bias for the fraction of ammonia removed that can be inverted from a given sampling trajectory, compared to the actual deposited fraction computed with the direct offline calculation over the corresponding spatial interval. Panel (c) shows the vehicle results and (d) shows the sUAS results.

B.3 Sensitivity Analysis across a broader range of spatial perturbations

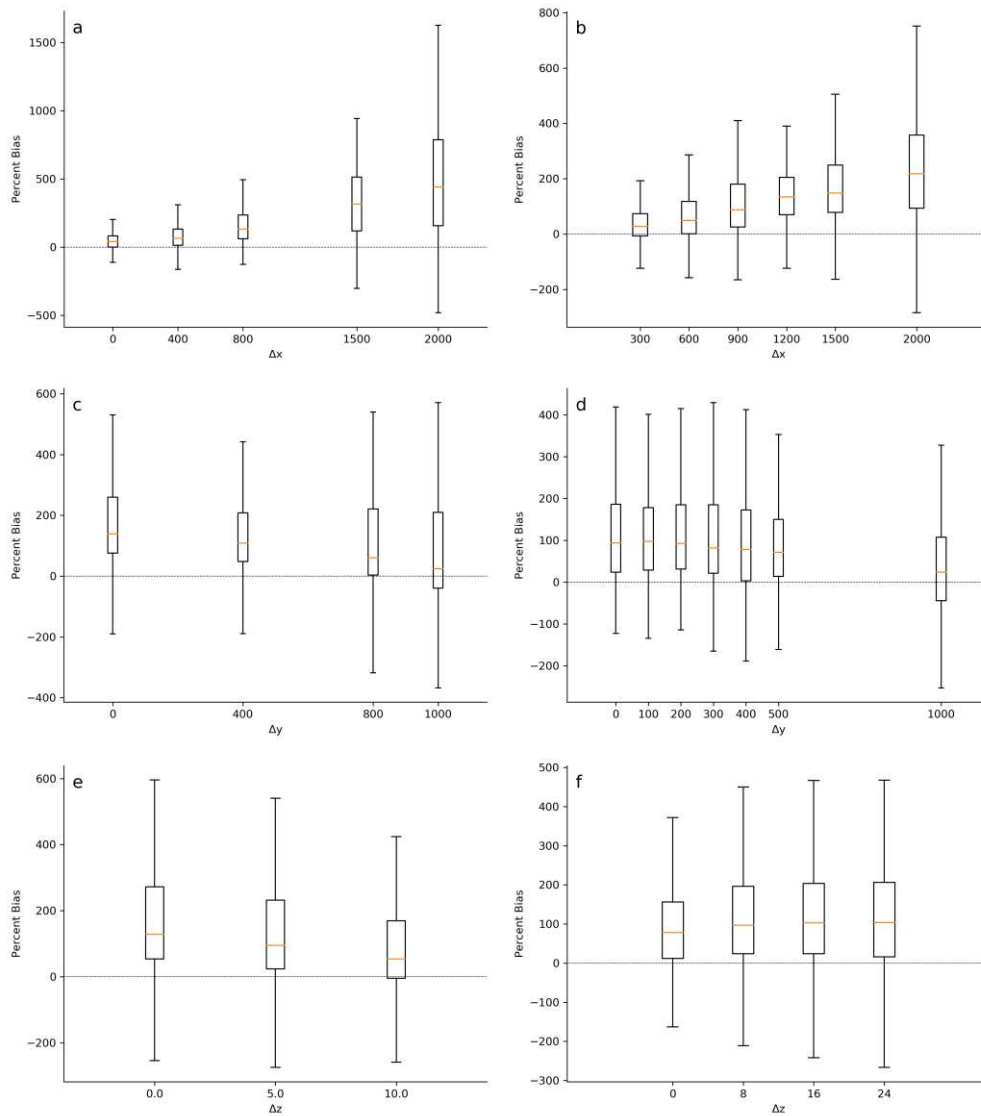


Figure B.8: The complete sensitivity analysis described in Chapter 3.3.3, showing the sensitivity of the surface vehicle and sUAS sampling trajectories to all perturbation types. None of the other variables show any interesting behaviour beyond what is described in the main text of the manuscript.